NAVIGATING THE ENERGY LANDCAPE OF MARTENSITIC TRANSFORMATIONS

A Dissertation

by

RUBEN VILLARREAL

Submitted to the Office of Graduate and Professional Studies of
Texas A&M University
in partial fulfillment of the requirements for the degree of

DOCTOR OF PHILOSOPHY

Chair of Committee,	Raymundo Arroyave
Committee Members,	Banerjee Sarbajit
	Tahir Cagin
	Ted Hartwig
Head of Department,	Andreas A. Polycarpou

May 2020

Major Subject: Mechanical Engineering

ABSTRACT

The following work presented focuses on the characterization and navigation of energy landscapes in systems that undergo solid state phase transformations; including the broad category of shape memory alloys, with extended study of the model systems copper zirconium (CuZr-X), doped vanadium dioxide (VO2B) and carbon nitride (C4N3). The third section on CuZr-X and HTSMA Database will present computational results used to guide selection of alloying elements (Ni ,Co, Hf) for manipulating the transition temperature (Tc) and lattice compatibility of CuZr-X, a high temperature shape memory alloy (HTSMA). In the same section, a broader outlook on the systematic discovery of HTSMAs is given through the generation of a binary alloy database with practical formulation to predict the effects of alloying elements on hysteresis. A similarity metric based on the fretchet distance between minimum energy pathways is introduced as a tool for catergorizing and eliminating subsets of related systems. Section 4 details an algorithm for systematic doping of group-subgroup related phases developed to resolve the energy landscape of boron metastable conditions in VO2 induced by a phase transformation. Section 5 will introduce the development of a general metric based solely on structural features and its practical application in the study of dynamical stability in carbon-nitride systems.

DEDICATION

To my wife, mother, father, and family

I am forever grateful to have experienced the great love and support that only God can bring. Thank you for all unforgettable moments that I will cherish with me till the end and the sacrifices on my behalf that allowed me to stand proud.

To my sister,

No words can describe how you have enriched my life and continue to do so. Thank you for being you, the strong root of the family.

To the dearly departed,

I look forward to rejoicing once again together in eternal peace

CONTRIBUTORS AND FUNDING SOURCES

Contributors

This work was supported by Professor Raymundo Arroyave of the Department of Materials Science at Texas A&M University.

The structural characterization for Chapter 4 were contributed by coauthor Prashant Singh who performed vibrational, electronic, elastic, and optical property characterizations of newly proposed structures.

All experimental results presented in Chapter 3 were provided by Yucong Miao and Professor Joost J. Vlassak at the VLassak group of Harvard University.

Experimental results presented in Chapter 4 were provided by Dr. Diane Sellers and Professor Sarbajit Banerjee of the Chemistry Department at Texas A&M University.

The correspondence relationships in Chapter 4 were provided by Dr. Timothy Brown of the Materials Science Department at Texas A&M University.

All other work conducted for the dissertation was completed by the student independently.

Funding Sources

This work was supported by the Air Force Office of Sponsored Research under Grant No. FA9550-16-1-0180. I acknowledge further support from National Science Foundation through grants no. (DMREF) CMMI-1729350. First-principles calculations were carried out at the Supercomputing Facility at Texas AM University.

TABLE OF CONTENTS

Page

LIST OF FIGURES

FIGURE Page

LIST OF TABLES

TABLE Page

1. INTRODUCTION

The study of phase transitions in solid state materials has fascinated and preoccupied the time of many inquisitive minds. Materials seem to choose either one form or another depending on external conditions such as temperature, stress, and pressure. A phase transition is a macroscopic expression of a material navigating the energy landscape to find its global energy minimum. Along the way, it can get trapped in metastable states whose properties are sometimes more useful than the ground state. From a classical thermodynamic viewpoint materials phase transform when a a lower energy state becomes accesible to it. If the system is under constant pressure and volume, the relative stability of the phases will dictate the equilibrium phase which minimizes the gibbs energy of the system and thus the phase selection is controlled by a minimization process.

In particular, the allotropic forms expressed by a structural phase transition often exhibit abrupt changes in material property. One of the most organized type of solid state transitions occurs in the shape memory alloys (SMA). The first SMA was discovered by Arne Olande in 1938 in an alloy of gold and cadmium. Shape memory alloys are phase transforming materials with properties that seem to defy the traditional notion of deformation and strain. Displaying strain deformation recovery many times larger than the elastic limit of other metals. The recovery mechanism follows the martensitic path back to its original form but not by retracing its macroscopic steps in reverse, but instead by never having deformed in the first place. The deformation only "uncoiled" its hidden transformation strain. This sleight of hand can be explained by the symmetry relationship between the parent phase, refered to as austenite and the daughter phase, called martensite. At higher temperatures, the high symmetry phase is stabilized. As austenite is cooled it transforms into one of several energetic equivalent variant forms of martensite. This process results in a loss of symmetry of the crystal lattice that can only be reversed back to the single variant parent form. When the austenite form and SMA transforms to martensite, the strain caused by lattice deformation if canceled out on average by reorientation of the variants in opposing strain directions. This is made possible by the energetic equivalence of each variant. The result of this is that the martensite does

not cause macroscopic deformation of the material. This process of martensite variant arrangement if known as self-accomodation and allows for SMAs to hold potential of large strain deformation without plastically deforming the martensite.

The microstructural features of martensite were not well understood until the development of the phenomenological theory of martensite crystallography (PTMC). The theory developed out of a natural progression of the bain strain which considered an orientation relationship between austenite and martensite. Due to the contraint of the surrounding austenite matrix the martensite crystal cannot grow uninhibited within the matrix as that would cause accumulation of stress. Instead, the martensite lattice strain is accomodated by the creation of variant twin groups. The twin variants interface along coherent planes of symmetry that opposes their relative strains to the parent lattice and eliminates macroscopic strains.

Shape memory alloy compositions can span the range of intermetallic elements and display many common features found in martensitic systems; Such as martensite twin formation, discontinuous change in lattice parameters (first-order), hysteresis, and non-diffusive displacement of the atoms. They derive special value however owing to their non-linear elastic properties; Granting them macroscopic shape recovery, high reversibility, large pseudoplastic strains, and motor less actuation. The scope of SMA applications has been limited predominantly by the degradation of functionality during cycling especially higher transformation temperatures (> 390K). HTSMAs can be prone to strain hardening due to generation of slip dislocations, brittle behavior, incomplete shape memory and plastic deformation during processing due to a lowering of yield stress. Recent foundational development on the geometric theory of martensite has established methods for quantitative analysis of twin morphology based on compatibility conditions within the parent matrix. The conditions of lattice compatibility are known as the cofactor conditions. Particular interest is given to the condition associated with the middle eigen value lambda of the stretch matrix U equaling one which has been associated to sharp drops in hysteresis [6]. Although ideally defect generation due to macroscopic stress build up is mitigated as the lamda=1 compatibility condition is reached [7], there is to date no general guideline for predicting alloying effects on the

transformation temperature, hysteresis or lattice compatibility.

The following work is presents the amalgamation of research into the symmetry of structures and there phase transformation energetics. Challenges taken on in the VO2 system are iterated further in the development of an HTSMA database of binary alloys. Section 3 dwelves deep into the symmetry analysis of VO2B system to discover new and exiting behaviour of boron interstitial as it navigates the energy landscape of a phase transition. The following section is dedicated to methods for the accelerated discovery of HTSMAs and establishes new ground for practical predictions of system compatibility, symilarity and hystersis. By estimating the cofactor condition, λ_2. It becomes possible to compare the effect of ternary alloying elements on lattice compatibility. By first analyzing the energy landcape of model system CuZr-X, the work follows a logical expansion of analysis on a much larger scale and produces usable output with easily interpretative results. A measure of similarity between systems is introduced based on the fretchet distance between to curves. The measure allows for quickly catergorizing system under a quantitative value representing the curves of minimum energy pathways (MEP). The final section introduces a metric with good prediction for dynamic stability of carbon nitride systems. The metric is purely based on structural information and can be readily extended to other systems with similar covalent bonding schemes.

1.1 Quotes

'Certainly, the specific morphology and configuration of a variant group depends on the nature of the self-accommodation to minimize the transformation strain energy accompanying the nucleation and growth of the martensite.' [8]

1.2 Motivation

1.2.1 Metastability

Materials that undergo martensitic transformations (MT) are of great technological importance with wide applications in aerospace, biomedical, and electronics industries. Some notable materials exhibiting martensitic phenomena include the shape memory alloy (SMA) such as Nitinol and

some correlated electronic materials coming from the early transition metal oxides. Such transformations can be engineered to serve in a vast array of application requiring functional switching of material properties with applications for motorless actuators, advanced optoelectronics, neuromorphic devices, and shape healing. The energy lanscape of a martensitic transformation has at least two associated minimas representing the relative stabilities between parent and product phases. The minimas are connected through a minimum energy pathway (MEP).

Energy landscapes of solid phase transitions map the real space structure elements to all its associated potential energies. With the peaks representing the energetic barriers of transition states and the local minima connecting them through minimum energy pathways (MEPs). Phase stabilities are sensitive to changes in state variables such as temperature, pressure, and stresses which in turn alter the energy landscape. For example, there have been computational studies on ZrO2 focused on resolving the transition kinetics based on the potential energy surface (PES) in phase space [9]. The Zirconium oxide ceramic has one of the highest martensitic transformation temperatures (1000^{o} C) and a large thermal expansion (4.2% volume increase). The high transition temperature makes it a difficult system to study experimentally but its wide application in crack resistant parts as well as its dielectric properties have kept active research in its transformation energetics. The authors found a possible pathway through a low temperature orthorhombic phase (o-phase) that featured a high energy barrier transition back to monoclinic. This o-phase has a similar volume to the high temperature tetragonal phase but exists kinetically at low temperature via a high energy barrier and therefore prevents transformation toughening normally attained from the larger volume change. Other theoretical studies on ZrO2, and HfO2 have just focused on characterizing transition enthalpies with comparison to experiment in order to validate the implemented theoretical model of the transition [10].

One important design parameter in first-order phase transformations is the thermal hysteresis width. It is believed that the part of the hysteric effect is created by frictional forces of the interface junctions between austenite and martensite [11]. Hysteresis can be considered as a energetic cost in accessing phase properties at either end of the transformation. The larger the hysteric loop

area, the larger the amount of energy dissipated. A small hysteresis width is needed in devices that implement properties of both the austenite and martersite in quick reponse to an external stimulus. While a broader width can serve as a stabilizing feature in low power memory and computation circuits. Furthermore, it is found that introducing dopants into the lattice can modify the hysteresis of the transition and have pronounced effect on transition temperatures. Hysteresis in transition metal oxides (TMOs) has been shown to be highly sensitive to doping [12; 13]. Current results of our investigation in a VO2 model system will show that introducing a Boron atom interstitially leads to a crossed energetic ordering of metastable sites across the phase transition. This unexpected mechanism could lead to an improved understanding of hysteresis width of VO2 in memristic applications. It is possible that this metastable trapping effect is not exclusive to VO2 and gives motivation to explore the site metastability in other TMOs.

1.2.2 Highthroughput HTSMA Database

Density functional theory (DFT) is expediently becoming an integral part of collaborative research where experimental efforts are either too expensive, need qualitative confirmation, or are near impossible to undertake. Recent advances in computational power and cost has made high throughput screening of material properties a tangible strategy for creating autonomous materials discovery frameworks (AMDF) but due to the practically infinite material search space, the implementation of screening algorithms requires tailoring the sampling methodology so that it navigates the search space in an informed manner.

Current efforts to reduce the exploratory expense of these calculations builds on a framework to reduce computational cost via smart regression sampling of the energy landscapes in martensitic transformations. Operating under the assumption that energetics at the ground state are sufficiently smooth and well suited for gaussian regression reduced order modeling;

Density functional theory (DFT) is expediently becoming an integral part of collaborative research where experimental efforts are either too expensive, need qualitative confirmation, or are near impossible to undertake. Recent advances in computational power and cost has made high throughput screening of material properties a tangible strategy for creating autonomous materials

discovery frameworks (AMDF) but due to the practically infinite material search space, the implementation of screening algorithms requires tailoring the sampling methodology so that it navigates the search space in an informed manner.

In data science based on materials research the bottleneck for generating useful databases does not always come down to computational cost but also to applying domain knowledge so that the type data generated best answers the questions relevant to the problem at hand. Currently there are a few comprehensive databases generated by ab-initio calculations such as the Open Quantum Materials Database (OQMD) or the Materials Project (MP), but they focus primarily on property characterization. The database allows searching in compositional space and rank orders structural polymorphs by their total energy. These type of databases can serve as useful static points of entry along an arbritrary energy landscape.

Many of the structures found in such databases are related through a phase transformation yet the database does not contain information regarding the energetics of transformation pathways. The lack of this type of information is not due to unawareness of the its importance and more to do with the lack of clear methodology for generating such a database efficiently.

Current efforts to reduce the exploratory expense of these calculations builds on a framework to reduce computational cost via smart regression sampling and energy landscape exploration with iterative doping schemes. For this I have looked at employing regression techniques and on-the-fly sampling of the search space to converge minimum energy paths of a phase transition. Energetics at the ground state are sufficiently smooth and well suited for Gaussian regression reduced order modeling. This methodology is currently applied to search for HTSMA B2 to Cm transition in shape memory alloys and lends itself to further development as a framework tool in practical collaborative research.

1.2.3 Boron Migration in VO2

In displacive transformations that subduce a symmetry break such that the product is a subgroup of the parent structure, the possible deformations are constrained to pathways of maximal symmetry groups. In other words, the deformation cannot generate a symmetry that is not found in

the parent phase. This is not the case for reconstructive transformations which are also considered displacive but require only that the lowest symmetry deformation be a subgroup of both parent and product phases. The energetics of the transformation dictate the the bounds of the deformation in real-space while the symmetry contraints express the dimensionality of the representation. For example, at high temperatures the ferroelectric barium titanate is a centrosymmetric. As the temperature is lowered, the parent structure undergoes multiple phase transitions that are evidenced by spontaneous electric polarization along different orientations relative to the initial crystal lattice. The initial polarization occurs when Ti cation shifts in position away from the center of inversion. Similarly, further transitions are caused by sequential shifts of Ti along different direction.

A detailed symmetric and energetic analysis of the interstitial sites on boron doped VO2 has been performed with an emphasis to resolve the complex energetic transition pathways. The results give a plausible atomistic explanation for a memory effect found in the transition. To my knowledge a mechanism of this kind has never been evidenced through both calculation and experiment. Since the memory effect in VO2 has been sought after as a design material for low-power nano sized memory devices, there is great interest in resolving possible mechanisms to fine tune the hysteresis response and kinetics of metastability in this compound.

As a starting point, we consider that a proper martensitic transformation keeps neighboring atoms the same across the transition and therefore once a one-to-one atomic correspondence between both crystal structures is established, we can ask questions about the energetic consequences that breaking symmetry has on the energy pathways of a dopant site across the forward or reverse transition. For a corresponding interstitial site to remain stable, it must be at the minimum energy in both phases. The overlapping unit cells in Figure 1.1 shows how the most stable boron site in rutile corresponds to a metastable site in monoclinic. **Figure 1.2** further down shows a schematic of energy levels for Boron stability at 0K. The first distinct feature of the graph can be seen in the middle portion at the M1 phase. Symmetry analysis reveals that the most stable R-site has correspondence to two inequivalent sets of positions in the M1 phase, as can be seen by the circled double lines. These inequivalent positions are metastable and degenerate. The next major feature

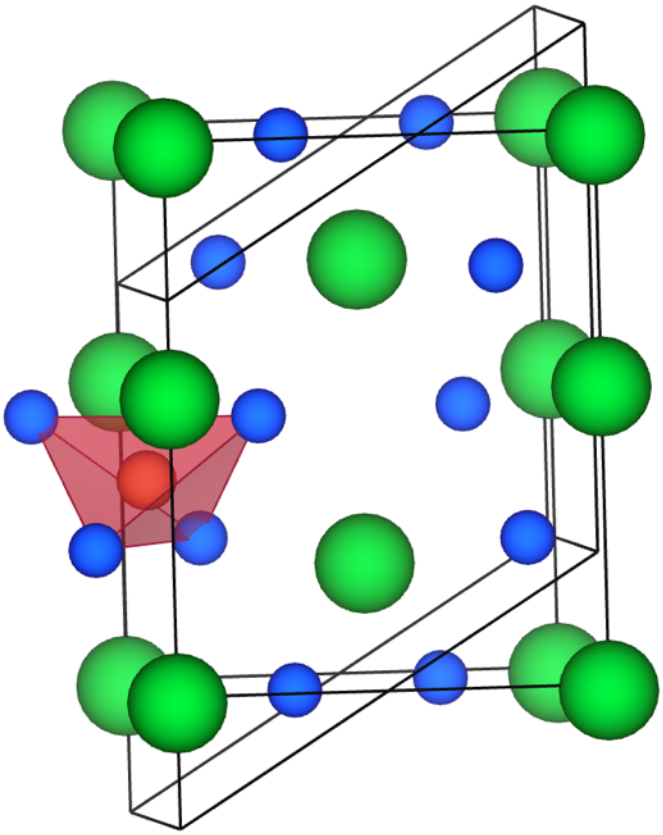

Figure 1.1: Interstitial site correspondence

in the figure can be seen on the right R phase portion. Here there is no degeneracy because R has higher symmetry.

The most relevant relaxation pathways are those which involve the most stable sites and their corresponding sites at the other phase. To start, direct pathways are calculated between start and end positions to estimate barrier energies. **Figure 1.3** below shows the energy barrier of Boron relaxation calculated using the SSNEB (Solid State Nudged Elastic Band) method. The activation barrier is 1.23 eV and driving force is 0.153 eV. Here only one of the degenerate sites was used in the SSNEB calculation. At least two more pathway calculations need to be run for the sake of thorough energetic analysis. One involving the second degenerate site. The other, is the intermediate metastable site found slightly above the lowest energy level.

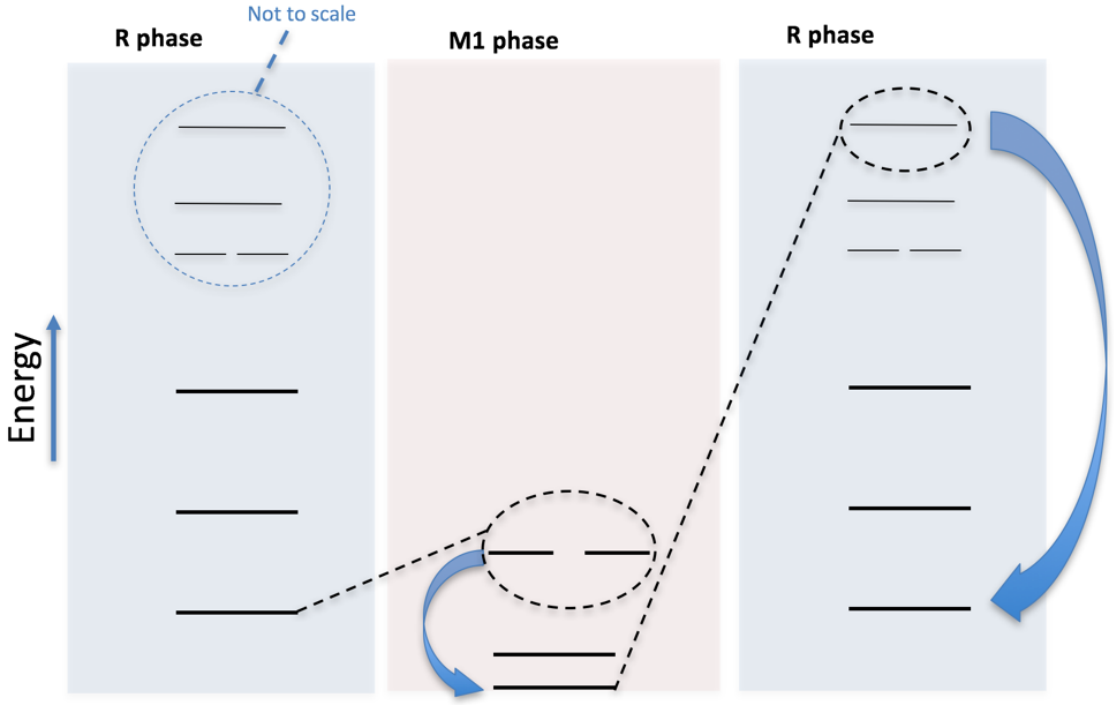

Figure 1.2: GGA calculated interstitial energies

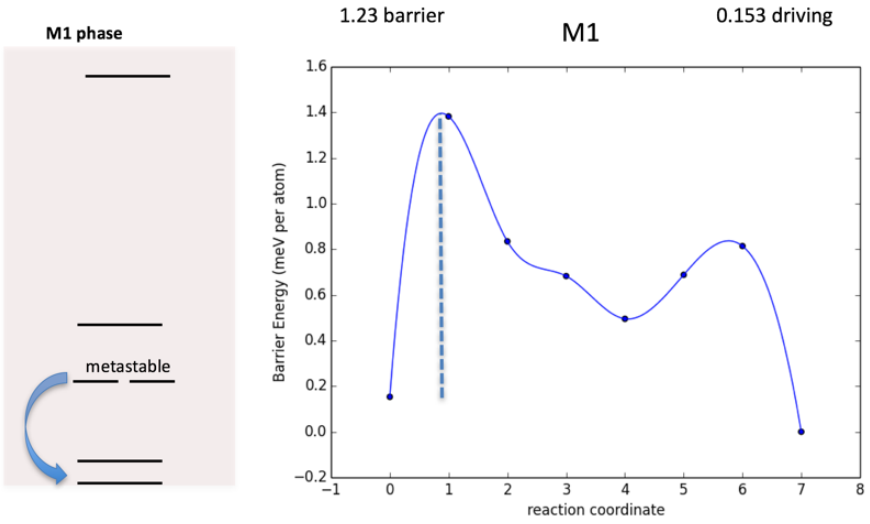

Figure 1.3: M1 barrier to relaxation

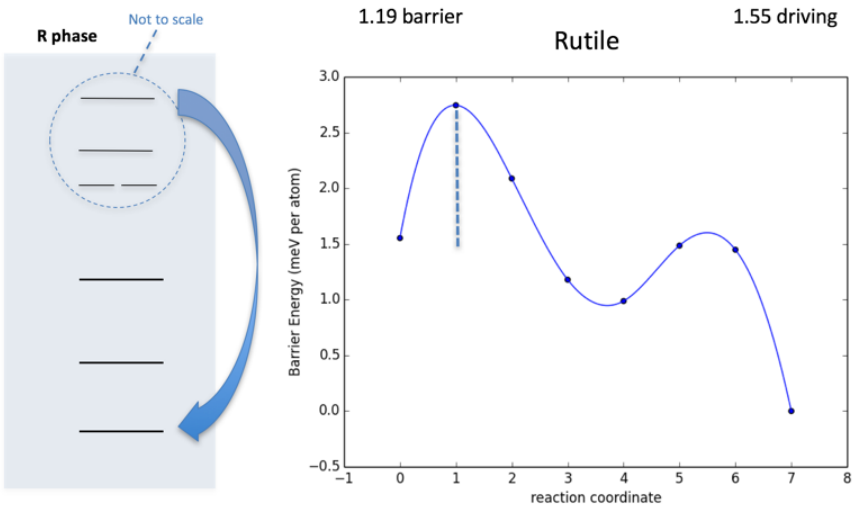

Figure 1.4: Rutile barrier to relaxation

Next, in **figure 1.4** , the calculated barrier for Boron relaxation in R phase is 1.19 eV, but this time, a considerably larger driving force of 1.55 eV helps the relaxation along. Here, things get considerably more complicated since there are several intermediates possible at lower energy than the established corresponding site.

Figure 1.5 below shows the first step in the iteration. The results show at least initially that this step is preferential but the possibility of higher energy barriers at each step remains. Still, it shows that it is necessary to try several more iterations to get a better understanding of the relaxation.

In summary, the phase transformation evolves to a metastable configuration and an energy barrier must be overcome to reach the equilibrium site position. The size of the energy barrier can have significant effect on the transformation dynamics and will depend on the metastable conditions that are possible. By analyzing site energies, I have established which pathways are most relevant to the transition and what are the necessary calculations needed for thorough analysis.

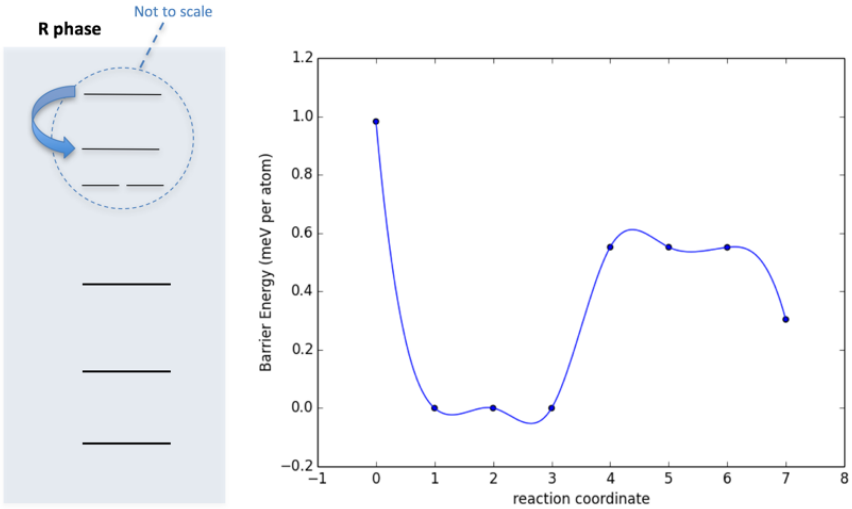

Figure 1.5: Rutile metastable relaxation

2. METHODS

2.1 Highthroughput Sampling Framework

To develop a sampling framework, a gaussian process regression method was employed on the pure HfO2 system and on Silicon doped HfSiO2. Validation of convergence is based on comparing the gaussian regression generated MEP and the true high resolution MEP. The pathways between high resolution (9x9 grid) PES and gaussian PES converge between 30-40 sampling points as can be seen in figure 6. This is a 50% reduction in the computational cost. If the grid was a higher resolution, the computational savings would be greater since further resolution increase would not change the MEP and convergence would still be reached at the same number of sampling points.

To test further possible improvement in cost reduction, the Si doped HfSiO2 system was sampled along an approximate guess of the MEP. This trial MEP is based on the previous undoped MEP with the expectation that Si substitution would not change the MEP drastically from the undoped system. By taking a gaussian distribution about the mean of the trial MEP, the gaussian regression would sample near the probable MEP path and eventually arrive at a convergence without random sampling the complete PES. The result in figure 7 shows that although convergence is reached around 23 sample points, it is not enough of an improvement over random sampling to justify biasing the sampling pattern.

2.2 Sampling Shape Memory Binary Alloys

An optimal experimental design framework is currently being developed in conjuction with Dr. Vlassak's group at Harvard University in efforts to search the Cu-Zr based alloys for novel high-temperature shape memory alloys (HTSMAs). Part of this design framework involves sampling a large space of compositions. Due to a recent experimental observation of a martensitic phase with lower symmetry than B19', it was decided to build a database of energy landscape from other binary systems with propensity for B2-B19' transformations to try and identify trends and gain deeper insight into the variations in the energetics of the transformations. A recent paper by

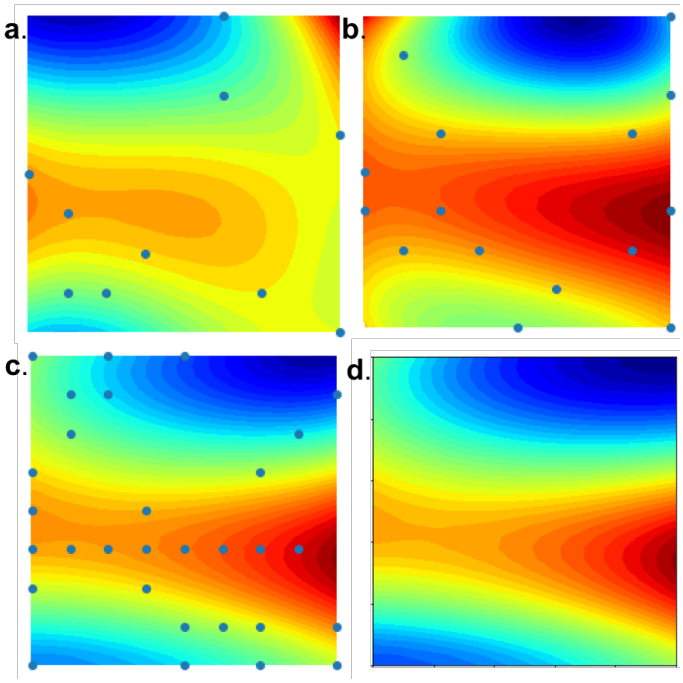

Figure 2.1: Lattice (x-axis) vs. Internal coordinates (atomic shuffle)

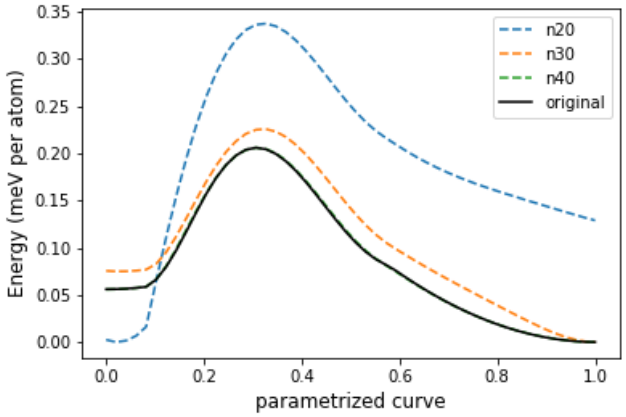

Figure 2.2: MEP convergence at different sampling resolutions in the HfO2 system

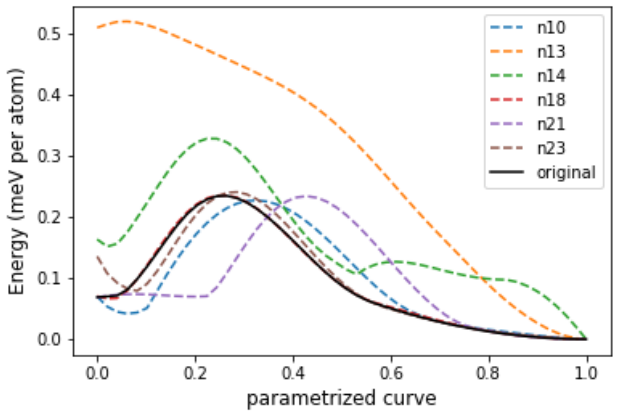

Figure 2.3: Convergence with biased sampling along the previous undoped HfO2 MEP in the HfSiO2 system

joohwi Lee, et al. [14], used first-principle calculations to screen 187 out of 6627 candidate shape memory alloys for optimal compatability conditions between the austenite and martersite phases. A high-throughput sampling of their candidate alloys is underway. Over 100 binary intermetallic alloys are being sampled concurrently within a 4-dimensional parameter space. This serves two objectives, one is as a benchmark to our goal of efficient large scale materials sampling and the other, and more importantly, is to develop predictive models from the large dataset. The dataset will come at a relatively low computational cost relative to the high number of degrees of freedom being sampled. Several factors, both in methodology and systems specific, help in reducing compute cycles. In methodology, the sparse optimal sampling scheme along with the use of Gaussian process interpolation are of considerable benefit and can flexibly fine-tuned as the need arises. Also, the simplicity of the binary structures allows for smaller supercells and systematically very similar structural transformations.

The figure 2.4 below shows a small subset of raw sampling points screened for the minimum energy at the symmetry points. A full analysis of the dataset is needed to further progress, but even a small fraction of the dataset plotted below already raises some questions, for instance, about the Ca2Tl6 system and its marked difference in energetic pattern from the rest of the structures. The

Binary Systems	Parent phase	2H martensitic phase
XY (10 structures)	B2 (Pm – 3m)	Pmma
X_3Y (101 structures)	DO_3 (Fm – 3m)	Pnma

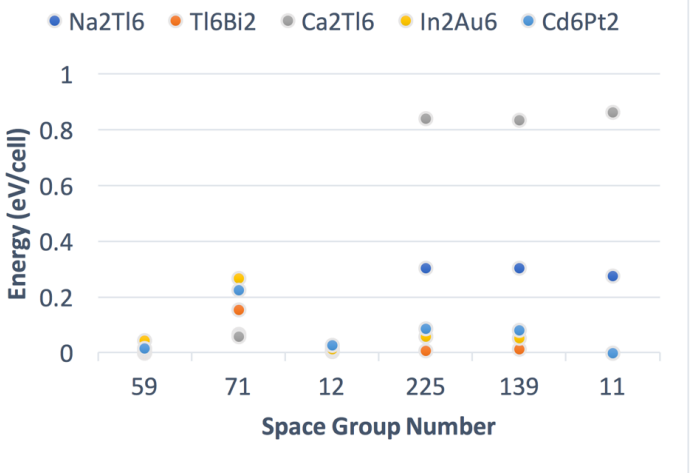

Figure 2.4: Representative subset of raw sampling points screened for the minimum energy at the symmetry points

full dataset will comprise of the 111 binary structures summarized in the table below along with necessary refinements and optimizations of minimum energy pathways.

2.3 Caculation Methods

2.3.1 Tungsten in the Presence of Oxygen Vacancies

Table 2.1: Rutile VO2, VO2W Oxygen Vacancy Comparison

System	Description	Ecell (eV per atom)	ΔF
$32_V\ 64_O$	No vacancy	-8.5775792	
$31_V\ 64_O\ 1_W$	No vacancy	-8.6171851	
$32_V\ 63_O$	Oxygen vacancy	-8.5909412	2.64785
$31_V\ 63_O\ 1_W$	Oxygen vacancy close to W	-8.6232964	3.37628
	Oxygen vacancy far from W	-8.6256125	3.15624

Table 2.2: Monoclinic (M1) VO2, VO2W Oxygen Vacancy Comparison

System	Description	Ecell (eV per atom)	ΔF
32_V 64_O	No vacancy	-8.5465130	
31_V 64_O 1_W	No vacancy	-8.5818206	
32_V 63_O	Oxygen vacancy	-8.5911944	-0.35855
31_V 63_O 1_W	Oxygen vacancy close to W	-8.6120943	1.04548
	Oxygen vacancy far from W		

Table 2.3: Stable elemental structures calculated from DFT

atom	E_i^0 (eV per atom)
V	-.89459010E+01
O	-4.6603379375
W	-13.00733398

Supercell total energies were calculated based on Density Functional Theory (DFT) as implemented in the Vienna Ab-initio Simulation Package (VASP). Thhe Generalized Gradient Approximation (GGA) under the Perdew-Burke-Ernzerhof (PBE) formalism was used for the exchange correlation. Pseudopotentials were generated by the projector augmented-wave (PAW) method and a cut-off energy of 533 eV for the plane wave basis was set. Optimized structures resulted as changes in total energy between steps were within 10-6 eV.

Supercells of 96 atoms were created for undoped and W-doped VO2 rutile and monoclinic structures. Formation energy of an oxygen vacancy in these structures were calculated with a vacancy concentration ratio of 1:95 atoms.

Formation Energy F (per cell) is calculated as follows:

$$F = E_{cell} - \sum_i n_i E_i^0$$

ΔF for an Oxygen vacancy in VO2:

$$\Delta F = \left(E_{cell}^{Vac} - \sum_i n_i E_i^0 \right) - \left(E_{cell} - \sum_j n_j E_j^0 \right)$$

$$\Delta F = \left(E_{cell}^{Vac} - (n_i E_V^0 + n_i E_O^0) \right) - \left(E_{cell} - (n_j E_V^0 + n_j E_O^0) \right)$$

where:

E_{cell} is bulk cell energy

E_i^0, the energy of ith atom reference state

n_i is the cell count of i$^{\text{th}}$ atom.

For Example, to calculate F for an oxygen vacancy in a 96 atom cell:

$$\begin{aligned} F^{vac} &= E_{cell}^{vac} - \sum_i n_i E_i^0 \\ &= E_{cell}^{vac} - 32E_V^0 - 63E_O^0 \end{aligned}$$

Similarly without vacancy:

$$\begin{aligned} F &= E_{cell} - \sum_j n_j E_j^0 \\ &= E_{cell} - 32E_V^0 - 64E_O^0 \end{aligned}$$

Finally ΔF:

$$\begin{aligned} \Delta F &= E_{cell}^{vac} - E_{cell} - 32E_V^0 - 63E_O^0 + 32EV^0 + 64E_O^0 \\ &= E_{cell}^{vac} - E_{cell} + E_O^0 \end{aligned}$$

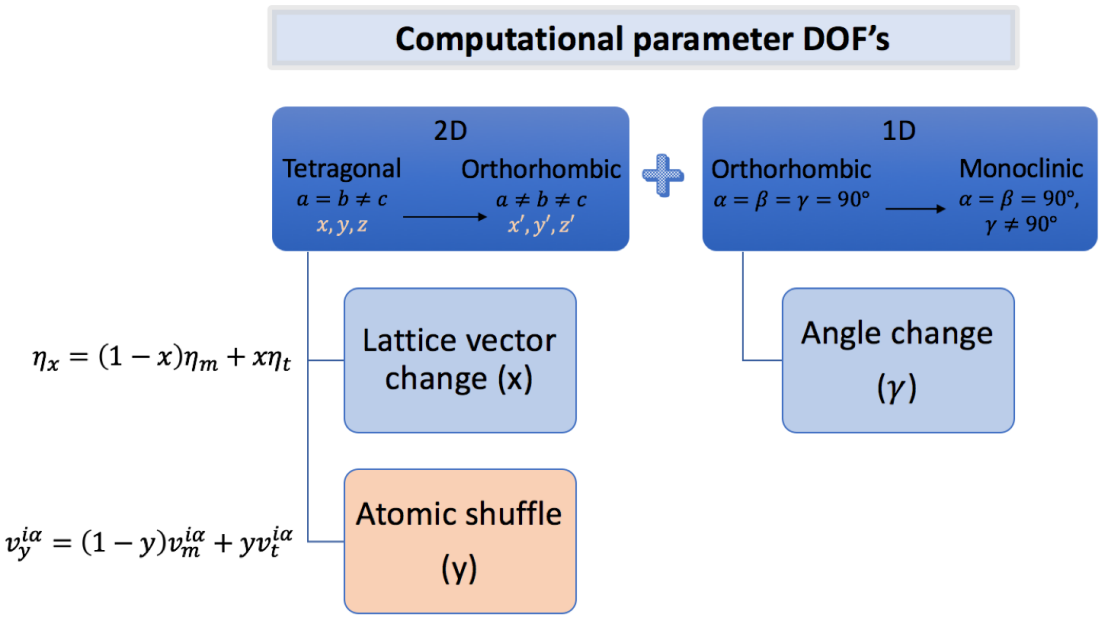

Figure 2.5: Structural degrees of freedom of energy landscape using 3D linear interpolation scheme

2.3.2 Parametrization

The HfO2 phase transition is described by a monoclinic to higher temperature tetragonal form. To model the transition, some assumptions were made in transforming the parameter space. Since minimal atomic movement is expected from the martensitic transition and the first nearest neighbor coordination does not change, then a uniform transformation of atomic coordinates is a reasonable approximation [10].

It is necessary to justify the linear approximation scheme used in transforming the parameter space. From a strict first principles point of view, the MEP is mapped out by both nuclear and electronic wave-functions. Along the MEP however, the system mostly remains in its electronic ground state and a Born-Oppenheimer type approximation can be taken to decouple the nuclear motion of the transition [15].

2.3.3 Density Functional Theory

Erwin Schrondinger's contribution to quantum mechanics is weighted with the same gravitas as Newton's laws of motion in classical mechanics. The time independent many-body Schrodinger equation defines the state of any system by a wave function Ψ. By choosing the initial conditions and solving for Ψ in the many-body equation 2.2 or more simply for the single-body equation 2.1, the observables of a system (i.e. physical properties) are calculated by linear operators on Ψ. In fact, everything about a system of any size can be known, including excited states, once the explicit functional form of Ψ is solved for. The price to pay for such generality is that no concessions are given to the computational limitations of solving it for complex systems, where solutions become intractable for even small molecules. It is a bit like establishing everything is knowable to the extent that all possible particle interactions in a system are solved for. It is not the intention to dismiss its importance but only to highlight the frustrations felt by the scientific community soon after. Most modern quantum codes in use today are based around approximating solutions of Schrondinger's equation and circumventing the many-body problem. Density functional theory (DFT) as formulated by Kohn along with Hohenberg in 1964 [16] provided a foundational basis for practical application of quantum mechanics in many fields of research. By establishing the existence of a functional of charge density $n(r)$ which when minized produces the same ground state charge density and energy as solving the many-body schodinger equation (Ψ); the theorems established a correspondence between a much simpler object, the average charge in space, and a much more complex many-body object, $\Psi(r_1, r_2..., r_N)$. This was a step in the right direction and was quickly followed up in 1965 by Walter Kohn and Lu Jeu Sham with the Kohn-Sham equations 2.3, 2.4 establishing a practical reformulation of DFT via a ficticious system of non-interacting particles. This fictitious system can generate an equal charge density to the interacting system. Thus allowing a return to the familiar Schrodinger equation in the form of single particle equations under an effective potential $\upsilon_s(r)$. By solving equation for all ϕ_i, which are themselves functionals of density ($\phi_i[n]$), a new charge density can be estimated using 2.4. This charge density can be used again to update the potential $\upsilon_s(r)$ and iterated until a convergence is reached. The

converged charge density can then be used to calculate energy from a similar density functional form originally introduced by Kohn and Hohenberg. The Kohn-Sham treatment is not an exact solution but holds the error of estimating the exchange-correlation functional. For many systems, the non-interacting functional terms are much larger sums than the exchange-correlation unknown and therefore still produce reasonably accurate property predictions. Modern treatments of DFT such as linear density approximation (LDA), generalized gradient approximation (GGA) [17], meta-GGAs and DFT+U [18; 19; 20] methods rely on formulating better approximations of the electronic density and functional forms to account for system dependent coulombic-exchange interactions. There has been extensive study about the accuracy of such DFT approximation methods in estimating reaction energies, phase stability, and structural parameters [21; 22]. This communicates a challenge to DFT practitioners that must navigate many pitfalls of interpreting theoretical results incorrectly due to being unaware of the limitations.

$$\left[\frac{\hbar^2\nabla^2}{2m} + \upsilon(r)\right]\Psi(r) = \epsilon\Psi(r) \tag{2.1}$$

$$\left[\sum_i^N \left(-\frac{\hbar^2\nabla_i^2}{2m} + \upsilon(r_i)\right) + \sum_{i<j} U(r_i, r_j)\right]\Psi(r_1, r_2..., r_N) = E\Psi(r_1, r_2..., r_N) \tag{2.2}$$

$$\left[-\frac{\hbar^2\nabla^2}{2m} + \upsilon_s(r)\right]\phi_i(r) = \epsilon_i\phi_i(r) \tag{2.3}$$

$$n(r) \equiv n_s(r) = \sum_i^N f_i \left|\phi_i(r)\right|^2 \tag{2.4}$$

2.3.4 String Method

The string method for finding MEPs requires an initial trial string path between starting and ending structures. Usually this is just a straight line with equally spaced images along its length. The path γ is updated using a gradient formulation as follows:

$$\varphi = -[\nabla V(\varphi)]^{\perp} + r\hat{t}$$

where $(\nabla V)^{\perp} = \nabla V - (\nabla V, \hat{t})\hat{t}$ is the gradient of the potential perpendicular to ∇, $\hat{t}$ is a unit tangent vector along the string. Also, r is a lagrange multiplier that has to be defined along with a constraint equation to parametrize the string. This parametrization helps numerical stability when evolving the string. The original paper by Weinan et. al. can be found in the references [23] for a detailed look at the method.

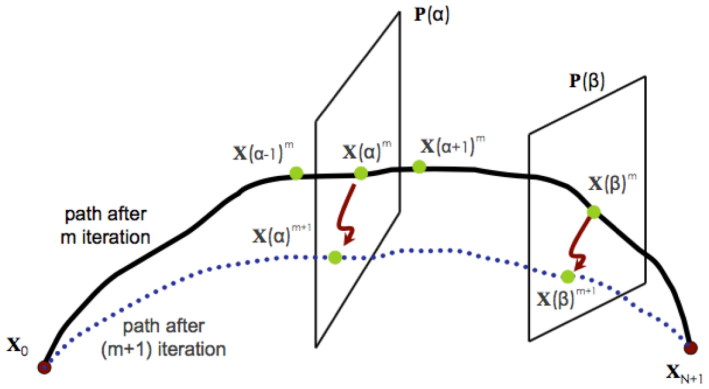

Figure 2.6: A schematic of the string optimization which relaxes $X(\alpha)^m$ to $X(\alpha)^{m+1}$ along the perpendicular planes to the path.

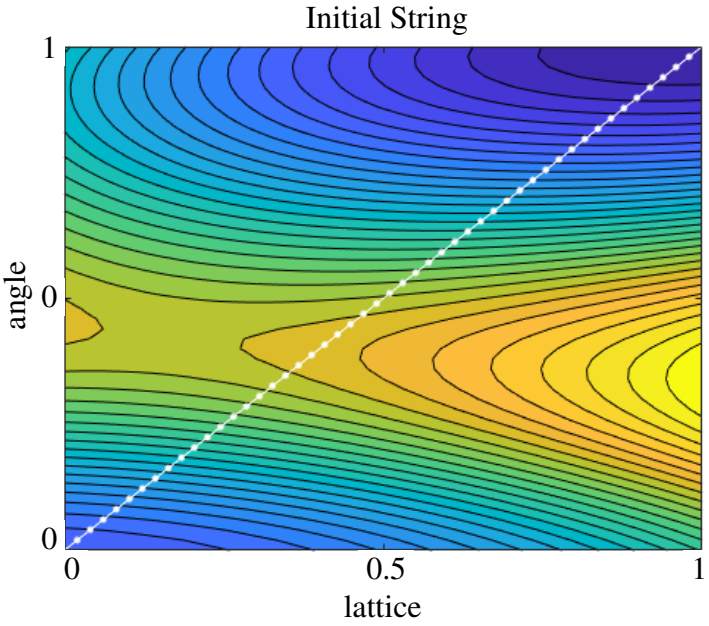

Figure 2.7: Initialization

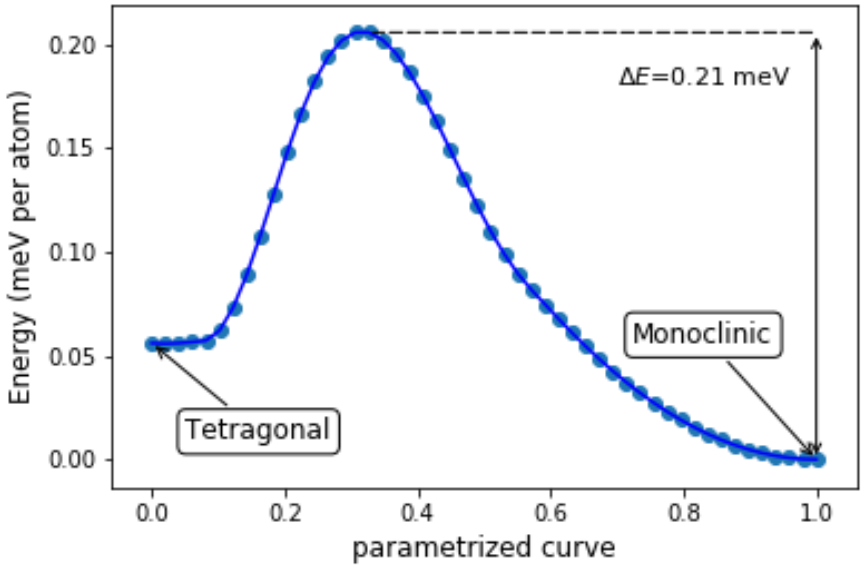

Figure 2.8: HfO2 activation barrier

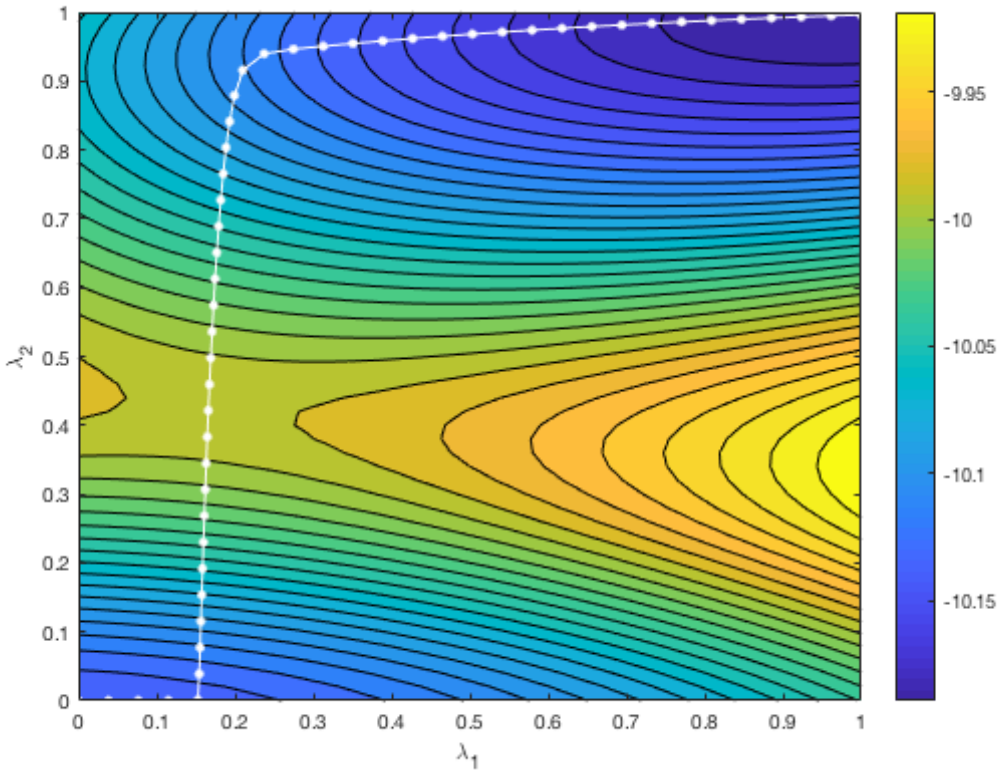

Figure 2.9: HfO2 MEP

3. COPPER ZIRCONIUM ALLOYS AND HTSMA DATABASE

3.1 CuZr Martensitic Transformation

3.1.1 Introduction

Shape memory alloys (SMAs) undergo a displacive martensitic transformation and have the ability to recover large strains as a response to either temperature change (pseudoplastic) or external stress load (pseudoelastic effect). Both mechanisms of deformation form martensitic variants that hold shape and then transform back into non-variant Austenite to recover original shape. The desired material response depends on maintaining proper operating temperature below Martensite finish temperature M_s, or above Austenite finish temperature A_f, respectively. Shape memory alloys that transform at temperatures above 100C, commonly referred as high temperature shape memory alloys (HTSMAs), Interest in HTSMAs has grown extensively due to increasing demand from Aerospace, military and private companies seeking to reduce bulk weight of performance parts as well as reduce component failure of smart functional devices.

Under hot corrosive environmental conditions, HTSMAs begin to offer significant practical advantage over traditional metals. Specifically, the large strain recovery of HTSMAs would allow superior resistance to plastic deformation while simultaneously reducing design tolerances. Commercially viable HTSMAs remain unrealized due to their enhanced susceptibility to creep, plastic deformation during cylcing, and incomplete shape recovery. In general, a higher Tc decreases the energy barrier to generating slip dislocations as they are faciliated by thermal ativation. Evidently, HTSMA function is particularly sensitive to energetic terms associated to the mechanism of the phase transformation. This work presents the results of a computationally guided experimental study on the effect of alloying elements (X=Co,Ni,Ti,Hf) on the transformation temperature of CuZr-X. The twin boundary energy terms are identified as important criteria that can be used to pre-select alloying elements for the discovery of HTSMAs. An energetically favorable transformation pathway is proposed with robust confirmation by three separate methods of analysis.

Furthermore, a new theoretical ground state martensitic structure is identified as well as several possible metastable structures that could help explain the selection mechanism of martensite in CuZr.

CuZr has been studied extensively due to dual ability to form bulk metallic glass and undergo martensitic transformation [24]. In crystalline form, CuZr exhibits high strength, and good corrosion resistance [25]. The stable austenitic temperature is well above 100C which makes CuZr an ideal HTSMA candidate. The parent phase of binary CuZr is B2, sharing the prototypical form found in NiTi [CsCl with Pm-3m space group no. 221]. NiTi B2 has been reported to have unstable phonons by nikolai et al. Similarly we have identified CuZr to have phonon instabilities originating at kpoint (1/2, 1/2, 0) of the brillouin zone as seen in Figure 3.7.

It took 25 years after the discovery of pseudoelastic behaviour in Au-Cd alloys to identify the first commercially successful shape memory alloy (SMA), NiTi (Nitinol) [26]. Wang and Buehler characterized its properties, noting an increase in ductility at colder temperatures, a drastic increase in hardness at 166C (Tc) for an equiatomic ratio of Ni:Ti, perfect shape memory, and a rapid drop in Tc with off-stoichiometric compositions. NiTi found some of its first commercial success in orthodontics as arch wires in braces. The superelastic regime of NiTi gives a constant stress-to-strain response that reduces the number of wire adjustments necessary to accommodate dental alignment. The NiTi martensitic transformation (MT) serves as a good model system for study of thermoelastic response near room temperature but its applications are limited in scope owing to high cost of manufacturing, problematic chemical reactivity, and functional degradation caused by cycling fatigue.

3.1.2 Results

3.1.2.1 Phonons and Pseudosymmetry

Zhou et al. [1] employed the use of DFT to calculate the relative formation energies of various candidate martensitic structures and found the B33 structure compared well with XRD measurements. They stipulated that the cm structure identified by Schryvers [27] was likely the orthorhom-

bic Cmcm No. 63 (B33) so they proposed the CuZr martensitic transformation as B2 $\rightarrow$ (B19' + B33). Figure 3.8 shows stable phonon dispersion curves calculated for the B33 orthorhombic phase. Zhou however calculates the formation energy of B33 to be lower (more stable) than B19' by 0.2 KJ/mol. We calculate B19' to be more stable than B33 by -0.45 KJ/mol. Furthermore, symmetry analysis using structure relations tool on the Bilbao Crystallographic Server (BCS) [28] fails to match Wyckoff positions of B33 to the experimental description of the Cm (No. 8) super structure. Therefore, we can conclude B33 will likely not be found paired with Cm as some experimental findings suggest Cm martensite as a superstructure for B19'.

3.1.2.2 Phonons and Pseudosymmetry

It should be mentioned that B2 and Cm have a spacegroup index relationship of 96, which can be calculated by multiplying the ratio of point group orders with the ratio of formula units (48/2)x(4/1). Although they are group-subgroup related, due to a high index, there can be 100's of maximal pathways that could relate the phases. In order to resolve competitive transition pathways, the unstable phonons of B2 were frozen into the structure and used as a branch point to follow the phase transition. This step is repeated until a stable phase is found or the loss of symmetry falls below Cm. A similar approach was introduced by Togo for simple systems [29]. Given the complexity of phase selection reported in CuZr [24] and the large index, an additional procedure to the phonon following method was implemented that facilitated grouping closely related structures by pseudosymmetry. The benefit of this approach is that closely related branch points of higher symmetry missed by a downward search of phonons can be identified and explored further. This approach draws inspiration from the erickson-pitteri neighborhood concept defining the close proximity of variant sets of small deformations as mapped under the parent group operations. Figure 3.10 shows groups of explored branch points with downward arrows representing the phonon search pathway and upward arrows are new structures identified by pseudosymmetry. These structures are proximal to lower symmetry branch points by small deformations and atomic shuffles.

3.1.2.3 Ground State Structure

Figure 3.9 shows a newly discovered ground state structure, labeled as B19" and a close pseudosymmetric orthorhombic B19 (No. 51) by a small angle distortion $\Delta\beta = 0.105$ and along with a slight volume decrease (0.07%). Interestingly, the two stable structures, No. 63, and No. 65, cannot directly subduce the Cm structure. Both Cmm2 (No. 35) and B19 (No. 51) can subduce Cm however. There are two irreps associated with generation of Cm and B19'. In fact, symmetry mode analysis shows that B19 (No. 51) can induce both martensites. B19' can result from shearing of Zr atomic planes in the (a) direction of Irrep GM3+ , while Cm is generated by an atomic shuffle with an irrep R1 in the (a,a) direction of kpoint (1/2,1/2,1/2).

3.1.2.4 Tranformation Pathway

SSNEB was used to compare the minimum energy pathways between B2$\rightarrow$ B19' and B2$\rightarrow$ Cm. The lattice and atomic correspondence augmented matrices that takes B2 to the martensite basis for B19' and Cm are respectively [15]:

Figure 3.11 shows comparison of neb pathways for the B2$\rightarrow$ B19' and B2 $\rightarrow$ Cm transition. The B2$\rightarrow$ Cm path shows a barrierless transition to an intermediate structure with Cmm2 (No. 35) symmetry. The loss of symmetry is dominated by atomic shuffling with no shearing of the lattice. The rise of the barrier corresponds to shearing of the Cmm2 lattice towards the monoclinic angle (90 $\rightarrow$ 105) and it reaches a maximum energy just slightly above the B2 phase. The low energy barrier of a direct transition from B2$\rightarrow$ Cm is in agreement with experimental detection of Cm martensite.

Structural Analysis tools from BCS [30] were used to analyze the symmetry modes compatible with the B2 distortion for both martensites. This is accomplished by first determining the lattice correspondence that minimizes global strain distortion between austenite and martensite, and then finding compatible symmetry-adapted modes relative to martensite. While this is a sensible approach, precaution should be taken; A correspondence based on prioritizing minimal global distortion does not gaurantee the lowest energy interpolation of atomic shuffles since there can

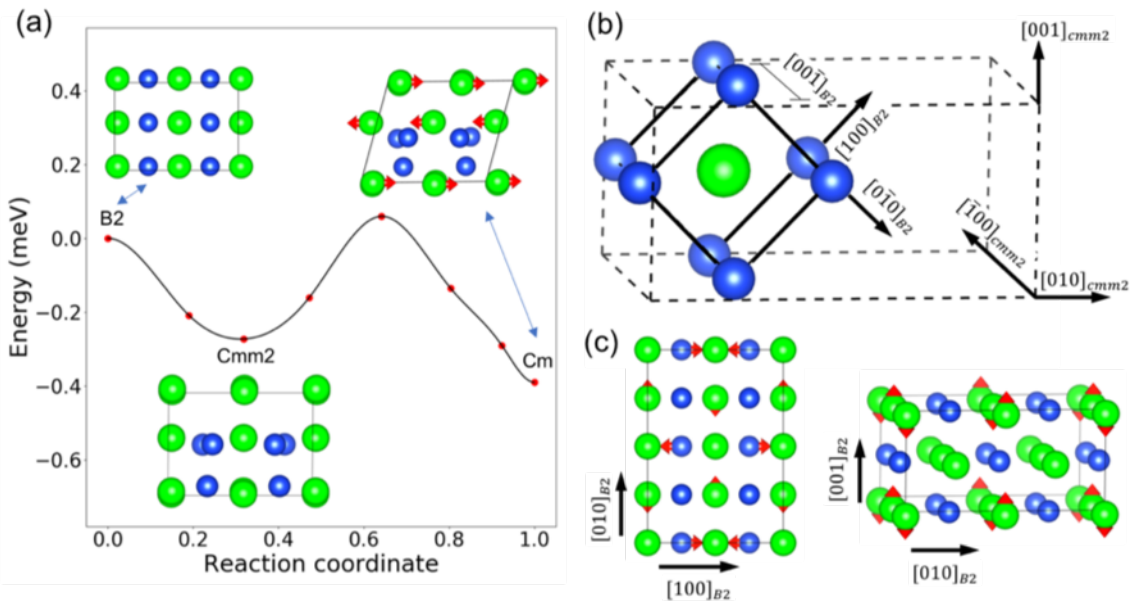

Figure 3.1: Correspondence between B2 and Cm phase [32]

exist alternative lattice correspondences that do not necessarily minimize strain but might reduce the overall energy barrier of MT. In order to mitigate some doubt, the structural symmetry modes obtained from BCS were compared to the unstable phonon modes to ensure the atomic shuffle is compatible with a reduction of energy. The lattice correspondence suggested by BCS structural relations tool is shown in Figure 3.1. The symmetry adapted distortions of B2→ B19' and B2→ Cm show in Fig. 3.1c are in agreement with a B2 phonon softening mode at the M point of the Brillouin zone.

3.1.2.5 Evaluation of Phase Stability in CuZr-X (X=Ni,Co,Hf)

Shape memory alloy (SMA) compositions can span the range of intermetallic elements and display many common features found in martensitic systems; Such as martensite twin formation, discontinuous change in lattice parameters (first-order), hysteresis, and non-diffusive displacement of the atoms. They derive special value however owing to their non-linear elastic properties; Granting them macroscopic shape recovery, high reversibility, large pseudoplastic strains, and motor less actuation. The scope of SMA applications has been limited predominantly by the degradation of

functionality during cycling especially at higher transformation temperatures (> 390K). HTSMAs can be prone to strain hardening due to generation of slip dislocations, brittle behavior, incomplete shape memory and plastic deformation during processing due to lowering of yield stress. Recent foundational development on the geometric theory of martensite has established methods for quantitative analysis of twin morphology based on compatibility conditions within the parent matrix. The conditions of lattice compatibility are known as the cofactor conditions. Particular interest is given to the condition associated with the middle eigen value $\lambda_2 = 1$ of the stretch matrix U which has been associated to sharp drops in hysteresis [6]. Defect generation due to accumulated macroscopic stress from lattice incompatability can be mitigated by shifting λ closer to 1 by the addition of alloying elementsi [31] but there is currently no general guideline for predicting alloying effects on the transformation temperature or hysteresis.

The following discussion details the computational evaluation of alloying effect on the relative phase stability between B2 austenite (A) and Cm martensite (M) phases of CuZr. The work was performed as part of a collaborative effort for the accelerated discovery of HTSMAs [32]. All experimental values referenced in the following discussion originate from the cited work unless otherwise stated. Computational goals of the work included; Offering guidance on alloy concentration range, selection of alloying elements [X=Ti, Ni, Co, Hf, Cr] in CuZr-X likely to increase Tc, and identify the most relevant energetic terms to help bring the theoretical model into alignment with experimental outcome. Experimental measurements of Tc were evaluated on CuZr-X thin films by nanocalorimetry [32]. The MT hysteresis was evaluated from DSC curves as the difference between the observed heating and cooling transformation temperatures.

The structure of martensite was determined to be the monoclinic Cm as previously reported by [27]. The effect of alloying elements on Tc are estimated from DFT by comparing the energy difference between martensite and austenite (M-A). A more negative value of M-A represents an increase of martensite stability relative to austenite and corresponds to an increase in Tc. While a more positive value (less negative) of M-A suggests a decrease of Tc. Figure 3.2 shows evaluation of M-A energy on the trial list of elements as a function of concentration. With the exception of

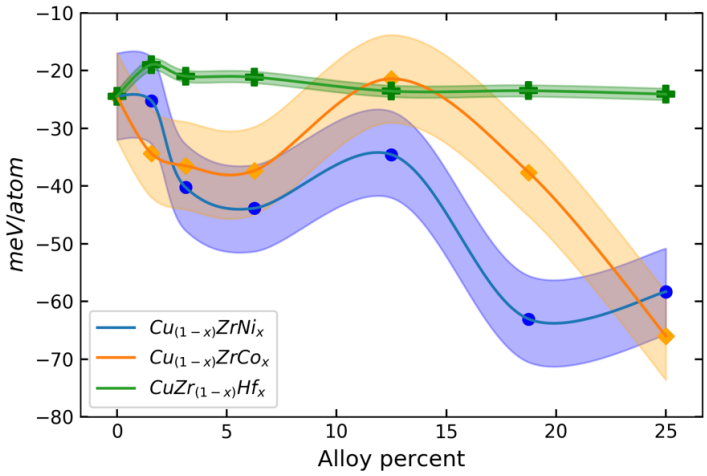

Figure 3.2: Energy difference between martensite and austenite is shown for CuZrX (X=Ni,Co,Hf). The standard deviations in meV are represented as colored bands for each composition. The deviations are a result multiple DFT simulations for each composition while varying the atomic site replacement to account for the effect of periodic boundary conditions.

Hf, all elements considered replaced Cu. The non-linearity in the trend lines are likely due to the limitations of supercell size and periodic boundary effects. As expected, the M-A for pure CuZr starts in the negative range since martensite is more stable than austenite. M-A is positive for Cr concentration above 6% making B2 the stable phase. Hf shows monotonic effect on phase stability while Ni,Ti, and Co stabilize Cm (increase Tc). To mitigate the effects of periodic boundary conditions from simulations, site subsitutions were varied for each composition according to unique site symmetries and maximum separation distance between alloying elements within the supercell. The average standard deviation of M-A (meV) based on averaging deviation for all concentrations for Co, Ni, and Hf are 7.5, 7.6, and 0.1, respectively.

3.1.3 Discussion

In Figure 3.2 Co is predicted to increase the negative value of M-A and therefore should increase Tc. The experimental results shown on Figure 3.6 contradict the theoretical prediction for Co alloying element with the addition of 5% Co causing a decrease in Tc by about 10K. Clearly,

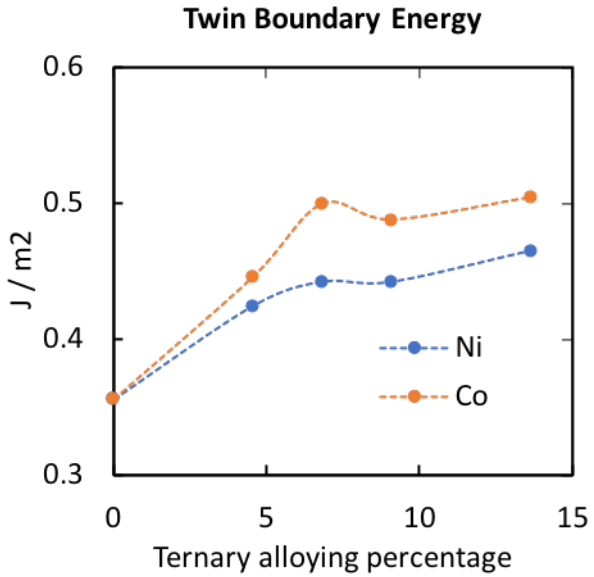

(a) (021) twin boundary energy

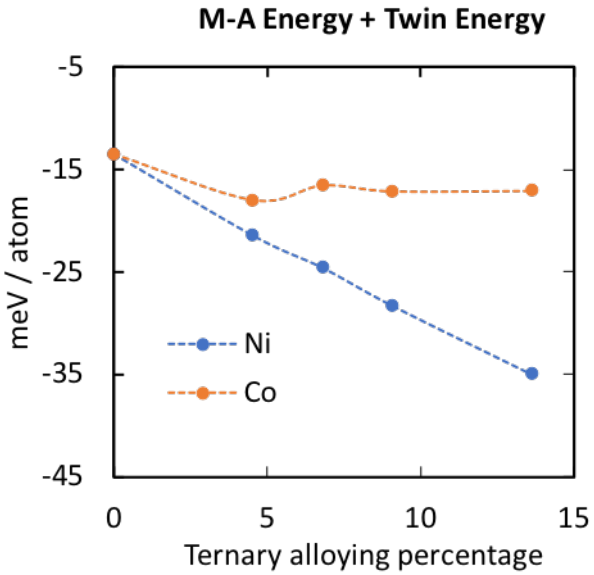

(b) Twin boundary energy added to M-A energy

Figure 3.3: (021) twin boundary energy terms [32]

only considering M-A energy is too simplistic and fails to capture the underlying physics that could affect Tc beyond the thermodynamic phase stabilities. TEM images [32] of CuZr-X showed finely spaced twinning structure which could mean that large strains are being accomodated. The effect

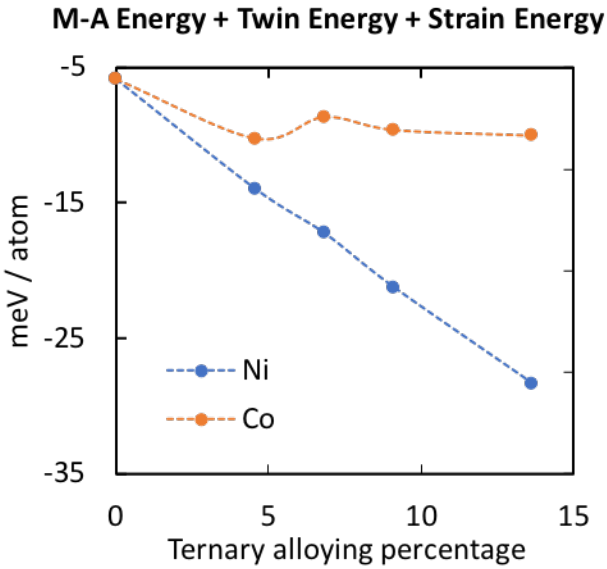

Figure 3.4: Twin strain energy term included in the analysis of boundary energy on M stability relative to A [32]

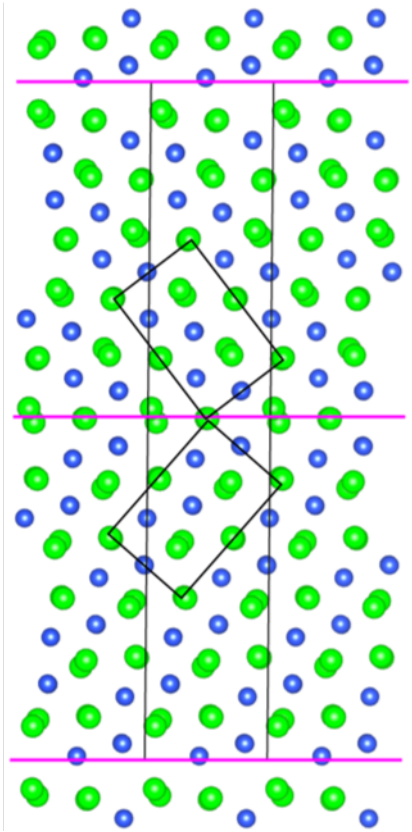

Figure 3.5: An 88 atom supercell was constructed with the (021) twin plane parallel to the (001) plane of the supercell. The smaller rectangles represent the conventional Cm unit cell mirrored across the twin plane [32].

of a large number of fine twins can possibly shift the energy balance between accomodation and energy cost creating twin boundaries.

Formation of M twin boundaries increases the energy barrier of transformation on cooling which decreases M stability compared to A. The arrangement of twins in a microstructure is a result of the balance between two energetic terms; The twin boundary energy, and strain energy. A large elastic strain will decrease twin spacing and increase total area of twin boundaries. The compatability strain energy for a twin plate of width t is

$$E_{strain} = 2 * \frac{1}{2} Y (1 - \lambda_2)^2 * \frac{\pi t^2}{4},$$

where the elastic modulus of CuZr is taken as 75 GPa[]. Then the total energy per unit volume of M can be approximated by

$$E_{Total} = \frac{1}{td}(E_{Strain} + \gamma d),$$

where γ and d are the twin boundary energy per unit area and width of the twin plate, respectively.

To evaluate twin boundary energy by DFT, the twin plane must be aligned parallel to two planes of periodic boundary conditions and perpendicular to all the other planes. Modelling the (021) mirror plane poses a geometric challenge under periodic boundary conditions. It is not possible to form a supercell with the (021) plane perpendicular to all other planes without approaching an infinite supercell size. So we have chosen an 88 atom supercell as shown in Figure 3.5, with approximate perpendicular angles of $\alpha = 90.3781°$ and $\beta = 90.5613°$. The surface structure of (021) was modelled from the TEM analysis by Seo et al. [27]. Figure 3.3a shows the twin boundary energy for addition of Ni, and Co as a function of concentration. Both Ni and Co increase the twin energy as compared to pure CuZr. Figure 3.3b shows the effect M boundary energy (converted to meV/atom) on the relative stability of M-A. The addition of Ni is predicted to increase the stability of M at a much faster rate than Co. Figure 3.4 shows the addition of strain energy to the total energy of M as calculated by Miao et. al. using the λ_2 values estimated from DFT.

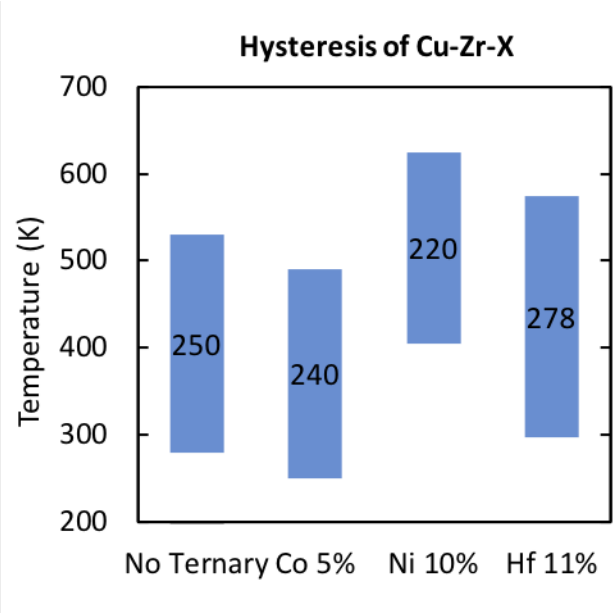

Figure 3.6: Hysteresis of M-A and A-M transformation peaks. Each bar represents the range between the M-A peak and A-M peak. The numbers are the measured hysteresis ($\pm$ 10 K error) [32].

The addition of twin boundary energy terms results in significant differences in energy between martensite and austenite that show a strong dependence on alloying composition. After accounting for alloying effect on twin bounday energy and strain, the theoretical predictions are brought into closer agreement with experiment. The results of this work infer that boundary energy should be evaluated in guiding alloying selection to other systems exhibiting fine martensitic twin formation.

3.1.4 Methods

The climbing image nudged elastic band (cNEB) method: The cNEB has been utilized to explore the possibility of new ground state or metastable crystal structure from carbon-nitride family. The initial and final states must be known to start cNEB, which then provides minimum energy structure (if any). The cNEB performs linear interpolation between the initial and final states and minimizes the energy the chosen images between end point structures [15].

Structural and electronic relaxation- We use first-principles density functional theory as implemented in Vienna Ab-initio Simulation Package (VASP) [33]. The Perdew, Burke and Ernz-

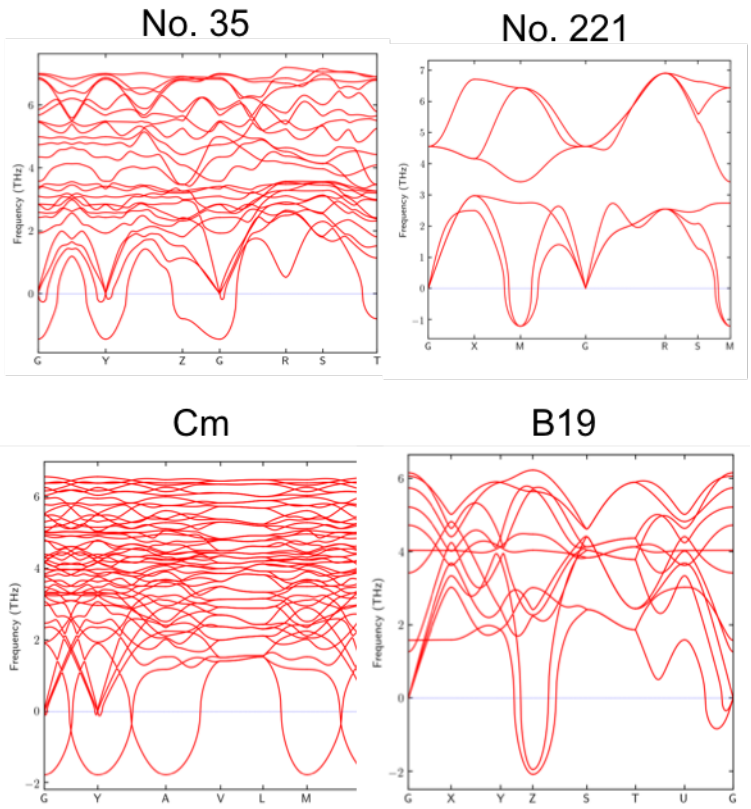

Figure 3.7: 0K Phonon dispersion curves for intermediate No. 35, martensites Cm, B19, and austenite No. 221

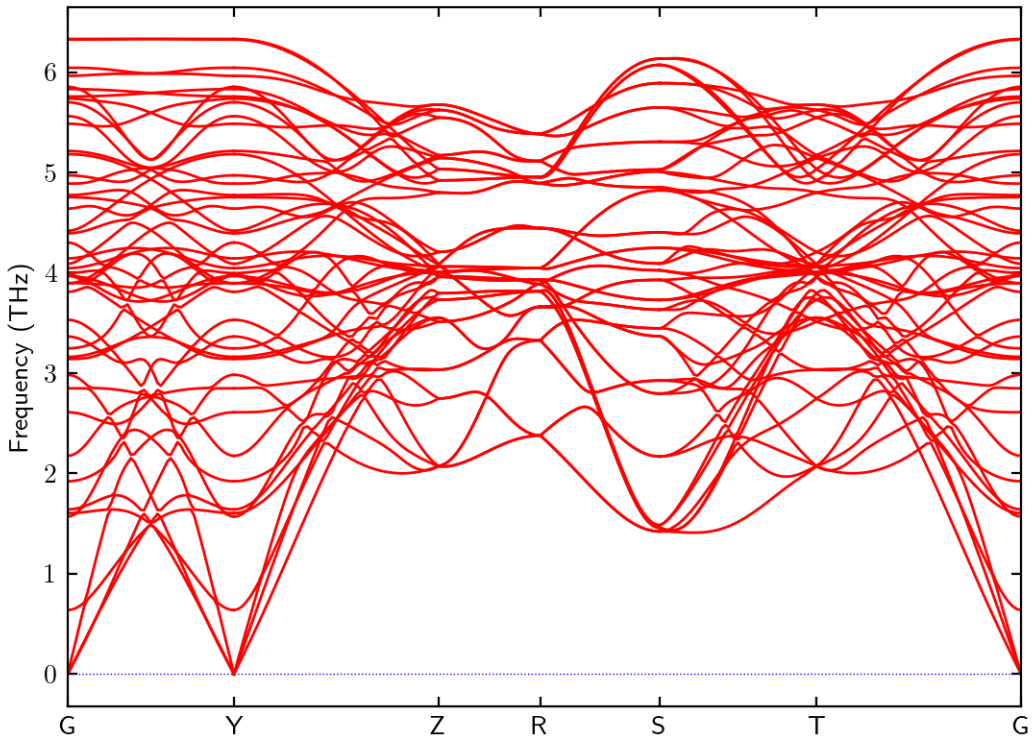

Figure 3.8: 0K Phonon dispersion curve for B33 structure proposed as martensite by Zhou [1] shows stable phonons

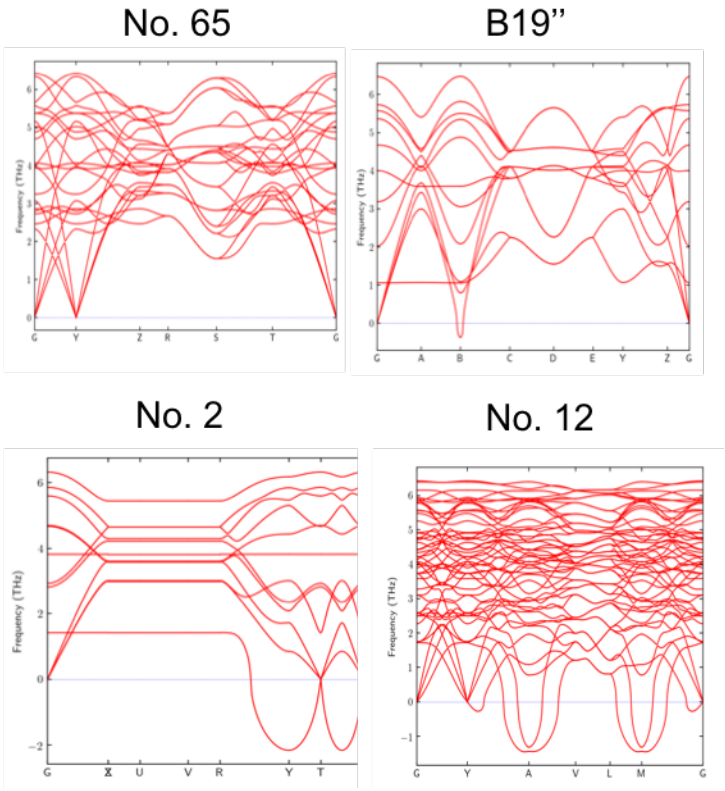

Figure 3.9: 0K phonon dispersion curves found by structural search of energy landscape

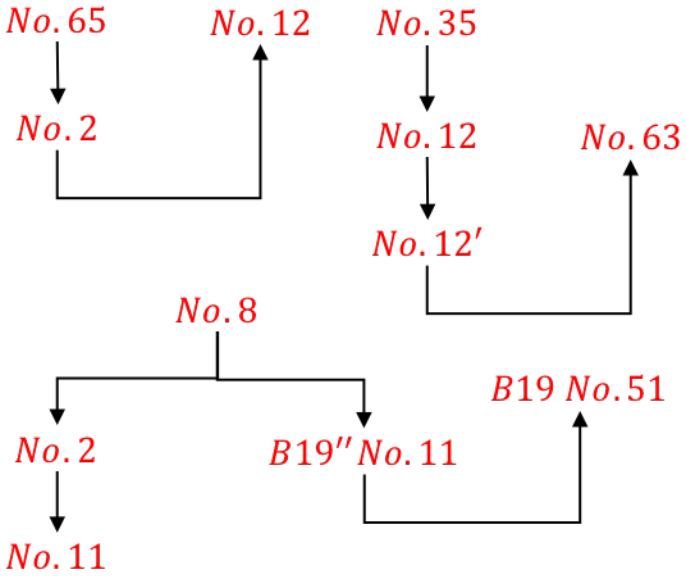

Figure 3.10: Transition related structures traversed by downward search (by phonon instability) and upward search (by pseudosymmetry)

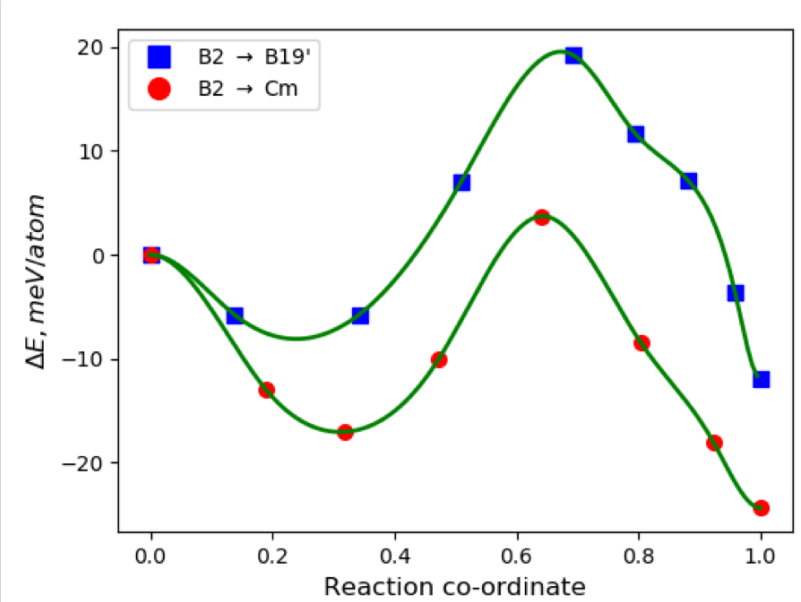

Figure 3.11: Comparison MT energetic barriers [32] between pathways B2 → B19' and B2 → Cm as calculated by SSNEB.

Table 3.1: DFT calculated lattice parameters of CuZr-X (X=Co,Hf,Ni)

Unit in	Alloying percentage	Austenite B2			Martensite Cm			
		a	b	c	a	b	c	gamma
X=Co	1.56	6.58	9.22	4.61	6.59	8.27	5.28	102.8
	3.13	6.61	9.18	4.59	6.59	8.28	5.24	102.45
	6.25	6.63	9.12	4.59	6.6	8.3	5.2	102.17
	12.5	6.51	9.4	4.49	6.66	8.23	5.21	103.63
	18.75	6.46	9.31	4.52	6.64	8.22	5.16	103.07
X=Hf	1.56	6.57	9.23	4.61	6.52	8.3	5.35	103.63
	3.13	6.56	9.23	4.62	6.52	8.3	5.34	103.35
	6.25	6.56	9.18	4.63	6.52	8.31	5.32	103
	12.5	6.51	9.25	4.61	6.51	8.29	5.32	103.48
	18.75	6.56	9.19	4.56	6.57	8.21	5.28	103.46
X=Ni	1.56	6.58	9.22	4.61	6.53	8.29	5.35	103.69
	3.13	6.54	9.24	4.62	6.59	8.26	5.27	102.78
	6.25	6.59	9.19	4.6	6.59	8.27	5.24	102.5
	12.5	6.34	9.76	4.46	6.58	8.25	5.24	103.01
	18.75	6.57	9.14	4.57	6.6	8.25	5.18	102.31

erhof (PBE) generalized gradient approximation is used with with a cut-off energy of 533 eV [4]. The gamma-centered Monkhorst-Pack [34] k-mesh of 7x9x7 and 13x17x13 is used for Brillouin zone integration during geometry-optimization and charge self-consistency, respectively. Total energies and forces are converged to 10-5 eV/cell and -10-5 eV/Å, respectively. We calculate structural property (cell parameters, bond-length, bond-angels), formation energy, electronic-structure (density of states, bands, bandgap), and elastic-parameters on optimized Pm-C4N3 (z=2, 14 atoms/cell).

3.1.5 Conclusion

The CuZr-X system displays many interesting properties useful for application due to good corrosion resistance, high hardness, good ductility of martensitic phase and the ability to display shape memory effect at high Tc. There are many unresolved aspects about its transformation behaviour and sensitivity to strain conditions on the cooling transformation cycle. This work has laid out a comprehensive overview of the various phases in CuZr-X and their relation grouping based on symmetry and pseudosymmetry. We have determined that DFT can serve as an effective guide for highthroughput phase discovery if all the proper energetic terms are included in the analysis. We identified the importance of considering twin boundary energy, strain energy, and composition on the overall effect of hysteresis. Particularly the low symmetry phase Cm has many closely related energy minimas within proximity that can be selected based on strain conditions of the transformation.

3.2 HTSMA Database

3.2.1 Introduction

Density functional theory (DFT) is expediently becoming an integral part of collaborative research where experimental efforts are either too expensive, need qualitative confirmation, or are near impossible to undertake. Recent advances in computational power and cost has made high throughput screening of material properties a tangible strategy for creating autonomous materials discovery frameworks (AMDF) but due to the practically infinite material search space, the imple-

mentation of screening algorithms requires tailoring the sampling methodology so that it navigates the search space in an informed manner.

Current efforts to reduce the exploratory expense of these calculations builds on a framework to reduce computational cost via smart regression sampling of the energy landscapes in martensitic transformations.

The following work details the methods implemented to sample and analyze a comprehensive database of binary alloys for the accelerated discovery of high temperature shape memory alloys (HTSMAs).

SMAs undergo a displacive martensitic transformation and have the ability to recover large strains as a response to either temperature change, external stress load and applied magnetic fields in the case of magnetic SMAs. Both mechanisms of deformation form martensitic variants that hold shape and then transform back into non-variant Austenite to recover the original shape. The desired material response depends on maintaining proper operating temperature below Martensite finish temperature, or above Austenite finish temperature, respectively. Much research has focused on the Ni-Ti SMAs due to their high quality applications in the medical industry as well as for stress or temperature induced actuators.

Shape memory alloys have many possible applications in modern technology ranging from self-actuating components, robotic movements, shape recovery of damaged components, alternative energy solutions, thermo-responsive fitting ligatures, smart nano-devices, aerospace flight components and many other unforseen uses. The discovery of just a few HTSMAs with good mechanical performance and long-term stability would have a lasting technological impact. The mathematical constructs describing SMA transformation twinning are well developed at least geometrically and the algebraic methods are laid out rigorously from several authors [35; 36; 37]. Less well understood is the dependence of hysteresis on the energetics of the transformation pathway [38], and the contributing effects of alloying compositions on the lambda condition. Hysteresis is closely related to the energetic efficiency of a martensitic transformtion. The delicate balance between coherent phase coexistence and kinetics, elastic transition layers between M and A, and

dynamic evolution of defects during thermal cycling are all topics of current research. In general, it has been established that when the cofactor conditions between M and A are met, the detectable hystersis drops sharply and the mitigation of defect generation alloys good reversibility of the transition. The 3 main cofactor conditions of lattice compatibility are: (1) det U = 1, where U is a matrix representing the pure homogeneous stretch strain of the lattice parameters; (2) $\lambda_2 = 1$, as the second largest eigenvalue of U; (3) $\hat{a}\dot{U}_1 cof(U_1^2 - I)n = 0$. The third condition is required by the coherency requirement of the surface connecting twins. The det U = 1 means there is no net volume difference due to the stretching or contracting of lattice parameters. The λ_2 =1 condition allows for the existance of a compatible interface between A and a variant of M. Together, the cofactor conditions imply the existence of an energy minimizing process where many compatible interfaces can be generated between twinned M and A. In reality, the minimization process must contend with several intrinsic material properties endowed by the crystalline arrangement of phases along grain boundaries.

Bucsek et. al. noted that hysteresis is also highly sensitive to aging and preprocessing parameters and brought into question the generality of λ_2 as the sole predictor of hysteresis. [7]. The evidence from experiments is clear in that there is strong correlation between hystersis and λ_2 = 1.

3.2.2 Results

Given that the lamda coniditon is inexpensive to calculate and correlates strongly with low hystersis and hence good reversibility, we have implemented a simple formulation for the prediction of λ_2 values in ternary compositions using only binary compositions. The formulation relies on exploiting combinatorially related binary structures generated in construction of the database. For every binary composition AB there are associated binaries AX and BX, where X can be considered the alloying element totally replacing A or B. The λ_2 value is then determined for all concentrations between the range AB and AX by a weighted sum of the individual contributions of binary parts in $AB_{1-c}X_c$. Taking the minimum concentrations $C_{AB} = \min|1, 1-c|$ for AB, $C_{AX} = \min|1, c|$ for AX, and $C_{BX} = \min|1-c, c|$ for BX, as the representative weights of binary components in the ternary composition the λ_2 can be predicted by:

Table 3.2: Prediction of λ_2 values for TiNi-X

	at%	Fe (λ_2)	Hf (λ_2)	Pd (λ_2)	Mn (λ_2)	W (λ_2)
0	0.040	0.915	0.917	0.918	0.913	0.919
1	0.100	0.916	0.920	0.922	0.912	0.925
2	0.160	0.917	0.922	0.925	0.910	0.929
3	0.220	0.917	0.924	0.927	0.909	0.933

$$\frac{C_{AB}}{C_{AX}+C_{BX}} \cdot \lambda_{2AB} + \frac{C_{BX}}{C_{AX}+C_{AB}} \cdot \lambda_{2BX} + \frac{C_{AX}}{C_{AB}+C_{BX}} \cdot \lambda_{2AX}$$

Figure 3.12 shows the predicted trends for $lambda_2$ in $Ni_{1-c}TiX_c$ for alloy concentrations up to 20. The dotted vertical line marks the base value of λ_2 for NiTi binary alloy calculated from database structures. Here can see that Pd alloying element has strong tendency to raise the λ_2 value. This is a consistent prediction with experimental evidence [39; 7]. It can also be seen that Mn is predicted to lower the compatability of M and A. This is also consistent with experimental observations that Mn lowers the martensitic start (M_s) temperature by about 70K per atomic percent [40]. The depressed M_s on cooling could be the result of increased incompatability between M and A which is directly correlated with creation of elastic stresses during transformation. It is also possible other factors like oxidation of the samples could lower (Tc) but the authors observed a greater rate of M_s depression when compared to A_s depression.

Figure 3.13 shows a plot of λ_2 predictions for FeNi-X(Co,Mn,Pt,W) for a range of alloying concentrations. The dotted vertical line marks the λ_2 for the pure binary FeNi. The plot shows clear trends for either increasing λ_2 or decreasing. The addition of Pt is predicted to inrease λ_2 the most, followed closely W addition. The opposite trend is seen for Mn, while Co is predicated to have minimal effect.

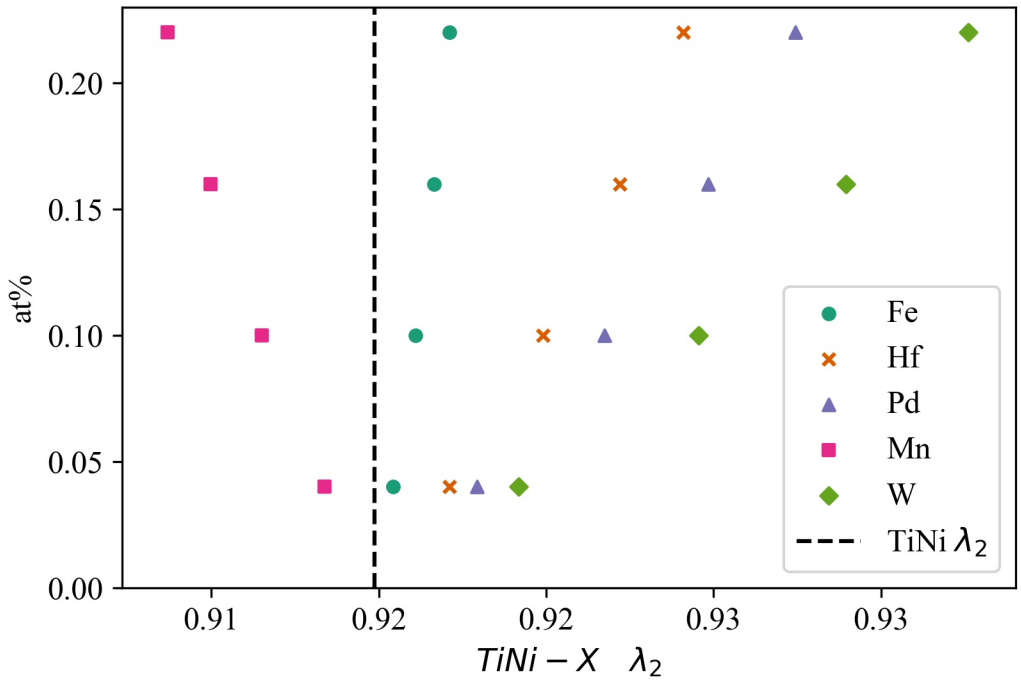

Figure 3.12: Predicted trends for λ_2 in ternary $TiNi_{(1-c)}X_c$ as a function of concentration

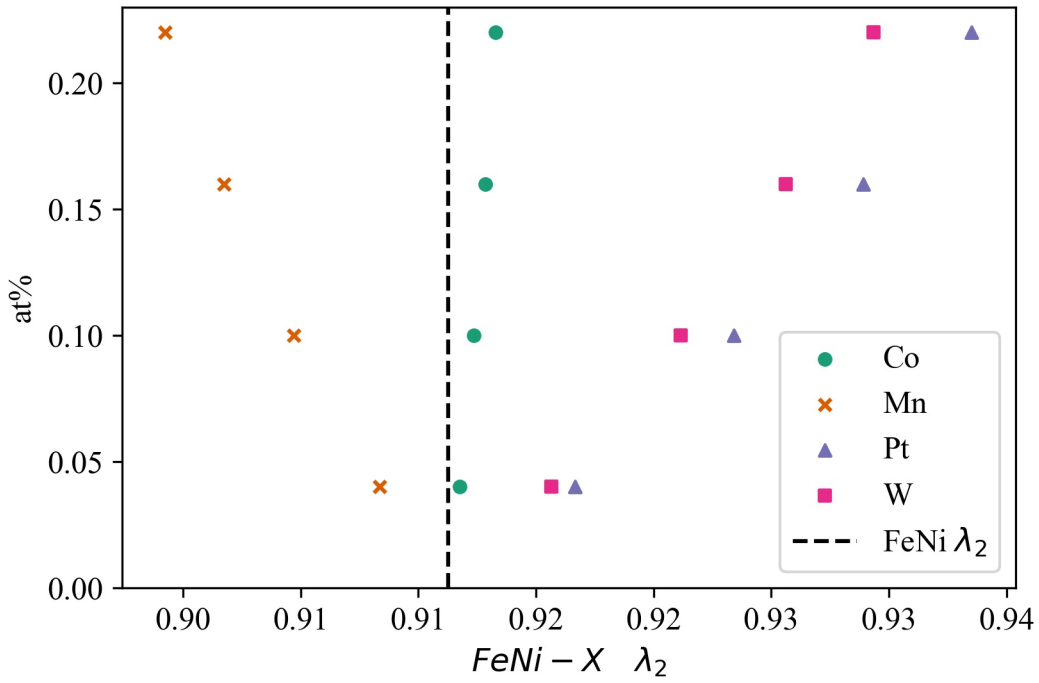

Figure 3.13: Predicted trends for λ_2 in ternary $FeNi_{(1-c)}X_c$ as a function of concentration

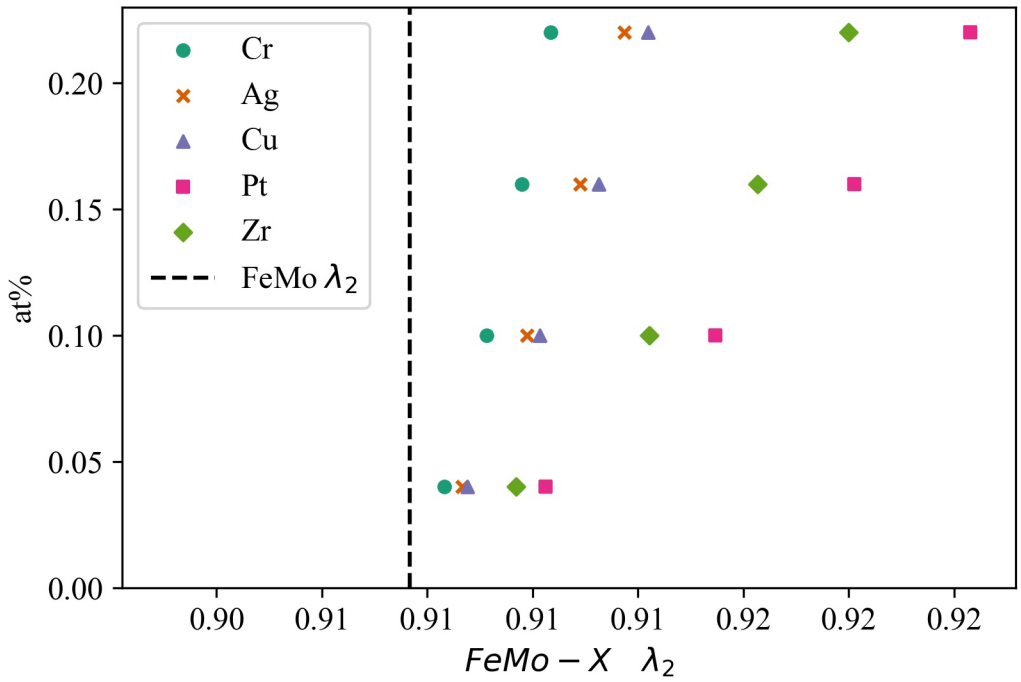

Figure 3.14: Predicted trends for λ_2 in ternary $FeMo_{(1-c)}X_c$ as a function of concentration

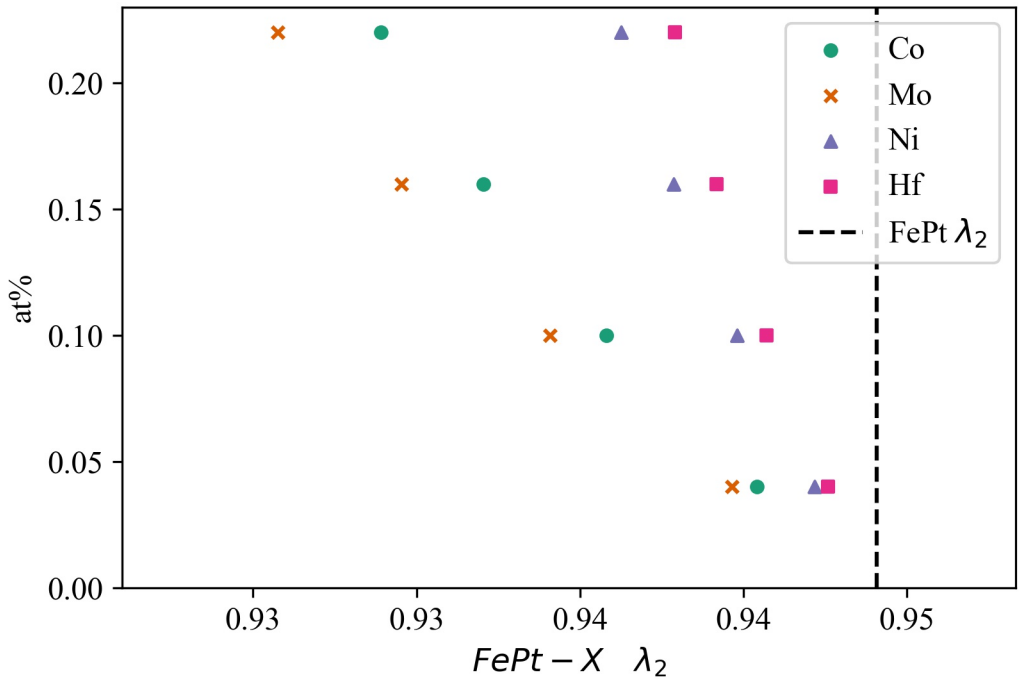

Figure 3.15: Predicted trends for λ_2 in ternary $FePt_{(1-c)}X_c$ as a function of concentration

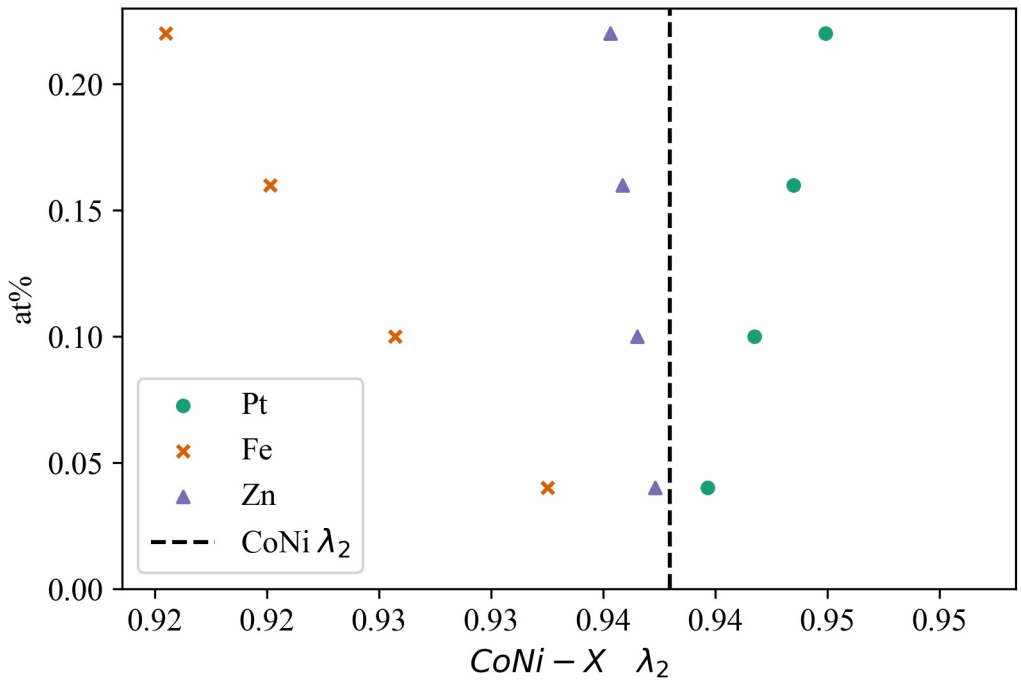

Figure 3.16: Predicted trends for λ_2 in ternary $CoNi_{(1-c)}X_c$ as a function of concentration

Table 3.3: Prediction of λ_2 values for FeNi-X

	at%	Co (λ_2)	Mn (λ_2)	Pt (λ_2)	W (λ_2)
0	0.040	0.912	0.908	0.917	0.916
1	0.100	0.912	0.905	0.923	0.921
2	0.160	0.913	0.902	0.929	0.926
3	0.220	0.913	0.899	0.934	0.929

Table 3.4: Prediction of λ_2 values for FeMo-X

at%	Cr (λ_2)	Ag (λ_2)	Cu (λ_2)	Pt (λ_2)	Zr (λ_2)
0.040	0.910	0.911	0.911	0.913	0.912
0.100	0.911	0.912	0.913	0.917	0.915
0.160	0.912	0.914	0.914	0.920	0.918
0.220	0.913	0.915	0.915	0.923	0.920

Table 3.5: Prediction of λ_2 values for CoNi-X

at%	Pt (λ_2)	Fe (λ_2)	Zn (λ_2)
0.040	0.940	0.933	0.937
0.100	0.942	0.926	0.937
0.160	0.943	0.920	0.936
0.220	0.945	0.915	0.935

Table 3.6: Similarity of systems based on the Discrete Frechet distance between minimum energy pathways

	PtNi	FeCo	ZnNi	WNi	HfZn	WTi	ZrMo	WCr	PtFe	CrTi
PtNi	0.000	0.923	0.408	0.669	0.598	0.422	0.569	0.660	0.398	0.729
FeCo	0.923	0.000	0.915	0.738	0.954	0.574	0.820	0.910	0.886	0.852
ZnNi	0.408	0.915	0.000	0.801	0.239	0.414	0.473	0.393	0.711	0.869
WNi	0.669	0.738	0.801	0.000	0.757	0.718	0.755	0.849	0.780	0.986
HfZn	0.598	0.954	0.239	0.757	0.000	0.481	0.431	0.280	0.905	0.990
WTi	0.422	0.574	0.414	0.718	0.481	0.000	0.337	0.421	0.593	0.999
ZrMo	0.569	0.820	0.473	0.755	0.431	0.337	0.000	0.321	0.851	0.997
WCr	0.660	0.910	0.393	0.849	0.280	0.421	0.321	0.000	0.932	1.008
PtFe	0.398	0.886	0.711	0.780	0.905	0.593	0.851	0.932	0.000	0.729
CrTi	0.729	0.852	0.869	0.986	0.990	0.999	0.997	1.008	0.729	0.000

Table 3.7: Similarity of systems based on the Discrete Frechet distance between minimum energy pathways

	CrTi	ZnCr	HfMn	CrMo	MnNi	CuMo	PtMo	WFe	MnZn	HfCo
CrTi	0.00	0.99	0.99	0.84	0.99	0.57	0.96	0.99	0.96	1.01
ZnCr	0.99	0.00	1.22	1.00	1.14	0.86	0.87	1.20	1.20	0.72
HfMn	0.99	1.22	0.00	0.29	0.43	1.07	1.51	0.35	0.43	1.09
CrMo	0.84	1.00	0.29	0.00	0.39	0.82	1.32	0.32	0.37	0.88
MnNi	0.99	1.14	0.43	0.39	0.00	0.97	1.40	0.25	0.21	0.99
CuMo	0.57	0.86	1.07	0.82	0.97	0.00	0.96	1.04	1.02	0.90
PtMo	0.96	0.87	1.51	1.32	1.40	0.96	0.00	1.49	1.43	1.18
WFe	0.99	1.20	0.35	0.32	0.25	1.04	1.49	0.00	0.24	1.06
MnZn	0.96	1.20	0.43	0.37	0.21	1.02	1.43	0.24	0.00	1.05
HfCo	1.01	0.72	1.09	0.88	0.99	0.90	1.18	1.06	1.05	0.00

Table 3.8: Similarity of systems based on the Discrete Frechet distance between minimum energy pathways

	HfCo	FeZr	PtCo	FeTi	HfW	ZnCo	WZr	AgMo	HfFe	FeCu
HfCo	0.00	1.04	0.80	1.02	1.02	0.92	1.07	0.80	1.08	0.75
FeZr	1.04	0.00	0.74	0.89	1.03	1.13	0.65	0.65	0.97	0.70
PtCo	0.80	0.74	0.00	0.78	0.69	1.07	0.58	0.30	0.69	0.26
FeTi	1.02	0.89	0.78	0.00	0.18	1.09	1.01	0.90	0.18	0.60
HfW	1.02	1.03	0.69	0.18	0.00	1.10	1.00	0.78	0.23	0.44
ZnCo	0.92	1.13	1.07	1.09	1.10	0.00	1.12	0.97	1.14	0.90
WZr	1.07	0.65	0.58	1.01	1.00	1.12	0.00	0.37	1.05	0.74
AgMo	0.80	0.65	0.30	0.90	0.78	0.97	0.37	0.00	0.84	0.41
HfFe	1.08	0.97	0.69	0.18	0.23	1.14	1.05	0.84	0.00	0.56
FeCu	0.75	0.70	0.26	0.60	0.44	0.90	0.74	0.41	0.56	0.00

Table 3.9: Similarity of systems based on the discrete frechet distance between minimum energy pathways

	FeCu	PtHf	MnTi	NiCo	FeAg	FeCr	NiFe	MnFe	FeMo
FeCu	0.00	0.63	0.40	0.38	0.65	0.53	0.49	0.89	0.50
PtHf	0.63	0.00	0.94	0.58	0.64	0.39	0.60	1.13	0.61
MnTi	0.40	0.94	0.00	0.68	0.81	0.91	0.88	0.96	0.74
NiCo	0.38	0.58	0.68	0.00	0.65	0.28	0.36	0.92	0.32
FeAg	0.65	0.64	0.81	0.65	0.00	0.65	0.65	0.87	0.65
FeCr	0.53	0.39	0.91	0.28	0.65	0.00	0.34	1.05	0.37
NiFe	0.49	0.60	0.88	0.36	0.65	0.34	0.00	1.01	0.40
MnFe	0.89	1.13	0.96	0.92	0.87	1.05	1.01	0.00	0.97
FeMo	0.50	0.61	0.74	0.32	0.65	0.37	0.40	0.97	0.00

3.2.3 Discussion

The B2 $\rightarrow$ Cm transition of CuZr was used as a model for all transformations. Several factors influenced the decision for this approach; Most SMAs found in literature have a cubic (B2) parent phase. The reason for this is well explained in [35] on the topic of self-accommodation. Conditions of perfect self-accommodation between martensite and cubic phases only requires that volume is preserved in the transformation. Another benefit of volume preservation as a condition of compatibility is that modification of lattice parameters is simplified to finding alloying elements that reduce a change in volume of transformation. Therefore, each alloy in the database is deformed along four dimensions starting from B2 as the parent structure and taken to Cm martensite. Volume is allowed to relax for both B2 and Cm structures.

To gain further understanding of the landscape of binary alloys sampled, a similarity metric based on the Discrete Fretchet distance between two curves was employed to allow comparison of different unrelated systems. This measure was performed using the curves of minimum energy pathways (MEPs) along a parametrized four dimensional space. The parametrization is discussed in detail in the methods section of this dissertation. The similarity distances given between any two structures can be found in tables 3.6-3.7. The similarity distance of any system to itself is zero. The curves measured by the fretchet metric are 4 dimensional curves based on the phase transformation strains from B2–>Cm structure. By measuring similarity between systems, it might be possible to expedite the discovery process through identification of related SMA behaviour across the composition space.

3.2.4 Conclusion

The quality of SMA function for fast switching applications depends on the accesibility of low energy pathways to the transformation. The performance of SMAs is closely tied to the energetics of transformation. Certain characterisitc elements within the energy landscapes are expected to reflect useful information about systems accross the intermetalics. The energetic barriers, λ_2 =1 condition, and similarity metrics that are discussed in this work can provide guidance for the future

selection of systems across the full spectrum of candidate HTSMAs. We showed good agreement with experimental results on model SMA system, NiTi.

4. SITE SYMMETRY ANALYSIS OF RELAXATION PATHWAYS IN BORON DOPED VO2

4.1 Introduction

Since the design of the early physical memristor by HP, first theoretically posed by Leon Chua in 1971, memristive functional materials have become ubiquitous within neuromorphic computing architectures due to their ability to hold a passive resistive state and simultaneously serve as programmable memory in logic circuits, eliminating the need for a data transfer bus. For phase change memory (PCM) devices, the asymmetric response of the material property across the transition complicates their use in designs implementing the spike-timing-dependent plasticity (STDP) [41**?**]. This temporal dependent response of neuron plasticity can be emulated by memristors that modulate conductivity based on diffusive dynamics [42]. Tunable time-dependent modulation of conductivity could serve to emulate both the short-term and long-term plasticity and greatly reduce complexity of neuromorphic hardware design. The ability to control the work function of charge carriers in electronically correlated materials is tantamount to programming a synaptic element for neuromorphic function. Recently, Sellers et. al [43], demonstrated that introducing a mobile dopant into the VO_2 lattice can have a profound energetic consequence that is wholly separate from nucleation mechanics. Calorimetry analysis shows temporal evolution of the heating transition temperature going from $M_1 \rightarrow R$ caused by diffusion of B atoms relaxing from non-equilibrium conditions in the monoclinic VO_2 lattice. The authors demonstrated a maximum temperature modulation range spanning 45°C (for a $B_{0.05}VO_2$ sample) that is kinetically controlled by the energetic barriers of boron diffusion from metastable to stable states. In this work, we aim to resolve the dynamics of boron diffusion within the scope of a complex energy landscape that changes upon the reversible structural transition that VO_2 goes through. We propose a method to relate interstitial boron sites between R and M_1 structures by taking into account the theoretical point orbital splits. We further apply this analysis to resolve a plausible mechanism in boron doped VO_2 that corroborates experimental evidence of a thermal and time-dependent hysteresis.

Vanadium dioxide is a well studied material featuring a wide gamut of structural and electronic properties that modulate near room temperature (Tc = 340 K). The VO_2 structural transition is coupled to an electronic transition responsible for a large change in resistivity as well as a shift in wavelength transmittance. At temperatures above Tc, VO_2 behaves like a metal and forms a tetragonal structure with space group P42/mnm. The vanadium atoms form a chain parallel to the c axis (c_R) with an equal V-V distance of 2.85 [44]. Cooling below T_c induces a symmetry reduction to monoclinic space group P21/c and concomitant metal to insulator transition (MIT). The M_1 phase is characterized by dimerization of the vanadium atoms in a twisted configuration relative to c_R with the V-V distance alternating between 2.65 and 3.12 [45]. It has been stipulated that large multivalent dopants alter T_c by either the charge doping effect or by structurally destabilizing the M_1 V-V dimers while defect mediated nucleation offers an extra degree of freedom for tuning T_c and hysteresis width. For example, experiments on unclamped VO_2 nanobeams [46] show that point defects generally reduce the nucleation barrier equally for both rutile (R) and monoclinic (M_1) phases and therefore reduce hysteresis, but R formation exclusively benefits from a regenerative mechanism at M_1 twins under strain and thus hysteresis reduction is more pronounced in the reverse transition.

There are antithetical aspects in engineering the hysteresis of phase change materials for memristive application. Even though, reducing hysteresis by tuning the lattice parameters [47] can increase the amount of useable cycles as well as reduce the width under which asymmetry can be expressed; Reducing hysteresis increases volatility and negatively impacts storage longevity. Reduction of Tc and the VO_2 response time are essential in switching applications such as energy smart windows, optical filters, and low-power mott transistors, while granular property modulation is desirable for phase change memory devices and neuromorphic computing technology. Progress in capitalizing on the electronic transport properties of VO_2 has been stifled by an incomplete understanding of the mechanism governing the Mott/Pierls dynamics [48; 49; 50]. Establishing a one-to-one atomic correspondence between doped R and M_1 structures gives a relational map to investigate the consequences that symmetry breaking has on the energy pathways of boron migra-

tion across the forward or reverse transition. We will show possible energetic pathways that could help in understanding kinetic asymmetries between boron relaxation in R and M_1.

4.2 Experimental

4.2.1 Synthesis of VO2 Nanowires

VO_2 nanowires with diameters of approximately 210±70 nm and lengths of 4.0±3.0 m were prepared as reported in our previous work based on the hydrothermal reduction of V_2O_5 by 2-propanol. Briefly, 1.6000 g of V_2O_5 (Sigma-Aldrich, St. Louis, MO) was reduced to VO_2 with 10 mL of 2-propanol (Fisher, Fair Lawn, NJ) dissolved in 65 mL of deionized water (prepared with a Barnstead International NANOpure Diamond ultrapure water system = 18.2 M cm-1). The hydrothermal reaction was performed at 210°C for 72 h in a 125 mL autoclave. The supernatant was discarded and the precipitate was rinsed with acetone (Macron Fine Chemicals, Center Valley, PA). The samples were then annealed within a quartz tube to a temperature of 550°C (ramping at a rate of ca. 45°C/min) for 3 h under flowing argon gas at a rate of 800 mL/min.

4.2.2 Incorporation of B by Diffusive Doping

2-Allyl-4,4,5,5-tetramethyl-1,3,2-dioxaborolane (97%) was purchased from Sigma-Aldrich (St. Louis, MO). In a typical reaction, 20 mg of VO_2 nanowires were dispersed in 1.00 mL of mesitylene by ultrasonication and 200 L of 2-allyl-4,4,5,5-tetramethyl-1,3,2-dioxaborolane was added to the reaction mixture. The reactants were stirred for 2.5 h at 120°C under an argon environment in a Schlenk flask. Centrifugation was then used to recover the VO_2 nanowires, followed by rinsing with toluene and further annealing using a 2 mL porcelain combustion boat (VWR, Sugar Land, TX) to a temperature of 900—950°C for 1 minute, again under an argon environment, in a quartz tube furnace as reported in our previous work [51].

4.2.3 Powder X-ray Diffraction (XRD)

In order to characterize the degree of phase purity of the sample, powder X-ray diffraction (XRD) patterns were obtained using a Bruker D8-Focus Bragg-Brentano X-ray powder diffractometer equipped with a Cu K (= 1.5418Å) source and operated at an accelerating voltage of 40

kV.

4.2.4 Synthesis, Characterization, and Relaxation of B0.02VO2

Furthermore, differential scanning calorimetry (DSC) analysis was performed using a TA instruments Q2000 calorimeter. The samples were placed in an aluminum T-zero pan under a purge flow of argon gas. To characterize the dynamic response of the samples, scans from -30°C to 100°C and back to -30°C with a scan rate of 10°C/min were used.

4.3 Computation

4.3.1 Transformation Matrices

Although the conventional unit cells of M_1 and R are different shapes, it is possible to transform the R lattice into a monoclinic basis without reduction of symmetry, i.e. an isometry mapping of R. The change of basis enables correspondence between atomic positions in R with those in M_1 under the same frame of reference. The relationship between R and M_1 lattice parameters, derived from X-ray diffraction experiments in literature, is given as:

$$\boldsymbol{a_{M1}} = 2\boldsymbol{c_R}, \qquad \boldsymbol{b_{M1}} = \boldsymbol{a_R}, \qquad \boldsymbol{c_{M1}} = \boldsymbol{b_R} - \boldsymbol{c_R} \tag{4.1}$$

The c-axis is doubled in R parallel to the M_1 a-axis. Although, this relationship does give an atomic correspondence between R and M_1, the M_1 unit cell prevalent in the literature is not a derivative of modern cell reduction methods. Pioneering work on reduced cell forms by Mighell et al. [52] allows derivation of uniquely defined conventional lattices based on a mathematical foundation. This standard removes ambiguity when communicating crystallographic information. For our analysis we choose to transform the M_1 unit cell in accordance with modern standards, where the lattice vector translations in the a-c plane are minimized, β angle is obtuse, and $|a| < |c|$ is enforced. The M_1 lattice is transformed to a modern standard setting by,

$$\begin{pmatrix} \boldsymbol{a'_{M1}} \\ \boldsymbol{b'_{M1}} \\ \boldsymbol{c'_{M1}} \end{pmatrix}^T = \begin{pmatrix} \boldsymbol{a_{M1}} & \boldsymbol{b_{M1}} & \boldsymbol{c_{M1}} \end{pmatrix} \begin{pmatrix} -1 & 0 & 0 \\ 0 & -1 & 0 \\ -1 & 0 & 1 \end{pmatrix} \tag{4.2}$$

and atomic positions by

$$\begin{pmatrix} x'_m \\ y'_m \\ z'_m \\ 1 \end{pmatrix} = \begin{pmatrix} -1 & 0 & 0 & 0 \\ 0 & -1 & 0 & 0 \\ -1 & 0 & 1 & -0.5 \\ 0 & 0 & 0 & 1 \end{pmatrix} \begin{pmatrix} x_m \\ y_m \\ z_m \\ 1 \end{pmatrix} \tag{4.3}$$

The transformed lattice parameters for M_1 as calculated by DFT are:

$$abc() = 5.390345, 4.586349, 5.396233 \quad \alpha\beta\gamma = 90, 116.4, 90 \tag{4.4}$$

Caution must be taken when manipulating the change of basis of group-subgroup related crystal structures as there are severe consequences to an improper basis transformation, such as mapping atomic positions to the wrong site symmetry, or changing the inter-atomic distances without necessarily changing the space group. One consequence of changing the basis of M_1 to our new conventional cell is that the lattice correspondence commonly found in the literature is no longer valid. Fortunately, there are well established group theoretical methods and freely available software tools to help find an appropriate change of basis [28].

4.3.2 DFT

Total energies per unit cell were calculated based on Density Functional Theory (DFT) as implemented in the Vienna Ab-initio Simulation Package (VASP). The Generalized Gradient Approximation (GGA) under the Perdew-Burke-Ernzerhof [17] (PBE) formalism was used for the exchange correlation. Pseudopotentials were generated by the projector augmented-wave (PAW) method and a cut-off energy of 533 eV was set for the plane wave basis. Optimized structure ge-

ometries converged as changes in total energy between steps were within 10^{-6} eV and ionic forces less than 10^{-4} eV/ . Integration of the Brillouin zone was performed with a mesh density of at least 3000 k-points per atom. 96-atom supercells were relaxed for calculation of the most stable sites for boron interstitial insertion while 12-atom cells were used to search for stable sites as well as for the investigation of migration paths. To account for correlation effects of the electron localization of vanadium d orbitals, a GGA + U method [53] was employed by setting the effective U parameter to 3.4 eV. The solid-state nudged elastic band (SSNEB) method [54] was used to generate the minimum energy path (MEP) of boron migration in rutile and monoclinic structures. SSNEB permits interpolation of the unit cell degrees of freedom and therefore the lattice parameters were fully relaxed at the endpoint structures.

4.3.3 Interstitial Search

Interstitial sites within the R and M_1 lattice were searched using the cages algorithm developed by Curtarolo et al [55]. The method defines within a crystal structure, a collection of empty spherical cages encapsulated by any quadruplet of non-coplanar atoms. The resulting set represents possible interstitial locations where a dopant atom could be placed. The algorithm ensures a unique set of crystal structures with respect to the symmetry operations of the respective space groups. The final output was used to create prototype structures doped with a single boron atom placed at the center of the cage. In total, a set of 10 structures for R, and 58 structures for M_1 were generated.

4.3.4 Mapping Points Between Distorted Structures

In crystal structures with a group-subgroup relationship, such as the high- and low-symmetry phases in VO_2, the atomic correspondence between the phases can be represented under a linear transformation of the Wyckoff sites plus a symmetry breaking distortion. The term Wyckoff splitting as used in crystallography refers to a reduction of site symmetry that partitions the orbits (symmetry equivalent positions) of an atom in the parent group G into nonequivalent sets under a proper subgroup H. For example, in undoped VO_2, the O ion in rutile, with site symmetry 4f, splits

to two nonequivalent O ions (4e, 4e) under the M_1 basis. Similarly, for boron doped VO_2, we take the assumption that some boron sites in the R phase become symmetrically nonequivalent in M_1, i.e. undergo a Wyckoff split across the phase transition. It has been shown in the literature to be necessary to account for Wyckoff splitting of point defects in supercell simulations [56]. This is especially true when the supercell does not have the same crystal class as the primitive lattice. In this case, the reduction of point symmetry creates additional unique sites. We extend this concept and apply it to the symmetry reduction of the VO_2 transformation. It has been established previously from experiments and computation that boron in VO_2 tends to have tetragonal coordination with oxygen ions at interstitial sites in both R and M_1. However, due to the symmetry break at the phase transition and Wyckoff splitting, it is not clear whether boron remains in a ground state configuration across the transition. For a corresponding interstitial site to remain stable across the transition, it must either be located at the global energy minimum, or have a high enough energy barrier to prevent migration (relaxation).

Using the Stoke's and Hatch method [57], a transformation matrix L_{rm} defining the group-subgroup relationship is used to establish the correspondence of real space coordinates between M_1 and R crystal structures, with the caveat that placement of a boron atom into the host lattice breaks the space group symmetry. Regardless of this complication, we will show that when the lattice distortion is small, as is the case with stable boron interstitial sites, the undistorted symmetry relationships hold true and allow the approximate mapping of sites between distorted structures. As an illustrative example, let coordinates in the rutile basis be denoted by $\boldsymbol{x_R}$ and those in the monoclinic basis by $\boldsymbol{x_M}$. Then the following change of basis matrix L_{rm} converts coordinates from $\boldsymbol{x_R}$ to $\boldsymbol{x_M}$:

$$L_{rm}\boldsymbol{x_R} = \boldsymbol{x_M} \tag{4.5}$$

$$\begin{pmatrix} -1/2 & 0 & 1/2 & 1/4 \\ 0 & -1 & 0 & 0 \\ 1/2 & 0 & 1/2 & -1/4 \\ 0 & 0 & 0 & 1 \end{pmatrix} \begin{pmatrix} x_r \\ y_r \\ z_r \\ 1 \end{pmatrix}_R = \begin{pmatrix} \frac{-1}{2}x_r + \frac{1}{2}z_r + 1/4 \\ -y_r \\ \frac{1}{2}x_r + \frac{1}{2}z_r - 1/4 \end{pmatrix}_{M1} \tag{4.6}$$

The resulting vector $(-1/2x_r+1/2z_r+1/4, -y_r, 1/2x_r+1/2z_r-1/4)$ represents rutile coordinates in the monoclinic unit cell basis. The transformation of a rutile unit cell to a monoclinic basis is depicted in Figure 4.1. Now consider a boron atom placed within the monoclinic crystal lattice with coordinate $\boldsymbol{O_M}$. The goal is to find the corresponding rutile point, $\boldsymbol{x_R}$, that maps to $\boldsymbol{O_M}$. The subgroup symmetry operations $h_i \in H$ of an undistorted monoclinic cell can be used to operate on $\boldsymbol{O_M}$ and generate its idealized orbit. It is then compared to the resultant vector $\boldsymbol{x_M}$ to find the minimum distance of any pair of coordinates. If the minimum distance is close to zero, here denoted as $\min\{|h_i\boldsymbol{x}_M - h_j\boldsymbol{O}_M|\} \approx 0$, then the point $\boldsymbol{x_R}$ and $\boldsymbol{O_M}$ can be considered mapped under symmetry. The general method to map points in rutile to a point $\boldsymbol{O}_M$ is as follows:

1. Find the orbit of $\boldsymbol{x}_R$ in rutile by applying its symmetry operations:

$$G(x) = \{g_i\boldsymbol{x_R} : g_i \in G\} \tag{4.7}$$

2. Map the resulting set of coordinates to the monoclinic basis.

$$L_{rm}(\boldsymbol{x_R}) = \boldsymbol{x}_M \tag{4.8}$$

3. Complete the orbit of $\boldsymbol{x}_M$ by applying the subgroup symmetry operations.

$$H(x) = \{h_i\boldsymbol{x_M} : h_i \in H\} \tag{4.9}$$

4. Finally, find the minimum distance from the set $h_i\boldsymbol{x}_M$ to the point $\boldsymbol{O}_M$.

$$\min\{|h_i\boldsymbol{x_M} - h_j\boldsymbol{O_M}|\} \tag{4.10}$$

Note that since heterogeneous strains or symmetry-breaking distortions are not accounted for by the transformation matrix, some approximation error is inherent in mapping boron positions from rutile to the monoclinic lattice. The local distortion caused by interaction between boron and

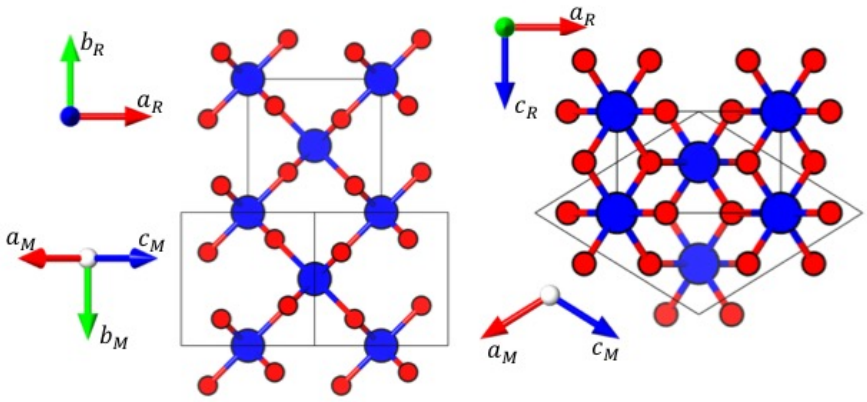

Figure 4.1: Coordinate transformation of rutile (top) to a monoclinic cell (botton)

R sites	eV/atom	Distance () from M site **S1**
R1	0.000	1.00
R2	0.103	0.21
R3	0.232	0.05 **match**
R4	2.944	1.37
R5	5.204	1.72
R6	5.287	1.15
R7	5.403	1.08
R8	5.531	0.69
R9	13.609	1.93

Table 4.1: Boron site relative formation energies in rutile and their corresponding distance from the most stable M site

oxygen is a main contributor to this error. For the most stable structures however, the distortion is not significant enough to make the mapping ambiguous. The validity of this claim will be supported in the results section under site symmetry analysis of the Wyckoff splitting.

4.4 Results and Discussion

4.4.1 Sites

B atoms have been incorporated as interstitial dopants within hydrothermally grown VO_2 nanowires using a post-synthetic diffusive doping approach.[23,24] Briefly, a 2-allyl-4,4,5,5-tetramethyl-

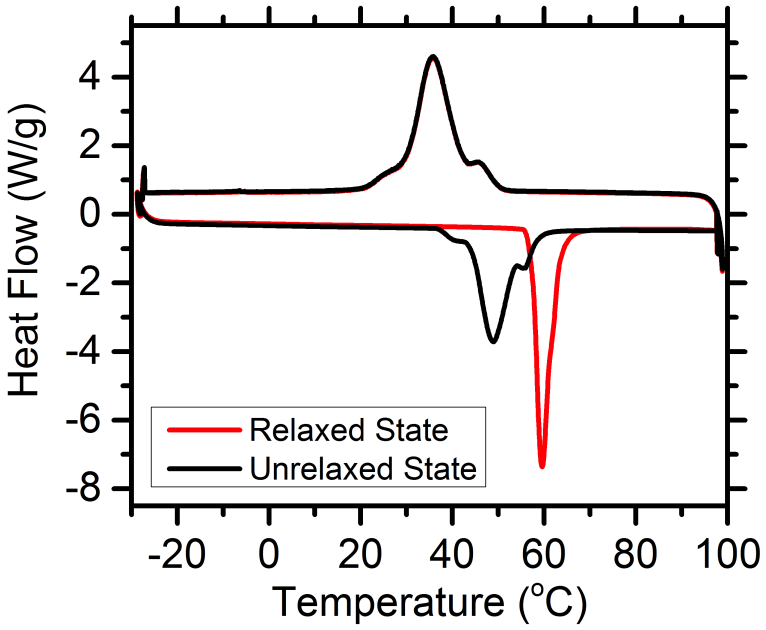

Figure 4.2: DSC traces of $B_{0.02}VO_2$ in the unrelaxed state and relaxed state. The unrelaxed state of the sample was scan immediately following temperature quenching from the R phase and the relaxed state of the sample was scanned following thermal-relaxation at room temperature for 622 days. Full thermal relaxation at room temperature for this sample was achieved within 90 days.

M1 sites	eV/atom	Distance () from **R1**
(S1, S3)	0.000, 0.031	(1.00, 0.97)
S2	0.031	0.96
trigonal S4	0.079	0.51
(S5, S6)	0.150	(0.09, 0.09) **match**
S7	0.240	0.98
(S8, S9)	0.622	(1.08, 1.08)
(S10, S11)	0.709	(1.39, 1.39)
trigonal S12	0.760	0.50
S13	0.911	1.42
S14	0.983	1.81
S15	1.059	0.73
S16	1.091	1.82
S17	1.093	1.83
S18	1.259	1.21
S19	1.820	1.86
S20	2.440	1.43
S21	3.235	2.41

Table 4.2: Boron site relative formation energies in M1 and their corresponding distance from the most stable R site

1,3,2-dioxaborolane precursor is physisorbed onto hydrothermally prepared single-crystalline VO_2 nanowires prior to a 900°C rapid thermal annealing step. The incorporation of B atoms suppresses the monoclinic $\rightarrow$ tetragonal transition temperature by ca. 10°C/at.% B.[23] Figure **??** shows DSC data for $B_{0.02}VO_2$, which has been simply allowed to relax at room temperature for 20 months, evolving from a Tc of 48.7°C for the quenched (unrelaxed) sample to a Tc of 59.6°C corresponding to the fully "relaxed" state. To investigate the asymmetry of boron relaxation on the quenched/relaxed M_1, we employed DFT calculation to generate a list of boron sites in both M_1 and R. From a total of 68 prototype structures output by the AFLOW cages algorithm, 30 were found to be symmetrically unique after relaxation, including 9 boron sites (R1-9) in the R phase, and 21 sites (S1-21) in the M_1 phase. With few exceptions, boron atoms coordinated at the center of oxygen tetrahedra. Table 4.1 makes use of equation (4.10) and lists the rutile boron sites and their minimum mapping distance to the lowest energy monoclinic site (S1). According to the

mapping procedure outlined before it is found that the most stable site in R and M_1 does not correspond symmetrically. Specifically, site R1 and S1 are at least 1.00 angstrom distance apart when considering all symmetry operations. Conversely in Table 4.2, site R1 is found to correspond to a wyckoff split of degenerate monoclinic sites, S5 and S6, which are not lowest in energy.

The formation energies of boron sites in R, and M_1 are plotted in Figure 4.4a along with site correspondence represented by a series of connected red-dashed lines. In 4.4a, starting from a ground state configuration in R, the $R \rightarrow M_1$ transition takes a boron atom into one of two possible sites, labeled S5 and S6. These sites are symmetric pairs with the same wyckoff site symmetry but are unique since they do not share the same point orbit and are 0.150 eV above S1. In relaxing from these sites down to the ground state site S1, we are careful to consider any possible intermediate sites along the shortest path. The closest neighboring sites are S4 and S12 at a distance of 0.4, and 0.5 , respectively. Interestingly, both neighbor sites have a planar trigonal (Trg) coordination and are coincidentally proximal to our predicted metastable site. Furthermore, from our list of 30 sites, these are the only trigonal sites found. To our knowledge, Trg coordination of boron in VO_2B has not been previously discussed in literature. Given the close proximity to S5, and S6, some attention will be given to these Trg interstitials as they could have significance in resolving energetic asymmetries between R and M_1 relaxation. Similarly, Figure 4.4b shows the effect of coulombic repulsion from V d states (U=3.4 eV) and a larger supercell size of 96 atoms. To reduce computational cost only the most stable relevant sites were recalculated. We find that the same stable sites do not correspond symmetrically and the energy difference increases between energy levels of boron sites in both R and M_1. This shows possible evidence that the electron correlation in VO_2 will tend to increase the relative energetic gaps between stable to metastable sites. In both cases, the flipping of energetic correspondence is surprising and suggests on the forward transformation R $\rightarrow$ M_1, the originally stable B atom is possibly shifted to a metastable site. Similarly in reverse M_1 $\rightarrow$ R, the stable M_1 site is shifted to a metastable site and therefore metastability of boron is intrinsically linked to the symmetry correspondence between R and M_1. The implications of this result is that conflicts between improving the lattice compatibility and yet maintaining non-

R sites	xyz	wyckoff	Subgroup wyckoff split	Calculated M sites
R1	(0.0, 0.5, 0.75)	4d	4e 4e	S5, S6
R3	(0.41, 0.12, 0.5)	8i	4e 4e 4e 4e	S1, S2, S8, S9

Table 4.3: Wyckoff split of most stable boron R sites to the corresponding M1 sites

volatile hysteresis response can be resolved by relinquishing parametric control of hysteresis to a diffusive element. Additionaly, we make note of possible strain dependent metastability caused by the generation of degenerate dopan sites. As can be seen in Figure 4.4cd, the formation energy of site symmetry pairs can be induced to energetically split by an arbitrarily small strain. As one site is brought to a higher energy state, the other symmetric pair is more stable to the distortion. Further, analysis is required to explore this effect and its significance in co-doping with elements that locally strain the VO_2 lattice [58; 59].

4.4.2 Wyckoff Splitting

To test the validity of this approach, an attempt to match the most stable sites found by DFT calculation to the pure VO_2 theoretical wyckoff split is summarized in Table 4.3. The most stable rutile site is located at a 4d wyckoff position and is expected to have an orbit split into two nonequivalent 4e sites. We matched a pair of monoclinic sites S5, S6 to within 0.09 angstroms of the theoretical positions. Similarly, site R3 corresponds to a four fold split into sites S1,S3,S8,and S9 and matches the theoretical orbit split of 16i to four 4e site symmetries. The results of Table 4.3 are visually represented in Figure 4.3. The close proximity between theoretical wyckoff splits and calculated sites gives confidence that our method of symmetry analysis is a valid approach. Hence, when a boron atom settles into its ground state in one phase, it will invariably find itself in a metastable configuration at the onset of a phase transition. Within this framework of analysis, the most relevant boron migration pathways are resolved.

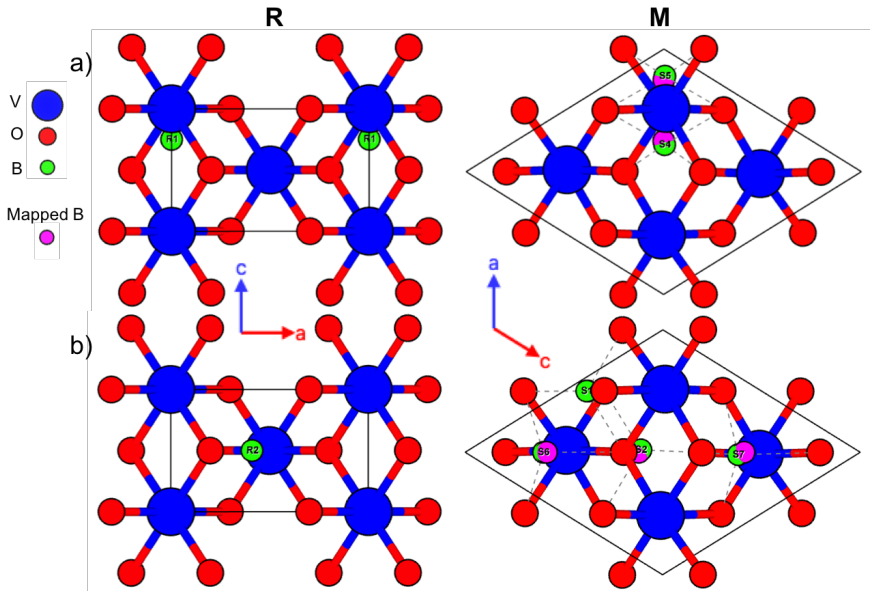

Figure 4.3: Wyckoff splitting of R sites in the M phase. a) R1 splits to two sites, S5, and S6 (show in green). The pink spheres represent the theoretical wyckoff split locations b) R2 splits into S1, S3, S8, and S9. The theoretical mapping again closely matches calculated sites (One pink sphere hidden from view by close superposition of the S1 location

4.4.3 Energy Barriers

Table 4 shows a subset of the boron relaxation pathways calculated by SSNEB. The initial relaxed image starts with a boron atom placed in site S5 since it corresponds symmetrically to the most stable R site. From there, we explored all possible migrations away from S5 towards proximal stable site locations and eliminated energetically unfavorable jumps. We found that the lowest migration energy was towards a trigonal configuration at a distance of 0.432 . Interestingly, experimental evidence has shown trigonal coordination of boron in XANES spectral data of unrelaxed M_1 [43]. In contrast, trigonal signatures completely vanish after allotting sufficient relaxation time. This was sufficient motivation to focus our analysis on the only two trigonal sites found through our site search.

Figure 4.5 shows a migration barrier of 1.8 eV from S6 to the Trg site S12. This can be

considered a high migration barrier with respect to the temperature range of the transition. Parts c,d show respectively as boron loses Tet coordination by dissociation from an oxygen atom to form a Trg coordination. We will refer to this dissociated oxygen as an apical oxygen due to having the longest bond length, 2.18 , to vanadium. In comparison, Figure 4.6 shows a lower energy barrier of 0.96 eV. A key difference here is that both apical oxygen atoms remain coordinated with boron while dissociation happens at an equatorial oxygen with a shorter bond length of 1.94 angstroms. Additionally, the apical bond length grows from 2.18 to 2.42 as boron moves to S4. Based on metastable conditions set by $R \rightarrow M_1$ or $M_1 \rightarrow R$ transitions, Figure **??** shows a comparison between possible M_1 relaxation pathways and R relaxation. Both M_1 relaxation pathways have a local minimum half-way along the reaction coordinate with structural similarity to our Trg site, S4. To check the stability of these local intermediates, the geometries were fully optimized. After relaxation, the intermediate structures were found to be identical to the stable Trg S4 site. In contrast, the migration in R from R3 to R1 does not have a local minima intermediate and instead shows a flat energy curve as it passes through Trg coordination. Although a Trg coordination is along its path, it is in effect only a transition state with no barrier. Furthermore, no evidence of a stable site with Trg coordination in R has been found through our search. SSNEB pathways show that boron migration in VO_2 changes coordination as $Tet \rightarrow Trg \rightarrow Tet$ during transition between stable in R to stable in M_1 sites.

Similar patterns of coordination change are confirmed in computational work on battery cathode materials. Rong et al. [60] has shown that ion mobility in oxide frameworks generally depends on compatibility with host structure topology rather than the host chemistry. Their work focused primarily on diffusion of multivalent (MV) ions (Mg2+, Zn2+, Ca2+, and Al3+) for design of efficient battery cathode materials. Analogous to our diffusion pathways, they show that the minima and saddle points of the MEP are bounded by coordination environment changes. Their results show correlation between improved ion mobility and a small absolute energy difference between Tet and Oct (octahedral) sites. By similar arguments we conclude that diffusion in the R phase will be easier due to both a smaller energy difference between Tet and Trg coordination and lack of an

Boron diffusion () pathways	Energy Barrier (eV)
S5 $\leftarrow$ 0.910 $\rightarrow$ S3	1.1
S5 $\leftarrow$ 0.432 $\rightarrow$ S4 $\leftarrow$ 0.509 $\rightarrow$ S3	1.0, 1.3
S5 $\leftarrow$ 0.521 $\rightarrow$ S14	1.8
S5 $\leftarrow$ 0.649 $\rightarrow$ S18 $\leftarrow$ 0.675 $\rightarrow$ S1	2.1, 1.9

Table 4.4: Boron diffusion pathways in monoclinic cell

intermediate energy barrier. Within the context of site correspondence, our results clearly indicate some major feature differences in the energy landscapes of boron migration in R and M_1, with M_1 showing a double barrier relaxation as compared to a single activated state in R.

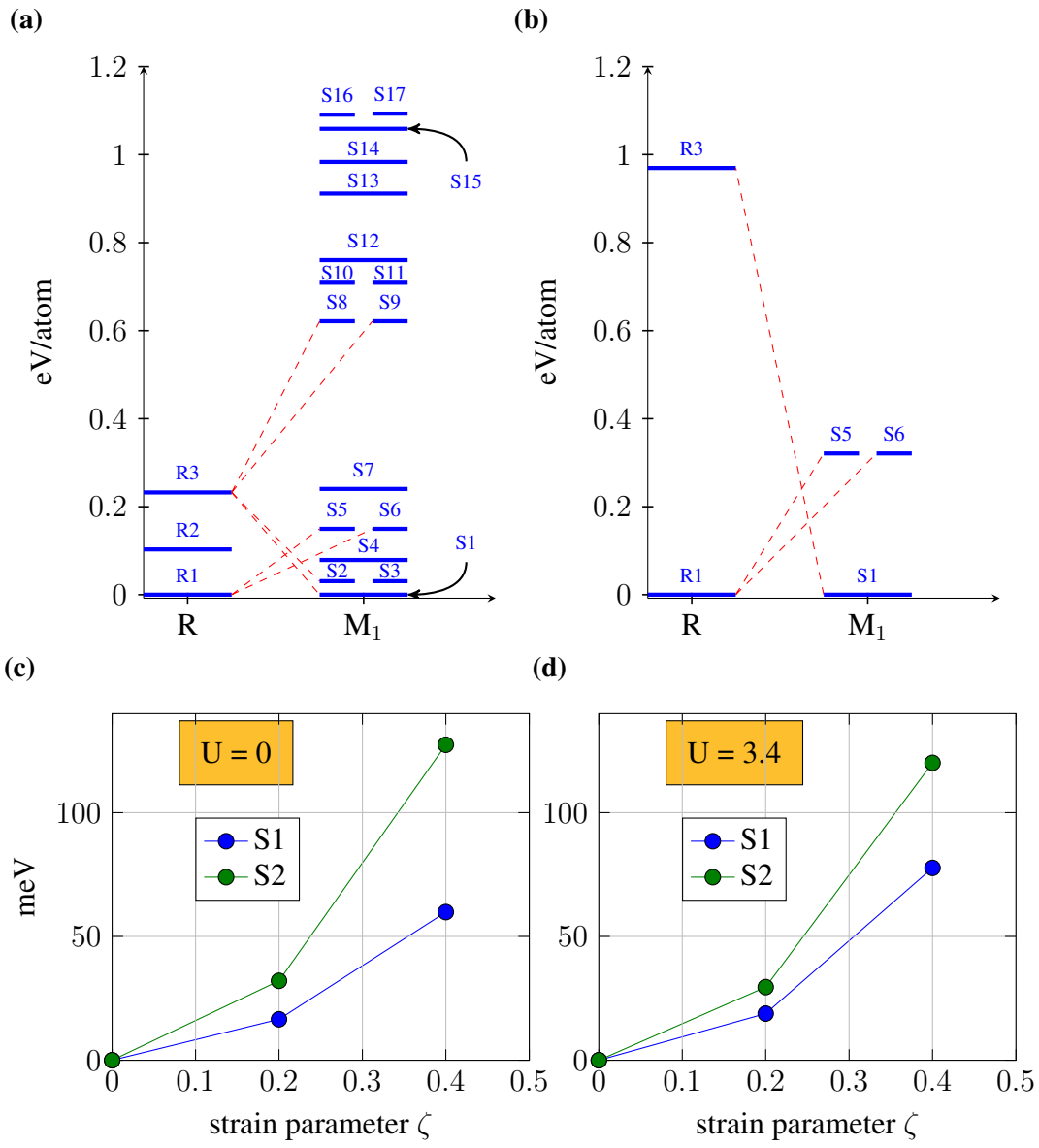

Figure 4.4: Normalized boron site formation energy levels in R and M1 with (a) cell composition $V_4O_6B_1$ and U = 0, (b) cell composition $V_{32}O_{64}B_1$ and U = 3.4. (c), (d) Strain effect on symmetrically paired sites with U = 0 and U = 3.4, respectively. The maximum strain is at 2.5% engineering strain of the a_M axis.

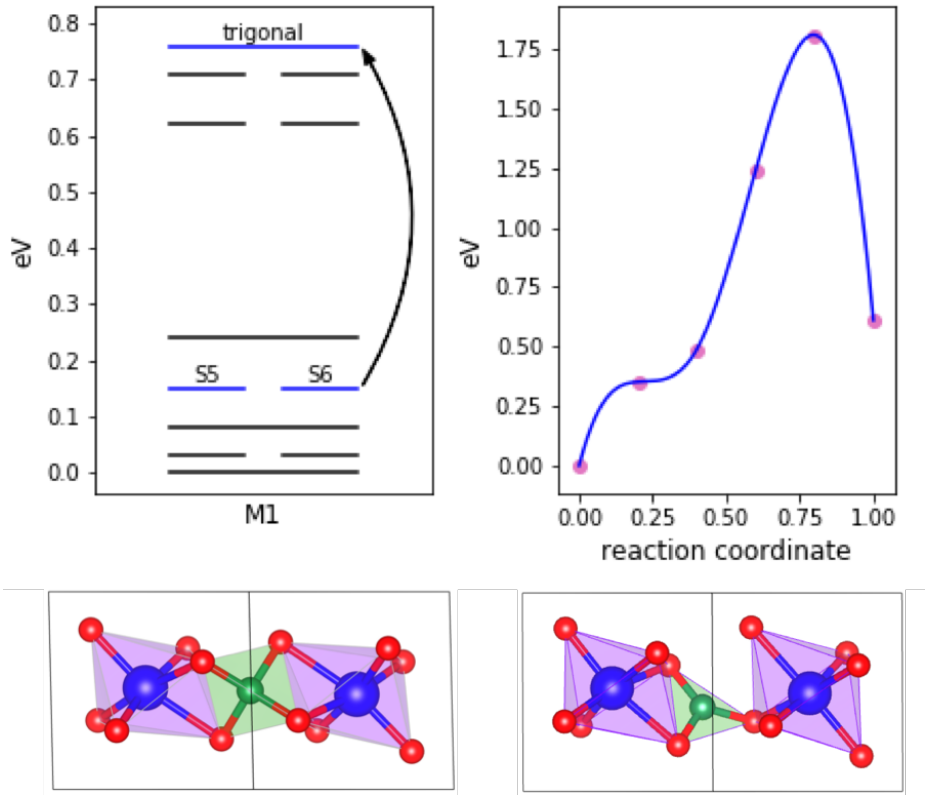

Figure 4.5: One apical oxygen bond is broken going from tetrahedral to trigonal site S10.

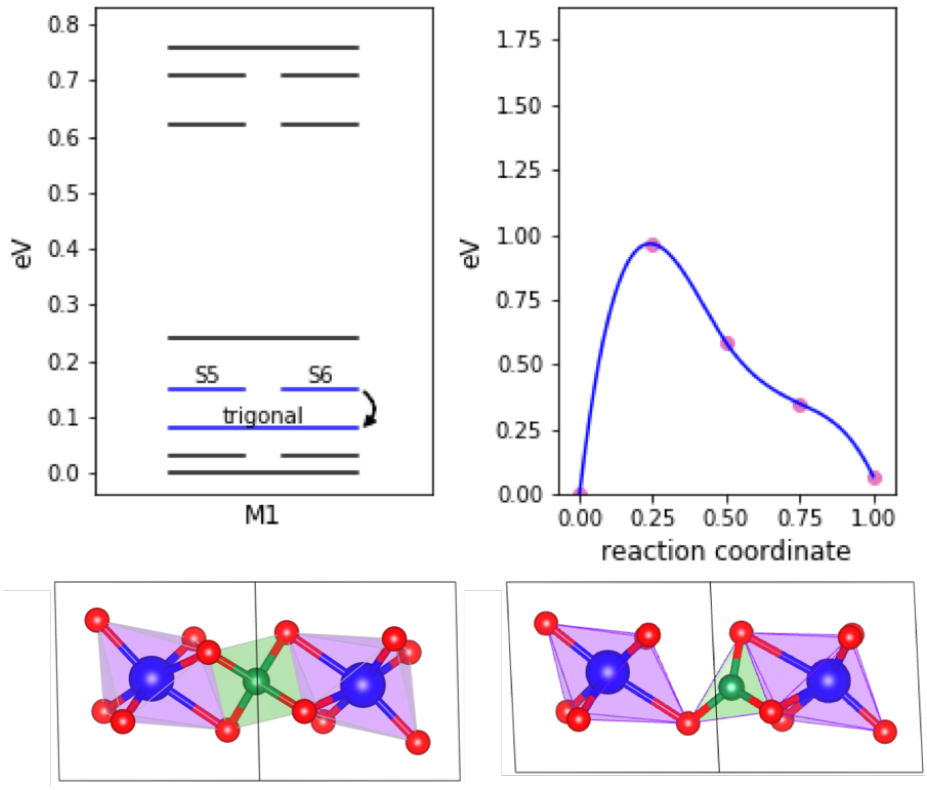

Figure 4.6: Apical long bonds are kept going from tetrahedral to trigonal site S3.

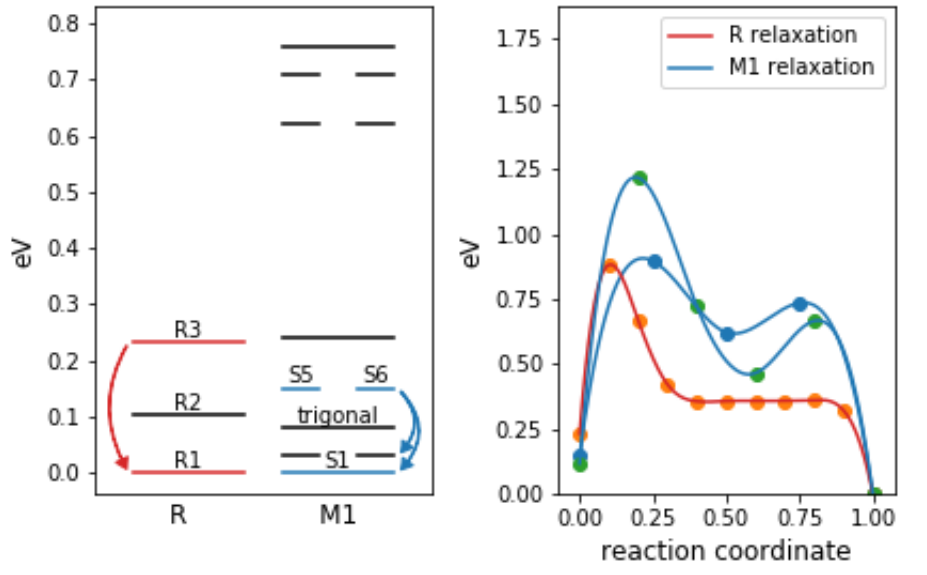

Figure 4.7: Likely relaxation pathways for R and M1 based on symmetry analysis.

4.5 Conclusion

A full symmetric and energetic analysis of the interstitial sites in VO_2 has been conducted and results indicate intrinsic boron metastability associated to the symmetry reduction. We have developed a practical and methodical approach for mapping dopant sites across distorted structures along with introducing a validation scheme based on Wyckoff split analysis, as long as the distortion from symmetry breaking and relaxation is not too large. Our site search finds two trigonal coordination sites in M_1 that have not previously been analyzed. The more stable trigonal site features an elongation of the octahedral V-O axial bonds while the less stable trigonal site coordinates with an equatorial oxygen and has less effect on octahedral bonding lengths. Differences between R and M_1 relaxation can be attributed to the slope of the energy landscape around Trg coordination. M_1 has a double barrier along the MEP with 0.7, and 0.12 eV, respectively. While R has a single lower barrier of 0.6 eV. Resolving the energetic correspondence of boron across a phase transition establishes links between two different energy landscapes, both parametrized by boron migration, one at the R phase and the other at the M_1 phase. This type of clear connection between start and end states could serve as an added guide in the design approach of doped VO_2 materials.

5. METRIC DRIVEN SEARCH FOR STRUCTURALLY STABLE INORGANIC COMPOUNDS

5.1 Synopsis

We report a prompt and facile 'metric' for the identification of structurally and dynamically (positive definite phonon structure) stable inorganic compounds. The metric considers charge-imbalance within the local substructures in crystalline compounds calculated using first-principles density-functional theory. To exemplify, we chose carbon-based nitrides as they have a large pool of structurally stable/unstable phases. We showcase how local structural information related to Wycoff symmetry uniquely identifies four new carbon-nitride phases. The metric predicts three out of four phases as structurally stable and we confirm this by direct phonon calculations. All three compounds show extraordinary mechanical properties, similar to diamond along with optimal (1.5 eV) to large (5.5 eV) bandgap. For the optimal band-gap case, we calculated the optical excitation energies using GW based Bethe-Salpeter equation. We believe that our simple, yet powerful approach will accelerate the search of unknown and unexplored inorganic compounds.

5.2 Introduction

Compounds made of light elements such as boron, carbon and nitrogen [61; 62] are known for extreme hardness, oxidation resistance and chemical inertness [63; 64; 65]. These materials find many uses in energy and sustainability applications such as visible-UV light harvesting and photocatalysis [66; 67; 68], fuel cell and electrolyzer catalyst support [69], redox catalysts [70; 71], and some other emerging areas [72; 73; 74]. Therefore, search for new materials with improved thermodynamic, electronic, and mechanical properties remain prime challenge for material science community.

Recently, carbon based light inorganic compounds have gained much momentum due to their extraordinary mechanical properties. In spite of useful physical properties [64; 65], carbon-nitrides suffer from structural and dynamical instability (unstable phonons), e.g., large pool of known

phases are stable only at externally applied pressures [75]. The development of new materials requires addressing and resolving fundamental questions concerning their chemical and structural nature in relation to their properties so that they can be designed and optimized for current and future applications. On the one hand, experiments face many challenges related to metastability, selection of precursors, determination of chemical compositions and their crystal structures, whereas calculations are limited to certain stoichiometries [76]. Both theoretical (computational) and experimental approaches face significant challenges to develop effective guidelines for the search of structurally stable phases with optimal properties.

Here, we [1] propose a metric that uses structural features that are sensitive to charge-imbalance at the local substructures—where the substructures are the building blocks of covalently bonded crystalline compounds—as a way to determine whether a given crystalline arrangement is dynamically stable. To exemplify, we chose carbon-nitride compound where C/N are arranged on tetrahedral (tet)/trigonal (trig) substructures. The metric 'M' sets the ratio for structural stability of carbon-based nitrides as

$$M = \frac{W_{tet}\,(n_2/n_1)}{W_{trig}} > 0.6, \tag{5.1}$$

for carbon rich compositions, or

$$M = \frac{W_{tet}\,(n_1/n_2)}{W_{trig}} > 0.6, \tag{5.2}$$

for nitrogen rich compositions, where W_{tet} is the average tetrahedral coordination weight of carbon, W_{trig} is the average trigonal coordination weight of nitrogen, and (n_1,n_2) are the number of carbon or nitrogen atoms in the unit cell, respectively. A strong correlation has been found between structural stability and proposed metric 'M'. Charge distribution on carbon substructures (tetrahedral (tet) or trigonal (trig)) relative to their crystallographic-points (Wycoff-positions) was calculated for several dynamically (un)stable phases of carbon-nitride polymorphs using first-principles density-functional theory (DFT). The proposed metric predicts the stability of most known carbon-

[1] Coauthor Prashant Singh performed vibrational, electronic, elastic, and optical property characterizations of new proposed structures

nitride phases with 100% accuracy. We believe that the proposed metric will allow accelerated filtering of useful inorganic compounds from large pool of possible phases, which will save computational efforts for phonon calculations of all unknown phases.

Computational method: Calculations were perfomed using first-principles density functional theory as implemented in Vienna Ab-initio Simulation Package (VASP) [77; 3]. The Perdew, Burke and Ernzerhof (PBE) generalized gradient approximation is used with a cut-off energy of 533 eV [17]. The gamma-centered Monkhorst-Pack [34] k-mesh is used for Brillouin zone integration during structural-optimization and charge self-consistency, respectively. The structural files for the known systems are taken from materials project database [2]. Structures are relaxed with higher convergence of total energies and forces, i.e., 10-6 eV/cell for energies and -10-6 eV/Å for forces. Density-functional perturbation theory (DFPT) [78; 79] with displacement method with step size 0.02 is performed to construct force constants [80] for phonon dispersion along the high-symmetry directions of the Brillouin zone [81].

5.3 Discussion

In spite of great future prospect of wide bandgap semiconductors, no design criteria have been presented for semiconductor materials. Most predictions are based on expensive DFT calculations, which makes it difficult to quickly assess the stability of candidate phases, particularly when trying to screen for potential dynamic instabilities. We developed a metric based on local coordination as a surrogate model of charge imbalance and exemplified our approach on carbon-based nitrides [82; 83; 84; 85; 86]. The C/N coordination weights have been extracted from the existing materials-project database, which has been largely ignored in theoretical predictions and marks a clear gap in the material search space. Rather than relying on random crystal prototyping, we opted to seed our search by altering the composition of the beta C3N4 structure by carbon substitution. In this way, we could compare change in stability of new phase and attribute them directly to changes in crystal symmetry with emphasis on identifying stabile substructures within the modified crystal structure.

The materials project database currently indexes 43 bulk carbon-based nitride phases predicted

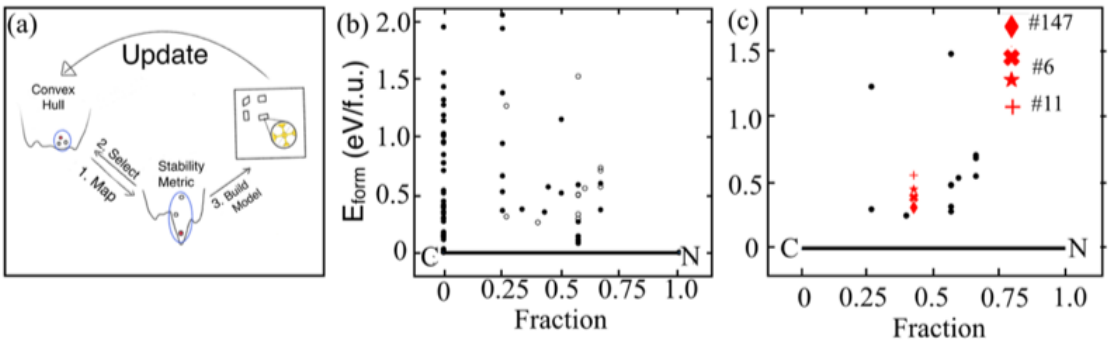

Figure 5.1: (a) Schematic of the flowchart for selecting new matric. (b) Convex hull for carbon-nitride polymorphs extracted from materials-project database. The open circles represent the phases used by the model to test the metric (also shown in Table 5.1). (c) Four new phases (sg-6(1), sg-6(2), sg-11, sg-147) predicted by the proposed metric. Formation energies in (b) and (c) are calculated using gas phase corrected energies for N2, which is taken from materials project database [2].

from DFT. The C-N in those compounds/phases can broadly be arranged in three major categories – (a) 3-dimensional (3D) networked (20), (b) layered (13), and (c) chain (10) with average formation energies of 0.906, 0.453 and 2.428 (eV/atom), respectively, above the convex hull. We found a general trend in Fig. 5.1 for C3N4 polymorphs closest to the convex hull that resist 3D C-N network formation. The C3N4 polymorphs near the convex hull are composed of layered atomic sheets with densities below 2.5 gm/cc. Therefore, these structures were eliminated from consideration, along with one dimensional structure, as possible prototype precursors in the search for stable networked carbon-nitride phases.

As mentioned above, we predict the structural stability of inorganic compounds using a simplified metric based on charge gain/loss due to bonding on atomic substructures formed by constituent elements in inorganic compounds. The metric in carbon-nitrides, as shown in Table 5.1, is defined by the average coordination ratio on tetrahedral and trigonal substructures as defined in equations (5.1) and (5.2) with a normalization factor adjusted for element dominant compositions. Regardless of formulaic simplicity, the good predictive performance of the metric stems from a couple of key physical observations. First, bond angle distortions are easily retained throughout the structure

and therefore shift the average coordination weights away from the preferred valence interaction geometry due to the formation of strong covalent networks. Second, maximal bond angle distortions are found to either originate or aggregate at symmetry points with lower degrees of freedom and become detectable by Bader analysis as slight charge imbalances. Lastly, the compounding effect of these local distortions seem to destabilize the material beyond the harmonic phonon approximation regime.

Table 5.1: The proposed metric (M) for structural stability based on charge-ratio. Here, M is the ratio of charges in tetrahedron (tet) vs trigonal (tri) arrangement of C and N in carbon-nitride polymorphs.

	C-N		Stability metric	Structural- Stability	
#	Polymorphs	Space group	[M > 0.6]	Predicted	Calculated
1	CN_2	119	0.751	Yes	Yes
2	$(CN_2)_2$	36	0.623	Yes	Yes
3	$(CN_2)_4$	122	0.611	Yes	Yes
4	C_3N	225	divergent	No (unstable)	No
5	C_3N_4	215	2.467	Yes	Yes
6	$(C_3N_4)_2$	159	0.957	Yes	Yes
7	$(C_3N_4)_2$	176	0.878	Yes	Stable at 275 GPa
8	$(C_3N_4)_2$	227	divergent	No (unstable)	No
9	$(C_3N_4)_2$	220	1.109	Yes	Yes
10	$C_{11}N_4$	16	0.597	No	No
11	$C_{11}N_4$	111	0.931	Yes	Yes
12	$(C_3N_2)_4$	221	0.594	No	No
13	$(C_4N_3)_4$	8	0.271	No	No
14	$(C_4N_3)_4$	10	0.368	No	No
15	$(C_4N_3)_4$	8	0.495	No	No

We list the net atomic charge at neighboring C-N in carbon-nitride polymorphs from Bader analysis at Wycoff symmetry point for C-N polymorphs in Table 5.1. We employed matminer's site featurizer to extract coordination character as well as weights for C-N polymorphs for the available structures in materials project database [21]. To verify the accuracy of our metric for the prediction of structural stability and find out the ground truth of our structural analysis, , in Fig.

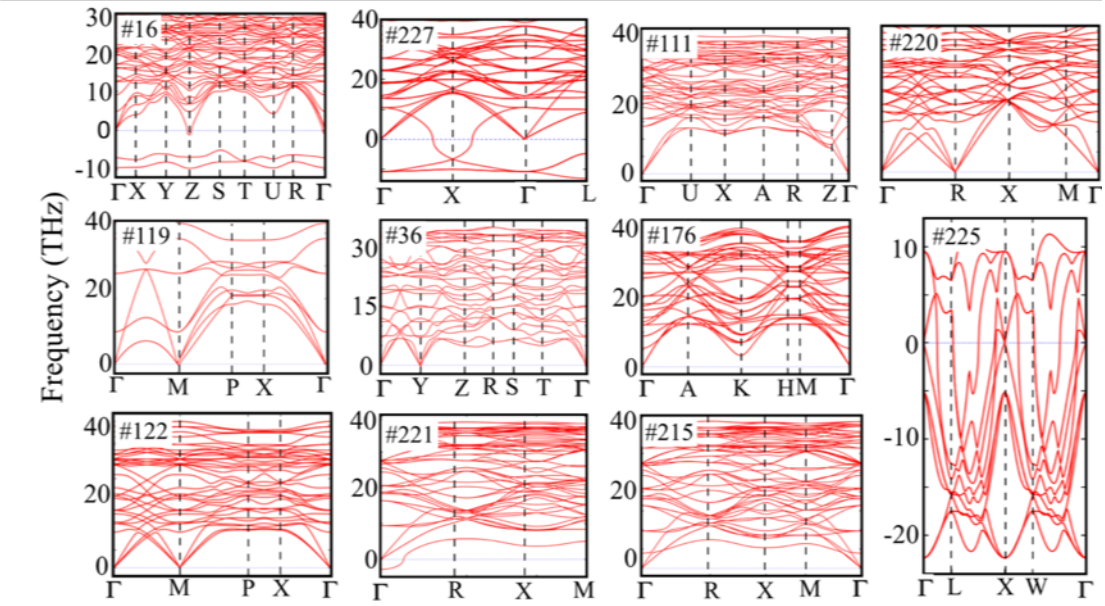

Figure 5.2: DFT calculated phonons showing stability for carbon-nitride polymorphs as predicted using proposed metric in Table 5.1.

5.2, we plot DFT calculated phonons at zero pressure for C-N cases in Table 5.1. The metric M for sg-227, sg-11, sg-211, sg-215, and sg-225 does not satisfy the criteria for structural stability, which is reflected by unstable phonons for respective cases in Fig. 5.2.

We choose $C_{11}N_4$ as an example to discuss the relevance of the proposed metric. Metric 'M' predicts that $C_{11}N_4$ with space group sg-6 is structurally unstable, while sg-111 is dynamically stable. C/N in $C_{11}N_4$ polymorphs show both tetrahedron and trigonal bonding environment. Carbon in sg-16 as shown in Fig. 5.3a is positioned at the special symmetry point (0,0,0) with positive charge of +0.21e-, whereas a special attention should be given to carbon located at the special Wyckoff positions with lowest symmetry in Fig. 5.3b, i.e., (0, 0, 0) and $(1/2, 1/2, 0)$. The C (0, 0, 0) and C $(1/2, 1/2, 0)$ in sg-111 has 0.05- and 0.02+, respectively, very close to neutral charges. For sg-16 in Fig. 5.3a C (0, 0, 0) is a fixed symmetry point and C no longer can shift positions to accommodate extra strain in bond-angles due to exccess charges. Therefore, the Bader charge imbalance coincides with maximal distortion of the ideal tetrahedral coordination. This is evidenced

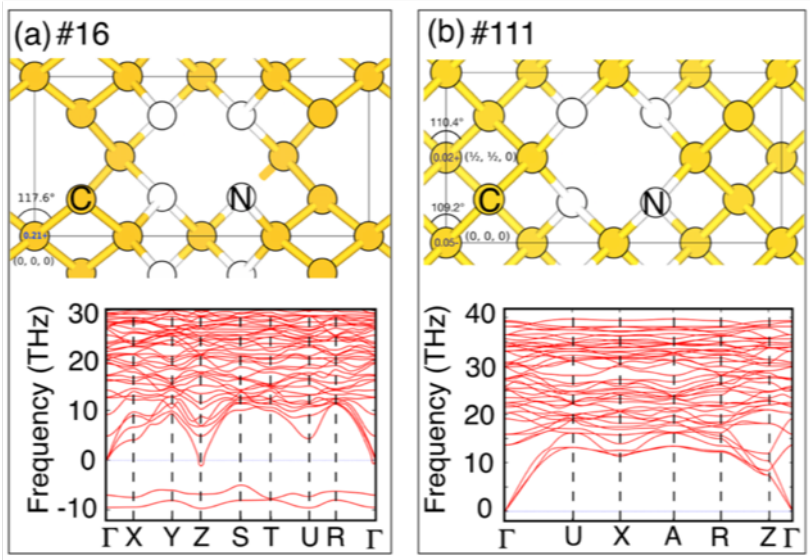

Figure 5.3: We plot crystal structure and phonon dispersion for (a) sg-16, and (b) sg-111 C11N4 polymorphs, respectively.

in Table 5.1 by our proposed stability metric (M). The tetrahedral weight feature of C (0, 0, 0) has the lowest value (0.276). This is a crucial point of observation as it directly evidences a possible correlation between ideal coordination environment and dynamical stability of carbon nitride polymorphs. (for full analysis see supplement Section S1 (a)). The phonon for $C_{11}N_4$ with sg-16 and sg-111 for respective structures is shown in Fig. 5.3ab. The sg-111 shows dynamical stability at zero pressure with no imaginary eigen modes in the resultant phonon dispersion curves, while sg-16 phase shows instability across the Brillouin zone.

5.4 Prediction of New Phases

Based on the proposed metric 'M' tested for known carbon-nitride phases in Table 5.1, we explore the extended carbon-nitride phase space as shown in Fig. 5.1bc. The qualitative nature of the metric 'M', based on local structural information and charges employed to screen for structurally stable phases predicts four new C-N phases as shown in Table 5.2. We plot crystal the structure and phonons for new phases in Fig. 5.4 to attempt to establish the accuracy and reliability of our dynamic stability prediction. The results show that in the test structures the proposed metric ac-

curately predicts the dynamic (in)stability of each of the systems. This is very encouraging given new set of compounds have been brought through to this stage by the screening process set by the proposed metric 'M'.

Table 5.2: Metric 'M' predicted structurally stable new carbon-nitride phases, with C4N3 stoichiometry. Phases are arranged in order of increasing 'M'.

System	Space-group	Stability metric	Structural- Stability	
		[M > 0.6]	Predicted	Calculated
C8N6	P21/m (#11)	0.289	No	No
C8N6	Pm (#6 (1))	0.664	Yes	Yes
C16N12	P-3 (#147)	0.843	Yes	Yes
C8N6	Pm (#6 (2))	0.968	Yes	Yes

5.5 Space-Group Analysis of Precited Structure

The β-C_3N_4 phase belongs to the space group P63/m and has two unique N atoms in the asymmetric unit cell. One is located in mirror plane at point $(x, y, 1/4)$ and the other at a roto-inversion point $(1/3, 2/3, 1/4)$. A prototype C_4N_3 structure can be generated by substitution at either of the two Wyckoff positions 6h, or 2c of β-C_3N_4, respectively. Two possible crystal symmetries can emerge by carbon substitution: (a) Pm symmetry: by substitution on a mirror plane; and (b) $P6_3/m$ by substitution at the roto-inversion point with site symmetry $\bar{6}$-. The carbon substitution changes the composition from β-C_3N_4 to C_4N_3. The carbon substitution on a mirror plane gives Pm- C_4N_3 phase, which is a novel structure with C atoms regularly arranged around the mirror plane. The basic unit cell is consisting of 14 C (8)/N (6) atoms conform with the Pm symmetry. Although C-substitution at roto-inversion point $(1/3, 2/3, 1/4)$ of $P6_3/m$ does not reduce symmetry, a carbon atom placed in that position is unstable towards displacement along the c-axis. However, if not displaced, the C coordination would form an unlikely substructure, which wouldn't satisfy the proposed metric 'M'. C in tetrahedron sub-structure in Pm-C_4N_3 becomes positively charged

by losing electrons, whereas the trigonal substructure gains some and becomes negatively charged, see Table 5.3. This charge imbalance created by switching C/N in β-C3N4 stabilizes the new Pm-C_4N_3, which is reflected in the metric M=0.664 in Table 5.2 (supplement Section S1 (b)). The space group P21/m (sg-11) C_4N_3 is obtained by fully relaxing β-C3N4 with switched C/N positions. The negative modes in space group $\#11$ in Fig. 5.4d correspond to carbon displacement at two equivalent roto-inversion points. The negative frequency phonons were followed in deciding C substitution in space group $\#11$ and subsequent full relaxation of all degrees of freedom of new carbon-nitride phase. Our symmetry analysis shows new space-group P-3 ($\#147$) for the C_4N_3. The predicted M=0.843 > 0.6 for Pm suggest structural stability (supplement Section S1 (b)), which is further confirmed by our phonon dispersion in Fig. 5.4c.

Table 5.3: The charge analysis on local substructures, i.e., tetragonal-C and trigonal-N substructures of Pm-C_4N_3. The metric 'M' is defined by sum of charge on tetrahedrally (tet) arranged 'C' divided by sum of charge on trigonally (trig) arranged 'N'. 'M' is 0.664 for Pm-C_4N_3 [5].

Elements	**Wyckoff Position**	**Ideal coordination**	**Charge**	**Metric 'M'**	**Rank**
C	x, 0, z	tetrahedral	1.64	0.722	2
C	x, 1/2, z	tetrahedral	-0.02	0.65	2
C	x, 1/2, z	tetrahedral	0.98	0.738	2
C	x, 0, z	tetrahedral	1.28	0.586	2
C	x, 0, z	tetrahedral	1.01	0.78	2
C	x, 1/2, z	tetrahedral	0.98	0.855	2
C	x, 0, z	tetrahedral	1.98	0.756	2
C	x, 0, z	tetrahedral	4	0	2
N	x, 1/2, z	trigonal	-0.94	0.482	2
N	x, 0, z	trigonal	-1.65	0.736	2
N	x, 0, z	trigonal	-2.36	0.442	2
N	x, 0, z	trigonal	-2.3	0.546	2
N	x, 1/2, z	trigonal	-1.59	0.749	2
N	x, 0, z	trigonal	-3.01	0	2

5.6 Electronic Structure of Pm-C_4N_3 (#6(1))

Having established promising compositions and their candidate structures, we provide quantitative analysis for one of the predicted phases, i.e., Pm-C_4N_3, where C occupies the mirror plane. The optimized Pm-C_4N_3 crystal-structure (see Fig. S1), phonons, density of states, and charge density are shown in Fig. 5.5. The Pm-C_4N_3 has lower formation energy (-1.03 eV) with respect to pure elements. The main features of Pm-C_4N_3 structure in Fig. 5.5a is the presence of single C-C, C-N and N-N bonds, with fourfold (tetrahedral) coordination of C, and threefold coordination of N. The DFW based Green's function (G) and screened Coulomb interaction (W) approximation [87] predicts bandgap of 1.45 eV for Pm-C_4N_3, which lies in the optimal (visible-light absorption) range. We also show in Fig. S2 that the bandgap for Pm-C_4N_3 does not change much under applied hydrostatic pressure. The phonon dispersion and DOS is well proven criteria to establish the structural stability of new materials. The phonon dispersion for Pm-C_4N_3 in Fig. 5.5b is plotted along G-Y-C-Z-G-B-A-E-D high-symmetry direction in the monoclinic Brillouin zone. The DFT calculated dispersion shows no imaginary modes, i.e., structure is dynamically stable. Pm-C_4N_3 has 56 vibrational modes, we only show some low energy modes, for full dispersion see Fig. S3. The phonons within and on boundary correspond to standing waves, where the vibrational modes mainly arise from high symmetry points, e.g., those with k1= k2= k3=0 at -point.

5.7 Free Energy, Vibrational Entropy and Specific Contribution for Pm-C_4N_3

The thermodynamic properties of Pm-C_4N_3 (z=2) are derived from the phonon spectrum calculated using quasi-harmonic approximation (QHA) in Fig. 5.5a. The QHA analysis useful in order to understand vibrational free-energy (F), vibrational entropy (S) and heat capacity at constant volume (Cv) [88; 81]. The Fvib, Svib, and Cv for Pm-C_4N_3 are calculated and shown as a function of temperature in Fig. 5.6a. The QHA calculated Fvib shows monotonous decrease with increasing temperature, i.e., the increased entropy (Svib) contribution with increases with T stabilizes Pm-C_4N_3. The specific heat (Cv) follows the Debye T3 law in the low temperature region ($T < 250$ K), whereas in high temperature region (above 250 K), it is close to a fixed value

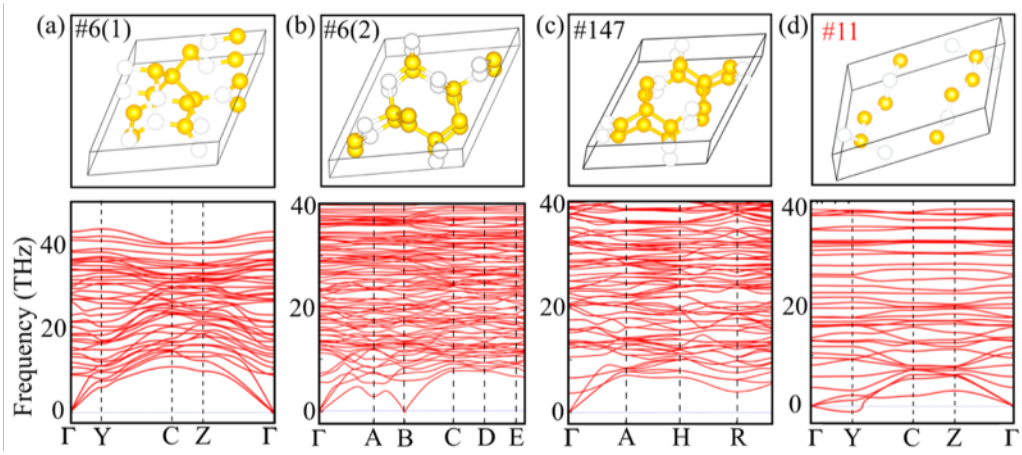

Figure 5.4: Phonon dispersion of (a) Pm (1) or sg-6, (b) Pm (2) or sg-6, (c) P-3 or sg-147, and (d) $P2_1/m$ or sg-11 confirm stability predictions.

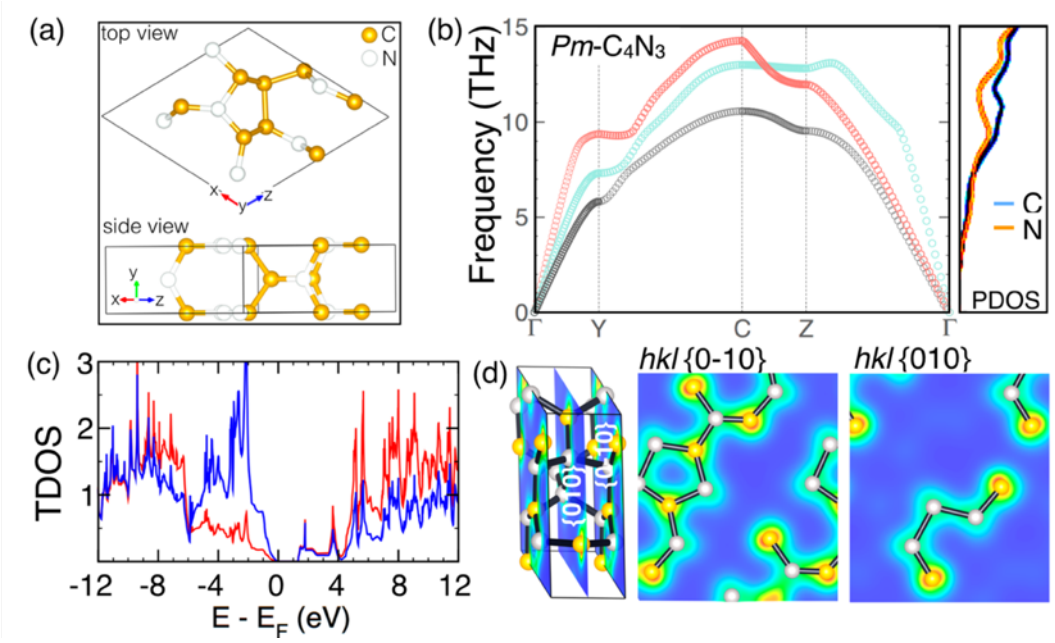

Figure 5.5: (a) Predicted Pm-C_4N_3 monoclinic crystal structure with lattice constant a=6.275 Å, b=2.509 Å, c=6.448 Å, and cell angles =90o, =116.68o, =90o. (b) Pm-C4N3 shows stable phonons at 0 pressure. (see Fig. S2 for full phonon dispersion). (c,d) DFT+HSE calculated partial density of states, and h-k-l-projected charge density.

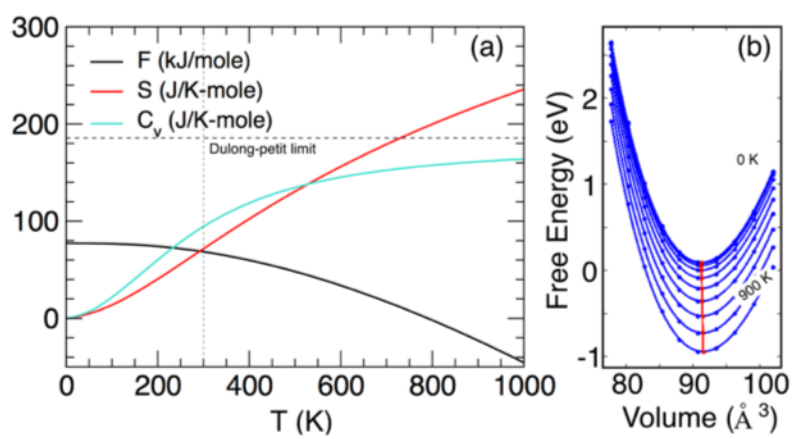

Figure 5.6: (a) Comparison of vibrational Helmholtz free energy (Fvib), vibrational entropy (Svib), and constant-volume specific heat (Cv) for Pm-C_4N_3 calculated using quantum harmonic approximation. (b) Dependence of free energy of Pm-C_4N_3 on volume and temperature.

with approximately 21.4 J/K/mol (25 J/K/mol per atom) in agreement with the Dulong-Petit law [89]. The Helmholtz free energies vs volume plot in Fig. 5.6b also shows increased stability with increasing temperature.

5.8 Negative Thermal Expansion (NTE) and Gruneisen Parameter Pm-C_4N_3

The Pm-C_4N_3 shows negative thermal expansion form 0 K to about 100 K in Fig. 5.4c. This suggests lattice/volume contraction for Pm-C_4N_3 in the temperature range of 0 K-to-120 K in Fig. 5.7a, where bulk-moduli show increase. With the further increase in temperature volume shows linear increase and moduli show decrease. Anharmonic effects are clearly visible on Gruneisen parameter in Fig. 5.7b. Also, the thermal expansion in Fig. 5.7c on average for 0 K-to-120 K is $\alpha V = -0.49x10^{-6}K^{-1}$, whereas positive thermal expansion is found with $\alpha V = -5.34x10^{-6}K^{-1}$. The NTE in Fig. 5.7c closely relates to the anharmonicity of lattice vibrations [90]. The negative modes in Gruneisen parameter serves as a bridge between the behavior of the lattice vibration and the NTE for C_4N_3 [91]. The vibrational modes in Fig. 5.5b and Fig. S2 should be looked more carefully as they reveal the contribution of atoms to thermal expansion, especially to the negative thermal expansion (NTE). The low energy phonon modes can easily be

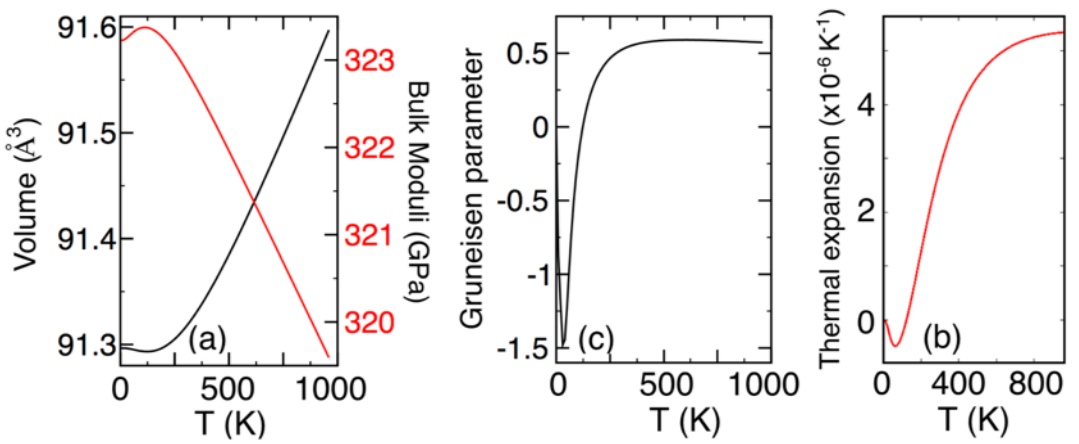

Figure 5.7: (a) Volume/bulk-moduli vs temperature, (b) Gruneisen parameter, and (c) thermal expansion for Pm-C4N3 calculated from quasi-harmonic approximation.

excited, i.e., acoustic branches and the low energy optical modes can be occupied at low temperatures. The optical modes with higher energy will be excited only at high temperatures. Therefore, the optical phonon modes with low energy can possibly contribute most to the NTE.

5.9 Mechanical Stability

The elastic response and mechanical stability of any crystal can be measured from the elastic constants (C_{ij}). Thermal properties including specific heat, thermal expansion, Debye temperature and Gruneisen parameter are exclusively linked to elastic constants (see the supplement), therefore, the discussion of Cij's of new phases is indispensable. We use stress-strain approach as implemented in VASP to calculate elastic properties, which performs six finite distortions to the lattice to derive the elastic constants [92] using both rigid ions as well as allowing relaxation of the ions.

We calculate elastic constants for four new carbon-nitride phases in Table 5.2. Three out of four belong to monoclinic symmetry group, and one has hexagonal symmetry. Born criteria for monoclinic system, is (i) $C_{11} > 0$; (ii) $C_{22} > 0$; (iii) $C_{33} > 0$; (iv) $C_{44} > 0$; (v) $C_{55} > 0$; (vi) $C_{66} > 0$; (vii) $[C_{11} + C_{22} + C_{33} + 2 * (C_{12} + C_{13} + C_{23})] > 0$; (viii) $C_{33} * C_{55} - C_{35}^2 > 0$; (ix) $C_{44} * C_{66} - C_{46}^2 > 0$; (x) $C_{22} + C_{33} - 2 * C_{23} > 0$; (xi) $C_{22} * (C_{33} * C_{55} - C_{35}^2) + 2 * C_{23} *$

$C_{25} * C_{35} - (C_{23}^2) * C_{55} - (C_{25}^2) * C_{33} > 0$; (xii) $2 * [C_{15} * C_{25} * (C_{33} * C_{12} - C_{13} * C_{23} + C_{15} * C_{35} * (C_{22} * C_{13} - C_{12} * C_{23}) + C_{25} * C_{35} * (C_{11} * C_{23} - C_{12} * C_{13})] - [C_{15} * C_{15} * (C_{22} * C_{33} - C_{23}^2) + C_{25} * C_{25} * (C_{11} * C_{33} - C_{13}^2) + C_{35} * C_{35} * (C_{11} * C_{22} - C_{12}^2)] + C_{55} * g > 0$; where, $g = [C_{11} * C_{22} * C_{33} - C_{11} * C_{23} * C_{23} - C_{22} * C_{13} * C_{13} - C_{33} * C_{12} * C_{12} + 2 * C_{12} * C_{13} * C_{23}]$ [38]. Born mechanical stability criteria for hexagonal systems is (i) $C_{11} - C_{12} > 0$; (ii) $2 * C_{13}^2 < C_{33}(C_{11} + C_{12})$; and (iii) $C_{44} > 0$ [93]. $P2_1/m$-C_4N_3 in Table 5.4 fails the mechanical stability criteria. Followed by this, we use C_{ij} to derive elastic moduli (Bulk, Shear, and Young's), melting-temperature, Debye temperature, and Poisson's ratio as shown in Table 5.4. The computed elastic constants in Table 5.4 show mechanical stability for Pm (1), Pm (2), and P-3 at ambient pressure. Remarkably, the three-dimensional framework of short covalent bonds in Fig. 5.5a seems to be the factor responsible for the extreme mechanical behavior of the Pm (1), Pm (2), and P-3 phases.

5.10 Optical Property of Pm-C_3N_4

The DFT+GW [87] approach predicts optimal bandgap of 1.45 eV for Pm-C_4N_3, which lies in the visible (light) range. Beyond the basic electronic-structure, bandgap, and phonons as shown in Fig. 5.5, the optical absorption is another important aspect of semiconducting materials. The GW based Bethe-Salpeter equation (BSE) [94] with a statistically screened electron-hole interaction has been successfully used to calculate optical excitation energies in the past [95; 96; 97; 98]. Fig. 5.8 compares imaginary dielectric function or optical absorption of Pm-C_4N_3 calculated from GW+BSE and GW+RPA. We found common two-peak structure both in GW+RPA and GW+BSE at around (2.5 eV; 5.8 eV) and (3.9 eV; 8.1 eV), respectively.

5.11 Conclusion

We present a facile 'metric' for the identification of structurally (phonons) stable inorganic compounds. Metric uses charge-imbalance within the local substructures of crystalline compounds. The metric predicts four new stoichiometric carbon-nitride (C_4N_3) phases with space-group Pm (1), Pm (2), P-3 and $P2_1$/m, however, only three out of four (Pm (1), Pm (2), P-3) criteria for structural stability. Our direct phonon calculations further predict their structural stabil-

Table 5.4: Lattice parameters, formation enthalpy, bandgap, and elastic properties of new Pm (1), $P2_1/m$, Pm (2), and P-3 phases calculated from first-principles density-functional theory.

System C_4N_3	a	b	c	α	β	γ	E_{form} (eV)	E_{gap}(eV)		
	(Å)			(°)				PBE	GW	HSE
Pm (1)	6.275	2.509	6.448	90	116.7	90	-1.03	0.3	1.45	1.32
$P2_1/m$	8.618	5.996	2.347	90	90	115.2	-0.88	0	–	0
Pm (2)	6.539	4.809	6.552	90	119.5	90	-1.13	4.22	–	5.88
P-3	6.628	6.628	4.723	90	90	120	-1.13	4.13	–	5.77

C_{ij}(GPa)	C_{11}	C_{22}	C_{33}	C_{44}	C_{55}	C_{66}	C_{12}	C_{13}	C_{23}
Pm (1)	910	827	907.5	153.5	246.3	236.4	52.9	77.4	29.8
$P2_1/m$	92	170	916	153	-92	54	78	15	-2
Pm (2)	617	1013	711	310	230	289	157	224	125
P-3	657	657	1114	344	344	228	201	137	137

	K	G	E	P-wave	n	k=K/G	T_D(K)	T_m(K)
	(GPa)							
Pm (1)	329	293	678	720	0.157	1.125	1598	3652
$P2_1/m$	151	95	237	279	0.239	1.583	908	1639
Pm (2)	372	288	688	757	0.192	1.292	1625	4039
P-3	375	313	736	793	0.173	1.198	1684	4036

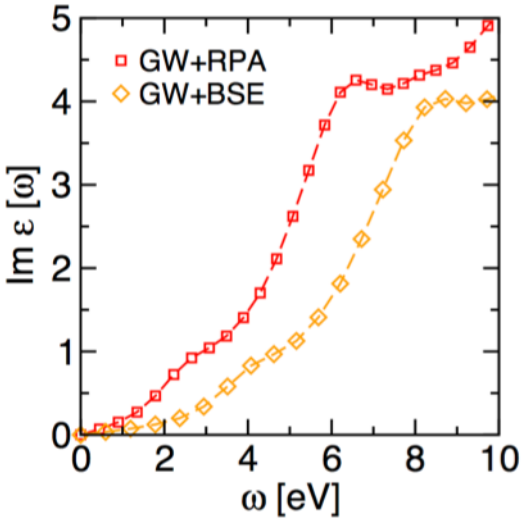

Figure 5.8: The comparison of the imaginary dielectric function (optical absorption) of Pm-C_4N_3 calculated using GW+RPA and GW+BSE approach as implemented within VASP [3; 4].

ity. We also tested all four cases for their mechanical stability, we show that the same three phases (Pm (1), Pm (2), P-3) qualify Born criteria. The hybrid-functional HSE06 (GW) predicted bandgap of 1.35 eV (1.45 eV) for Pm-C_4N_3 lies in the optimal range for various practical applications in semiconductor industry. This makes the newly predicted carbon-nitride phase very exciting finding by our proposed metric. We believe that our simple, yet powerful approach will accelerate the search of unknown and unexplored phases of inorganic compounds as the proposed metric can potentially be modified to consider other chemical systems in which coordination and charge balance are expected to play a role in determining the dynamic stability of the crystalline arrangements.

5.12 Acknowledgement

We acknowledge support from National Science Foundation through grants no. (DMREF) CMMI-1729350. First-principles calculations were carried out at the Supercomputing Facility at Texas A&M University.

6. SUMMARY AND CONCLUSIONS

Much of the future depends on martensitic transformations. There is very little exageration in that statement as the vast array of applications these atomistic machines are capable of is only limited by the imagination. Low power computational devices with information storage that can hold continuous range of values would bring analog computating back into a technological paradigm shift. From memristic devices, low power circuitry, optical filters to heat sensitive functional materials and biocompatible medical devices. One thing is clear, the future of materials research will involve an increasing dependence on collaboration between multiple fields of science.

6.1 Further Study

For my future work, I plan to compare my results on VO2 with other oxide systems in order to gain insight on the interactions between various dopants and transition metals. Furthermore, previous calculations (found in calculation section) on Tungsten doped VO2 show support for the conclusion that a reduction of oxygen vacancies tends to increase the hysteresis width [58]. In light of Boron's effect on kinetics of the transformation, I would be interested in resolving the magnitude of effect Tungsten doping has on the energy barriers of Boron mobility. Also, I plan on expanding the compositional search space for the B2 to B19' energy landscape database and synergize the sampling scheme into the materials discovery framework being developed for use in the AFOSR project. The development of metric of similarity and stability across systems can be further explored as a tool to identify promising regions in compositions space and quantiy their proximity.

REFERENCES

[1] S. H. Zhou and R. E. Napolitano, "Identification of the B33 martensite phase in Cu–Zr using first-principles and X-ray diffraction," *Scripta Materialia*, vol. 59, pp. 1143–1146, Nov. 2008.

[2] A. Jain, "The Materials Project: A materials genome approach to accelerating materials innovation," *APL Materials*, vol. 1, no. 1, p. 011002, 2013.

[3] G. Kresse and D. Joubert, "From Ultrasoft Pseudopotentials to the Projector Augmented-Wave Method," *Phys. Rev. B*, vol. 59, pp. 1758–1775, 1999.

[4] J. Perdew, K. Burke, and M. Ernzerhof, "Generalized Gradient Approximation Made Simple," *Phys. Rev. Lett*, vol. 77, pp. 3865–3868, 1996.

[5] N. Zimmermann and A. Jain, "Local structure order parameters and site fingerprints for quantification of coordination environment and crystal structure similarity," *RSC Adv*, vol. 10, pp. 6063–6081, 2020.

[6] Z. Zhang, R. D. James, and S. Müller, "Energy barriers and hysteresis in martensitic phase transformations," *Acta Materialia*, vol. 57, pp. 4332–4352, Sept. 2009.

[7] A. N. Bucsek, G. A. Hudish, G. S. Bigelow, R. D. Noebe, and A. P. Stebner, "Composition, Compatibility, and the Functional Performances of Ternary NiTiX High-Temperature Shape Memory Alloys," *Shape Memory and Superelasticity*, vol. 2, pp. 62–79, Mar. 2016.

[8] Z.-B. Li, B. Yang, Y.-D. Zhang, C. Esling, X. Zhao, and L. Zuo, "Crystallographic insights into diamond-shaped 7M martensite in Ni–Mn–Ga ferromagnetic shape-memory alloys," *IUCrJ*, vol. 6, pp. 909–920, Aug. 2019.

[9] S.-H. Guan, X.-J. Zhang, and Z.-P. Liu, "Energy Landscape of Zirconia Phase Transitions," *Journal of the American Chemical Society*, vol. 137, pp. 8010–8013, July 2015.

[10] X. Luo, W. Zhou, S. V. Ushakov, A. Navrotsky, and A. A. Demkov, "Monoclinic to tetragonal transformations in hafnia and zirconia: A combined calorimetric and density functional study," *Physical Review B*, vol. 80, Oct. 2009.

[11] S. Kustov, D. Salas, E. Cesari, R. Santamarta, and J. Van Humbeeck, "Isothermal and athermal martensitic transformations in Ni–Ti shape memory alloys," *Acta Materialia*, vol. 60, pp. 2578–2592, Apr. 2012.

[12] S. Chen, J. Liu, L. Wang, H. Luo, and Y. Gao, "Unraveling Mechanism on Reducing Thermal Hysteresis Width of VO_2 by Ti Doping: A Joint Experimental and Theoretical Study," *The Journal of Physical Chemistry C*, vol. 118, pp. 18938–18944, Aug. 2014.

[13] K. Miyazaki, K. Shibuya, M. Suzuki, K. Sakai, J.-i. Fujita, and A. Sawa, "Chromium–niobium co-doped vanadium dioxide films: Large temperature coefficient of resistance and practically no thermal hysteresis of the metal–insulator transition," *AIP Advances*, vol. 6, p. 055012, May 2016.

[14] J. Lee, Y. Ikeda, and I. Tanaka, "First-principles screening of structural properties of intermetallic compounds on martensitic transformation," *npj Computational Materials*, vol. 3, p. 52, Nov. 2017.

[15] K. J. Caspersen and E. A. Carter, "Finding transition states for crystalline solid–solid phase transformations," *Proceedings of the National Academy of Sciences of the United States of America*, vol. 102, no. 19, pp. 6738–6743, 2005.

[16] P. Hohenberg and W. Kohn, "Inhomogeneous electron gas," *Physical review*, vol. 136, no. 3B, p. B864, 1964.

[17] J. P. Perdew, K. Burke, and M. Ernzerhof, "Generalized Gradient Approximation Made Simple," *Physical Review Letters*, vol. 77, pp. 3865–3868, Oct. 1996.

[18] M. Cococcioni and S. de Gironcoli, "Linear response approach to the calculation of the effective interaction parameters in the LDA + U method," *Physical Review B*, vol. 71, Jan. 2005.

[19] S. Lutfalla, V. Shapovalov, and A. T. Bell, "Calibration of the DFT/GGA+U Method for Determination of Reduction Energies for Transition and Rare Earth Metal Oxides of Ti, V, Mo, and Ce," *Journal of Chemical Theory and Computation*, vol. 7, pp. 2218–2223, July 2011.

[20] M. E. Arroyo-de Dompablo, A. Morales-García, and M. Taravillo, "DFT+U calculations of crystal lattice, electronic structure, and phase stability under pressure of TiO2 polymorphs," *The Journal of Chemical Physics*, vol. 135, p. 054503, Aug. 2011.

[21] G. Hautier, S. P. Ong, A. Jain, C. J. Moore, and G. Ceder, "Accuracy of density functional theory in predicting formation energies of ternary oxides from binary oxides and its implication on phase stability," *Physical Review B*, vol. 85, Apr. 2012.

[22] S. Kirklin, J. E. Saal, B. Meredig, A. Thompson, J. W. Doak, M. Aykol, S. Rühl, and C. Wolverton, "The Open Quantum Materials Database (OQMD): Assessing the accuracy of DFT formation energies," *NPJ Computational Materials*, vol. 1, p. 15010, Dec. 2015.

[23] W. E, W. Ren, and E. Vanden-Eijnden, "String method for the study of rare events," *Physical Review B*, vol. 66, Aug. 2002.

[24] K. K. Song, D. Y. Wu, S. Pauly, C. X. Peng, L. Wang, and J. Eckert, "Thermal stability of B2 CuZr phase, microstructural evolution and martensitic transformation in Cu–Zr–Ti alloys," *Intermetallics*, vol. 67, pp. 177–184, Dec. 2015.

[25] H. Bala and S. Szymura, "Acid corrosion of amorphous and crystalline Cu-Zr alloys," *Applied Surface Science*, vol. 35, pp. 41–51, Oct. 1988.

[26] F. E. Wang, W. J. Buehler, and S. J. Pickart, "Crystal Structure and a Unique "Martensitic" Transition of TiNi," *Journal of Applied Physics*, vol. 36, pp. 3232–3239, Oct. 1965.

[27] J. W. Seo and D. Schryvers, "TEM investigation of the microstructure and defects of CuZr martensite. Part I: Morphology and twin systems," *Acta Materialia*, vol. 46, pp. 1165–1175, Feb. 1998.

[28] M. Aroyo, J. Perez-Mato, D. Orobengoa, E. Tasci, G. De La Flor, and A. Kirov, "Crystallography online: Bilbao crystallographic server," *Bulgarian Chemical Communications*, vol. 43, no. 2, pp. 183–197, 2011.

[29] A. Togo and I. Tanaka, "Evolution of crystal structures in metallic elements," *Physical Review B*, vol. 87, p. 184104, May 2013.

[30] C. Capillas, E. S. Tasci, G. de la Flor, D. Orobengoa, J. M. Perez-Mato, and M. I. Aroyo,

"A new computer tool at the Bilbao Crystallographic Server to detect and characterize pseudosymmetry," *Zeitschrift für Kristallographie*, vol. 226, pp. 186–196, Feb. 2011.

[31] A. Evirgen, I. Karaman, R. Santamarta, J. Pons, C. Hayrettin, and R. D. Noebe, "Relationship between crystallographic compatibility and thermal hysteresis in Ni-rich NiTiHf and NiTiZr high temperature shape memory alloys," *Acta Materialia*, vol. 121, pp. 374–383, Dec. 2016.

[32] Y. Miao, R. Villarreal, A. Talapatra, R. Arróyave, and J. J. Vlassak, "Nanocalorimetry and ab initio study of ternary elements in CuZr-based shape memory alloy," *Acta Materialia*, vol. 182, pp. 29–38, Jan. 2020.

[33] G. Kresse and J. Furthmüller, "Efficient iterative schemes for ab initio total-energy calculations using a plane-wave basis set," *Physical review B*, vol. 54, no. 16, p. 11169, 1996.

[34] H. Monkhorst and J. Pack, "Special points for Brillouin-zone integrations," *Phys. Rev. B*, vol. 13, pp. 5188–5192, 1976.

[35] K. Bhattacharya and P. o. M. a. M. S. K. Bhattacharya, *Microstructure of Martensite: Why It Forms and How It Gives Rise to the Shape-Memory Effect*. OUP Oxford, Nov. 2003.

[36] C. Cayron, "The transformation matrices (distortion, orientation, correspondence), their continuous forms and their variants," *Acta Crystallographica Section A Foundations and Advances*, vol. 75, pp. 411–437, May 2019.

[37] R. D. James and K. F. Hane, "Martensitic transformations and shape-memory materials," *Acta Materialia*, vol. 48, pp. 197–222, Jan. 2000.

[38] M. E. Gruner, R. Niemann, P. Entel, R. Pentcheva, U. K. Rößler, K. Nielsch, and S. Fähler, "Modulations in martensitic Heusler alloys originate from nanotwin ordering," *Scientific Reports*, vol. 8, pp. 1–12, May 2018.

[39] R. Delville, D. Schryvers, Z. Zhang, and R. D. James, "Transmission electron microscopy investigation of microstructures in low-hysteresis alloys with special lattice parameters," *Scripta Materialia*, vol. 60, pp. 293–296, Mar. 2009.

[40] M. Huisman-Kleinherenbrink, Y. Jian, and J. Beyer, "Influence of manganese on the trans-

formation temperatures of NiSOT& shape memory alloys," *MATERIALS LETTERS*, vol. 1, no. 3, p. 6, 1991.

[41] I. Boybat, M. Le Gallo, S. R. Nandakumar, T. Moraitis, T. Parnell, T. Tuma, B. Rajendran, Y. Leblebici, A. Sebastian, and E. Eleftheriou, "Neuromorphic computing with multi-memristive synapses," *Nature Communications*, vol. 9, p. 2514, Dec. 2018.

[42] Z. Wang, S. Joshi, S. E. Savel'ev, H. Jiang, R. Midya, P. Lin, M. Hu, N. Ge, J. P. Strachan, Z. Li, Q. Wu, M. Barnell, G.-L. Li, H. L. Xin, R. S. Williams, Q. Xia, and J. J. Yang, "Memristors with diffusive dynamics as synaptic emulators for neuromorphic computing," *Nature Materials*, vol. 16, pp. 101–108, Jan. 2017.

[43] D. G. Sellers, "Dynamically Evolving Metastability in an Atomic Hourglass: Temporal Control of the Metal-Insulator Transition of \ce{VO_2) upon Introduction of a Mobile Dopant," *Manuscript submitted for publication*.

[44] D. B. McWhan, M. Marezio, J. P. Remeika, and P. D. Dernier, "X-ray diffraction study of metallic V${\mathrm{O}}_{2}$," *Physical Review B*, vol. 10, pp. 490–495, July 1974.

[45] G. Andersson, "Studies on Vanadium Oxides," *Acta Chemica Scandinavica*, vol. 10, p. 623, 1956.

[46] W. Fan, J. Cao, J. Seidel, Y. Gu, J. W. Yim, C. Barrett, K. M. Yu, J. Ji, R. Ramesh, L. Q. Chen, and J. Wu, "Large kinetic asymmetry in the metal-insulator transition nucleated at localized and extended defects," *Physical Review B*, vol. 83, June 2011.

[47] Y. G. Liang, S. Lee, H. S. Yu, X. H. Zhang*, H. R. Zhang, L. A. Bendersky, Y. J. Liang, P. Y. Zavalij, X. Chen, R. D. James, and I. Takeuchi*, "Tuning the Hysteresis of a Metal-Insulator Transition via Lattice Compatibility," *arXiv:1905.01398 [cond-mat]*, May 2019.

[48] S. Chen, J. Liu, H. Luo, and Y. Gao, "Calculation Evidence of Staged Mott and Peierls Transitions in VO $_2$ Revealed by Mapping Reduced-Dimension Potential Energy Surface," *The Journal of Physical Chemistry Letters*, vol. 6, pp. 3650–3656, Sept. 2015.

[49] Z. Tao, T.-R. T. Han, S. D. Mahanti, P. M. Duxbury, F. Yuan, C.-Y. Ruan, K. Wang, and J. Wu, "Decoupling of Structural and Electronic Phase Transitions in VO 2," *Physical Re-*

view Letters, vol. 109, Oct. 2012.

[50] D. Wegkamp and J. Stähler, "Ultrafast dynamics during the photoinduced phase transition in VO2," *Progress in Surface Science*, vol. 90, pp. 464–502, Dec. 2015.

[51] T. E. G. Alivio, D. G. Sellers, H. Asayesh-Ardakani, E. J. Braham, G. A. Horrocks, K. E. Pelcher, R. Villareal, L. Zuin, P. J. Shamberger, R. Arróyave, R. Shahbazian-Yassar, and S. Banerjee, "Postsynthetic Route for Modifying the Metal—Insulator Transition of VO2 by Interstitial Dopant Incorporation," *Chemistry of Materials*, vol. 29, pp. 5401–5412, June 2017.

[52] A. D. Mighell, "Lattice Symmetry and Identification—The Fundamental Role of Reduced Cells in Materials Characterization," *Journal of Research of the National Institute of Standards and Technology*, vol. 106, no. 6, pp. 983–995, 2001.

[53] S. L. Dudarev, G. A. Botton, S. Y. Savrasov, C. J. Humphreys, and A. P. Sutton, "Electron-energy-loss spectra and the structural stability of nickel oxide: An LSDA+U study," *Physical Review B*, vol. 57, pp. 1505–1509, Jan. 1998.

[54] D. Sheppard, P. Xiao, W. Chemelewski, D. D. Johnson, and G. Henkelman, "A generalized solid-state nudged elastic band method," *The Journal of Chemical Physics*, vol. 136, p. 074103, Feb. 2012.

[55] S. Curtarolo, W. Setyawan, G. L. W. Hart, M. Jahnatek, R. V. Chepulskii, R. H. Taylor, S. Wang, J. Xue, K. Yang, O. Levy, M. J. Mehl, H. T. Stokes, D. O. Demchenko, and D. Morgan, "AFLOW: An automatic framework for high-throughput materials discovery," *Computational Materials Science*, vol. 58, pp. 218–226, June 2012.

[56] R. A. Evarestov, Y. E. Kitaev, and V. V. Porsev, "Use of Wyckoff position splittings in the supercell model of crystals with point defects," *Journal of Applied Crystallography*, vol. 50, pp. 893–900, June 2017.

[57] H. T. Stokes and D. M. Hatch, "ISOTROPY SUBGROUPS OF THE 230 CRYSTALLOGRAPHIC SPACE GROUPS," in *Isotropy Subgroups of the 230 Crystallographic Space Groups*, pp. 1–624, Singapore: World Scientific, 1988.

[58] E. J. Braham, D. Sellers, E. Emmons, R. Villarreal, H. Asayesh-Ardakani, N. A. Fleer, K. E. Farley, R. Shahbazian-Yassar, R. Arròyave, P. J. Shamberger, and S. Banerjee, "Modulating the Hysteresis of an Electronic Transition: Launching Alternative Transformation Pathways in the Metal–Insulator Transition of Vanadium(IV) Oxide," *Chemistry of Materials*, vol. 30, pp. 214–224, Jan. 2018.

[59] X. Tan, T. Yao, R. Long, Z. Sun, Y. Feng, H. Cheng, X. Yuan, W. Zhang, Q. Liu, C. Wu, Y. Xie, and S. Wei, "Unraveling Metal-insulator Transition Mechanism of VO2 Triggered by Tungsten Doping," *Scientific Reports*, vol. 2, June 2012.

[60] Z. Rong, R. Malik, P. Canepa, G. Sai Gautam, M. Liu, A. Jain, K. Persson, and G. Ceder, "Materials Design Rules for Multivalent Ion Mobility in Intercalation Structures," *Chemistry of Materials*, vol. 27, pp. 6016–6021, Sept. 2015.

[61] K. Li and D., "Hardness of group IVA and IVB nitrides," *Physica Scripta*, vol. T139, no. 1, p. 014073, 2010.

[62] P. McMillan, "High pressure synthesis of solids," *Current Opinion in Solid State and Materials Science*, vol. 4, no. 2, pp. 171–178, 1999.

[63] V. Khabashesku, J. Zimmerman, and J. Margrave, "Powder Synthesis and Characterization of Amorphous Carbon Nitride," *Chem. Mater*, vol. 12, no. 11, pp. 3264–3270, 2000.

[64] A. Liu and M. Cohen, "Prediction of new low compressibility solids," *Science*, vol. 245, pp. 841–2, 1989.

[65] C. Liu and M. Cohen, "Structural properties and electronic structure of low-compressibility materials: β-Si3N4 and hypothetical β-C3N4," *Phys. Rev. B*, vol. 41, no. 15, pp. 10727–10734, 1990.

[66] K. Schwinghammer, M. Mesch, V. Duppel, C. Ziegler, J. Senker, and B. Lotsch, "Crystalline Carbon Nitride Nanosheets for Improved Visible-Light Hydrogen Evolution," *J. Am. Chem. Soc*, vol. 136, pp. 1730–1733, 2014.

[67] X. Wang, K. Maeda, A. Thomas, K. Takanabe, G. Xin, J. Carlsson, K. Domen, and M. Antonietti, "A metal-free polymeric photocatalyst for hydrogen production from water under

visible light," *Nat. Mater*, vol. 8, pp. 76–80, 2009.

[68] F. Su, S. Mathew, G. Lipner, X. Fu, M. Antonietti, S. Blechert, and X. Wang, "Mpg-C3N4-Catalyzed Selective Oxidation of Alcohols Using O2 and Visible Light," *J. Am. Chem. Soc*, vol. 132, pp. 16299–16301, 2010.

[69] N. Mansor, A. Jorge, F. Cora, C. Gibbs, R. Jervis, P. McMillan, X. Wang, and D. Brett, "Graphitic Carbon Nitride Supported Catalysts for Polymer Electrolyte Fuel Cells," *J. Phys. Chem. C*, vol. 118, pp. 6831–6838, 2014.

[70] A. Schwarzer, T. Saplinova, and E. Kroke, "Tri-s-triazines (s-heptazines)—From a "mystery molecule" to industrially relevant carbon nitride materials," *Coord. Chem. Rev*, vol. 257, pp. 2032–2062, 2013.

[71] F. Goettmann, A. Fischer, M. Antonietti, and A. Thomas, "Chemical synthesis of mesoporous carbon nitrides using hard templates and their use as a metal-free catalyst for Friedel-Crafts reaction of benzene," *Angew. Chem., Int. Ed*, vol. 45, pp. 4467–4471, 2006.

[72] G. al Veith, "Electrochemical and Solid-State Lithiation of Graphitic C3N4," *Chem. Mater*, vol. 25, pp. 503–508, 2013.

[73] F. al Withers, "Light-emitting diodes by band-structure engineering in van der Waals heterostructures," *Nat. Mater*, vol. 14, pp. 301–306, 2015.

[74] X. Zhang, X. Xie, H. Wang, J. Zhang, B. Pan, and Y. Xie, "Enhanced Photoresponsive Ultrathin Graphitic-Phase C3N4 Nanosheets for Bioimaging," *J. Am. Chem. Soc*, vol. 135, pp. 18–21, 2013.

[75] V. Solozhenko, "Equation of state and phase stability of turbostratic carbon nitride," *J. Phys. Chem. Solids*, vol. 64, pp. 1265–1270, 2003.

[76] H. Dong, A. Oganov, and Q. al Zhu, "The phase diagram and hardness of carbon nitrides," *Sci Rep*, vol. 5, p. 9870, 2015.

[77] G. Kresse and J. Hafner, "Ab Initio Molecular Dynamics for Liquid Metals," *Phys. Rev. B*, vol. 47, pp. 558–561, 1993.

[78] X. Gonze and C. Lee, "Dynamical matrices, Born effective charges, dielectric permittivity

tensors, and interatomic force constants from density-functional perturbation theory," *Phys. Rev. B*, vol. 55, p. 10355, 1997.

[79] L. Chaput, A. Togo, I. Tanaka, and G. Hug, "Phonon-phonon interactions in transition metals," *Phys. Rev. B*, vol. 84, p. 094302, 2011.

[80] K. Parlinski, Z. Li, and Y. Kawazoe, "First-Principles Determination of the Soft Mode in Cubic ZrO2," *Phys. Rev. Lett*, vol. 78, p. 4063, 1997.

[81] A. Togo, L. Chaput, I. Tanaka, and G. Hug, "First-principles phonon calculations of thermal expansion in Ti3SiC2, Ti3AlC2, and Ti3GeC2," *Phys. Rev. B*, vol. 81, p. 174301, 2010.

[82] X. Sheng, Q. Yan, F. Ye, Q. Zheng, and G. Su, "T-carbon: A novel carbon allotrope. T-Carbon: A Novel Carbon Allotrope," *Phys. Rev. Lett*, vol. 106, p. 155703, 2011.

[83] S. Mo, L. Ouyang, W. Ching, I. Tanaka, Y. Koyama, and R. Riedel, "Interesting physical properties of the new spinel phase of Si3N4 and C3N4," *Phys. Rev. Lett*, vol. 83, pp. 5046–5049, 1999.

[84] J. He, L. Guo, X. Guo, R. Liu, Y. Tian, H. Wang, and C. Gao, "Predicting hardness of dense C3N4 polymorphs," *Appl. Phys. Lett*, vol. 88, p. 101906, 2006.

[85] P. Singh, M. Harbola, and D. Johnson, "Better band gaps for wide-gap semiconductors from a locally corrected exchange-correlation potential that nearly eliminates self-interaction errors," *J. Phys.: Condens. Matter*, vol. 29, p. 424001, 2017.

[86] S. Datta, *Exploring the Role of Electronic Structure on Photo-Catalytic Behavior of Carbon-Nitride Polymorphs*. 2019.

[87] F. Aryasetiawan and O. Gunnarsson, "The GW method," *Rep. Prog. Phys*, vol. 61, p. 237, 1998.

[88] A. Togo and I. Tanaka, "First principles phonon calculations in materials science," *Scr. Mater*, vol. 108, 1, 2015.

[89] A.-T. Petit and P.-L. Dulong, "Recherches sur quelques points importants de la Théorie de la Chaleur"," in *Annales de Chimie et de Physique (in French*, vol. 10, pp. 395–413, 1819.

[90] L. Wang, P.-F. Yuan, F. Wang, Q. Sun, E.-J. Liang, and Y. Jia, "Metal fluorides, a new family

of negative thermal expansion materials," *Mater. Res. Bull*, vol. 47, p. 1113, 2012.

[91] Z. Wang, F. Wang, L. Wang, Y. Jia, and Q. Sun, "First-principles study of negative thermal expansion in zinc oxide," *J. Appl. Phys*, vol. 114, p. 063508, 2013.

[92] Y.-L. Page and P. Saxe, "Symmetry-general least-squares extraction of elastic data for strained materials from ab initio calculations of stress," *Phys. Rev. B*, vol. 65, p. 104104, 2002.

[93] F. Mouhat and F.-X. Coudert, "Necessary and sufficient elastic stability conditions in various crystal systems," *Phys. Rev. B*, vol. 90, p. 224104, 2014.

[94] E. Salpeter and H. Bethe, "A Relativistic Equation for Bound-State Problems," *Phys. Rev*, vol. 84, p. 1232, 1951.

[95] S. Albrecht, L. Reining, R. Del Sole, and G. Onida, "Ab Initio Calculation of Excitonic Effects in the Optical Spectra of Semiconductors," *Phys. Rev. Lett*, vol. 80, p. 4510, 1998.

[96] M. Rohlfing and S. Louie, "Excitons and Optical Spectrum of the Si(111)-(2×1) Surface," *Phys. Rev. Lett*, vol. 83, p. 856, 1999.

[97] L. Yang, J. Deslippe, C.-H. Park, M. Cohen, and S. Louie, "Excitonic Effects on the Optical Response of Graphene and Bilayer Graphene," *Phys. Rev. Lett*, vol. 103, p. 186802, 2009.

[98] B. Arnaud, S. Lebegue, P. Rabiller, and M. Alouani, "Huge Excitonic Effects in Layered Hexagonal Boron Nitride," *Phys. Rev. Lett*, vol. 96, p. 026402, 2006.

[99] J. Wan, Q. Ren, N. Wu, and Y. Gao, "Density functional theory study of M-doped (M = B, C, N, Mg, Al) VO2 nanoparticles for thermochromic energy-saving foils," *Journal of Alloys and Compounds*, vol. 662, pp. 621–627, Mar. 2016.

[100] S.-H. Bae, S. Lee, H. Koo, L. Lin, B. H. Jo, C. Park, and Z. L. Wang, "The Memristive Properties of a Single VO $_2$ Nanowire with Switching Controlled by Self-Heating," *Advanced Materials*, vol. 25, pp. 5098–5103, Sept. 2013.

[101] O. Nájera, M. Civelli, V. Dobrosavljević, and M. J. Rozenberg, "Resolving the ${\mathrm{VO}}_{2}$ controversy: Mott mechanism dominates the insulator-to-metal transition," *Physical Review B*, vol. 95, p. 035113, Jan. 2017.

[102] R. Sakuma, T. Miyake, and F. Aryasetiawan, "First-Principles Study of Correlation Effects in VO2: Peierls vs. Mott-Hubbard," *arXiv:0804.0990 [cond-mat]*, Apr. 2008.

[103] P. J. Fillingham, "Domain Structure and Twinning in Crystals of Vanadium Dioxide," *Journal of Applied Physics*, vol. 38, no. 12, p. 4823, 1967.

APPENDIX A

FIRST APPENDIX

Text for the Appendix follows.

A.1 Structure of VO2

Transition metal oxides (TMOs) are a class of materials showcasing diverse variability in electronic properties that modulate across the transition. The electronic-structure property relations can be attributed to their valence orbital behaviour. For example, in VO2, the metallic element consists of partially filled d orbitals but due to coulombic interaction between the d-shell electrons, the stable phase can become insulating even though traditional band theory would predict metallic behaviour. Vanadium dioxide undergoes a reversible metal-insulator transition (MIT) close to 340 K. The transformation is structurally evidenced by vanadium atoms dimerizing as the tetragonal symmetry shifts to a reduced symmetry monoclinic phase. Furthermore, there is a strong change in its optical response and electronic properties which makes it an ideal candidate material in many applications ranging from smart window [99], optical filters, phase change memory [100], and field effect transistors . It is characterized as being a proper martensitic reaction but the underlying mechanisms driving the transition are still debated in the literature [101; 102]. Many attempts have been made to model the atomistic mechanisms of solid-solid transformations to a series of strain and orientation steps but current experimental efforts are limited in their ability to capture the fast atomic dynamics that characterize martensitic transformations. A combination of computation, in conjunction with x-ray methods and calorimetry still remains the practical method of choice in exploring the kinetic mechanisms of a transformation.

The lattice correspondence between tetragonal (solid line) and monoclinic unit cells is shown graphically in figure A.1. The monoclinic unit cell contains four formula units of VO2(Z = 4) and belongs to space group P21/c. Whereas the more symmetric tetragonal cell contains two formula units and belongs to space group P42/mnm. To study the transformation path, a lattice cell

compatible with both structures is deduced through an orientation correspondence. An extended rutile (R) cell will be needed at twice the length along its c-axis. [103]

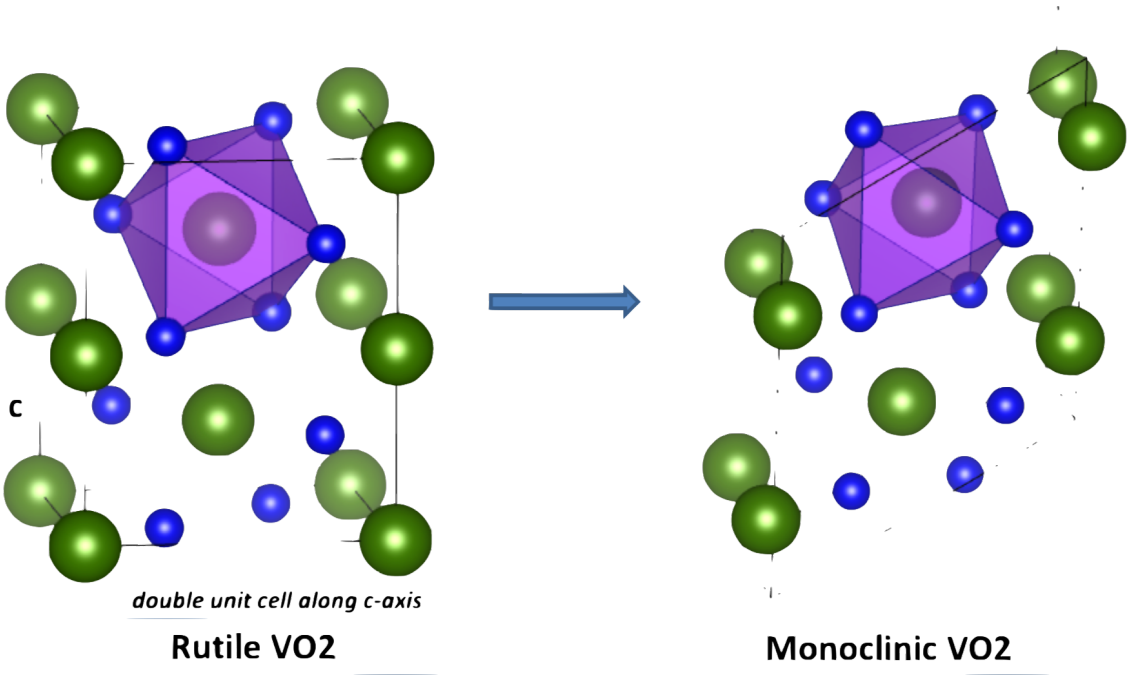

Figure A.1: Lattice Correspondence